DOKUZ EYLÜL UNIVERSITY
GRADUATE SCHOOL OF NATURAL AND APPLIED SCIENCES

INVESTIGATION OF SOURCE, SITE, REGIONAL AND NEAR SURFACE ATTENUATION CHARACTERISTICS IN THE WESTERN ANATOLIA REGION

by
Tevfik Özgür KURTULMUŞ

May, 2014
İZMİR

INVESTIGATION OF SOURCE, SITE, REGIONAL AND NEAR SURFACE ATTENUATION CHARACTERISTICS IN THE WESTERN ANATOLIA REGION

A Thesis Submitted to the
Graduate School of Natural and Applied Sciences of Dokuz Eylül University
In Partial Fulfillment of the Requirements for the Degree of Doctor of
Philosophy in Geophysical Engineering

by
Tevfik Özgür KURTULMUŞ

May, 2014
İZMİR

Ph.D. THESIS EXAMINATION RESULT FORM

We have read the thesis entitled **"INVESTIGATION OF SOURCE, SITE, REGIONAL AND NEAR SURFACE ATTENUATION CHARACTERISTICS IN THE WESTERN ANATOLIA REGION"** completed by **TEVFİK ÖZGÜR KURTULMUŞ** under supervision of **ASSOC. PROF. DR. NİHAL AKYOL** and we certify that in our opinion it is fully adequate, in scope and in quality, as a thesis for the degree of Doctor of Philosophy.

Assoc. Prof. Dr. Nihal AKYOL

Supervisor

Prof. Dr. Talip GÜNGÖR

Thesis Committee Member

Asst. Prof. Dr. Mehmet UTKU

Thesis Committee Member

Assoc. Prof. Dr. Eşref YALÇINKAYA

Examining Committee Member

Assoc. Prof. Dr. Gökhan GÖKTÜRKLER

Examining Committee Member

Prof. Dr. Ayşe OKUR
Director
Graduate School of Natural and Applied Sciences

ACKNOWLEDGMENTS

Firstly, I would like to thank my thesis supervisor, Assoc. Prof. Dr. Nihal AKYOL, for her continuous encouragement, support, and advice throughout all process of preparation of the thesis. She has guided me with her vast knowledge, and her patience has enabled me to have success during my Ph.D.'s program. I am grateful to her directing me to study on this issue, and showing great enthusiasm and dedication to teaching and scientific research.

I would like to thank to my master supervisor, Prof. Dr. Mahmut Göktuğ DRAHOR, who's endeared me to geophysics and added greatly to my graduate experience. It is always pleasure for me to work with him and to be one of his students. I would like to also thank the entire staff members at the Department of Geophysics in Dokuz Eylül University for providing me environment for my geophysical education over the years.

I would like to thank my thesis committee members, Prof. Dr. Talip GÜNGÖR and Asst. Prof. Dr. Mehmet UTKU. They have guided me through all stages of the thesis with their vast knowledge for following my progress and reviewing this thesis. Also, I would like to thank Prof. Dr. GÜNGÖR for his help in carrying out a geological fieldwork for the investigation of detailed site condition of stations and producing of geological cross-section along the linear array stations in Fig. 3.2. I am grateful to Prof. Dr. Raul R. CASTRO for providing his computer codes. I also wish to thank him and Prof. Dr. Brian J. MITCHELL for their comments and suggestions which significantly improved the published manuscripts. I would like to thank Dr. N. Bozkurt ÇİFTÇİ for providing location map showing the main tectonic elements around the Aegean extensional province and simplified geologic map of the western Anatolia region.

I would like to thank my parents for supporting me in every important step in my life. Most of all, I would like to offer the biggest thanks to my beloved spouse Duygu KURTULMUŞ. Without her endless patience and support, the completion of this

thesis would be impossible. Finally, I would like to dedicate this thesis to my little daughter, Alya, who is impatiently awaited to join our family.

This study is supported by DEU Scientific Research Foundation Grant BAP-Project No: 2008.KB.FEN.08.

Tevfik Özgür KURTULMUŞ

INVESTIGATION OF SOURCE, SITE, REGIONAL AND NEAR SURFACE ATTENUATION CHARACTERISTICS IN THE WESTERN ANATOLIA REGION

ABSTRACT

Recordings of micro- and moderate-size local earthquakes have been used to estimate source, site, regional and near-surface attenuation effects on the horst-graben system in the western Anatolia region, Turkey. Firstly, site effect estimates were carried out by two different spectral ratio methods (Horizontal to Vertical Spectral Ratio, HVSR, and Standard Spectral Ratio, SSR). Epicentral distance, magnitude and back-azimuth dependencies of transversal component HVSR site functions were examined to see data distribution effect. Secondly, a series of generalized inversion technique (GIT) were applied to the data to separate source, path and site effects for the region. The attenuation functions, including anelasticity and geometrical spreading effects, were obtained using a non-parametric approach for transversal, radial and vertical components. Quality factor and geometrical spreading coefficients were obtained and parameterized from these attenuation functions, for three different distance ranges to separate deeper and longer ray path effects from shallow and near ones. Thirdly, after eliminating attenuation function effect from the spectra, source and site functions were decomposed. Site functions from transversal components by three different approaches were also compared. Finally, the near-surface attenuation parameter of each site was estimated.

The results imply that the site effect distributions of graben/basin fill thicknesses reflect geological complexities caused by basin geometry and edge effects in the region. Large amplitudes of V-component GIT site estimates are observed at varying frequency ranges for different site conditions. This means that the vertical component of motion is influenced by the local structure and may cause contamination of spectral ratio site estimates. Attenuation estimates reveal that both quality factor and geometrical spreading coefficients are strongly frequency dependent especially for large distances. *Q* anisotropy is also observed between

transversal and radial components for large hypocentral distance ranges. All of the results will shed light on the seismic hazard assessments for the region.

Keywords: Site function, horizontal to vertical spectral ratio, standard spectral ratio, generalized inversion, source function, regional and near-surface attenuation, geometrical spreading, quality factor *Q*, Western Anatolia, Turkey.

BATI ANADOLU BÖLGESİ'NDE KAYNAK, ORTAM, BÖLGESEL VE YEREL SÖNÜM ÖZELLİKLERİNİN İNCELENMESİ

ÖZ

Küçük ve orta büyüklükteki yerel deprem kayıtları kullanılarak; Türkiye, Batı Anadolu, horst-graben sistemi için kaynak, zemin, bölgesel ve yerel sönüm etkileri kestirilmiştir. İlk olarak, zemin etkisinin belirlenmesi için iki farklı spektral oran yöntemi (Yatay/Düşey Spektral Oran, YDSO ve Standart Spektral Oran, SSO) uygulanmıştır. Veri dağılımının sonuçlar üzerindeki etkisini görmek için transvers bileşen YDSO zemin fonksiyonlarının; episantr uzaklığı, büyüklük ve ters-azimut bağımlılıkları incelenmiştir. İkinci olarak, bölge için kaynak, ortam ve zemin etkilerini ayrıştırmak amacıyla veriye bir seri genelleştirilmiş ters çözüm (GTÇ) uygulanmıştır. Anelastik sönüm ve geometrik yayılma etkilerini içeren soğurma fonksiyonları, parametrik olmayan bir yaklaşım kullanılarak, transvers, radyal ve düşey bileşenler için elde edilmiştir. Soğurma fonksiyonları kullanılarak, derin-uzak etkiler ile sığ-yakın etkileri ayırt etmek amacıyla üç farklı uzaklık aralığı için anelastik sönüm ve geometrik yayılma değerlerine ulaşılıp, parametrelerle ifade edilmiştir. Üçüncü olarak, spektrumlardan soğurma fonksiyonları etkisi giderildikten sonra, spektral kaynak ve zemin fonksiyonları ayrıştırılmıştır. Ayrıca, üç farklı yöntem ile elde edilen transvers bileşen zemin fonksiyonları karşılaştırılmıştır. Son olarak, her bir zemin için yerel sönüm parametresi kestirilmiştir.

Sonuçlar graben/havza dolguları üzerindeki zemin büyütme dağılımlarının bölgedeki havza geometrisi ve havza kenar etkilerinden kaynaklanan jeolojik karmaşıklıkları yansıttığını işaret etmektedir. Farklı zeminlerde değişen frekans aralıklarına bağlı büyük genliklere sahip düşey bileşen GTÇ zemin fonksiyonları elde edilmiştir. Bu, hareketin düşey bileşeninin yerel zemin koşullarından etkilendiği ve spektral zemin fonksiyonlarının kestirilmesinde karışıklığa neden olabileceği anlamına gelmektedir. Soğurma kestirimleri hem anelastik sönüm hem de geometrik yayılma katsayısının özellikle uzak mesafelerde kuvvetli bir biçimde frekans bağımlı olduğunu ortaya koymuştur. Ayrıca büyük hiposantr mesafelerinde transvers ve

radyal bileşenler arasında *Q* anizotropi görülmektedir. Elde edilenlerin tümü, bölge için gerçekleştirilecek sismik tehlike değerlendirmelerine ışık tutacaktır.

Anahtar kelimeler: Zemin büyütmesi, yatay/düşey spektral oran, standart spektral oran, genelleştirilmiş ters çözüm, kaynak fonksiyonu, bölgesel ve yerel sönüm, geometrik yayılma, kalite faktörü *Q*, Batı Anadolu, Türkiye.

CONTENTS

LIST OF FIGURES

Pages

LIST OF TABLES

Pages

CHAPTER ONE
INTRODUCTION

1.1 Objective and Scope

The central west Turkey has experienced extensional tectonics since Late Oligocene times (e.g., Gessner et al., 2001; Seyitoğlu & Işık, 2009) and extension in the mid- and upper-crust is mainly accommodated by large displacement along low-angle detachment faults (Gessner et al., 2001; Hetzel et al., 1995). Deformation of the crust with increasing lithospheric thinning has been characterized by intense seismic activity (e.g., Le Pichon et al., 1995; Taymaz et al., 1991), extensive volcanism (e.g., Aldanmaz, 2006; Tokçaer et al., 2005), mineralization (e.g., Sayın, 2007; Yılmaz, 2007), geothermal systems (e.g., Mutlu, 2007; Tarcan et al., 2000), the high heat flow- (e.g., Göktürkler et al., 2003; İlkışık, 1995) and low Pn-values (e.g., Al-Lazki et al., 2004; Mutlu & Karabulut, 2011) around the horst-graben system in the central west Turkey. Approximately E-W trending main grabens contain deep sedimentary sequences with thicknesses being more than 3000 m in some localities (e.g., Çiftçi & Bozkurt, 2009; Çiftçi et al., 2010; Sarı & Şalk, 2006).

Site amplification in deep basin structures is one of the important factors that control damage in urban areas from the earthquakes. Thus, determination of deep sedimentary basin/graben site effects is a very important issue for the seismic hazard assessments. Several studies have demonstrated the role played by the surface geology in altering observed seismic motions (e.g., Bindi et al., 2009; Cadet et al., 2012; Castro et al., 2004; Parolai et al., 2004). The amplitude and frequency content of the ground motions from an earthquake can be greatly affected by properties such as impedance contrasts, and configuration of the near surface materials via mechanisms such as selective filtering including resonance frequency, damping and focusing. Moreover, seismic hazard calculations utilize an attenuation function and soil amplification factors. The first one includes the effects of ruptures and crustal structure; and the second one was generated by surface geology, soil column thickness and soil nonlinearity (Akyol et al., 2013). Although there are a lot of site effect related studies for northwest Turkey (e.g., Özalaybey et al., 2011; Parolai et al., 2004), site effect related papers (e.g., Eskişar et al., 2013) are missing for the central west Turkey.

Describing not only site effect but also source and path effects is significant in terms of both assessing the seismic hazard in a specific region and generation of the building codes/or renewing previous ones. Obtaining of a detailed knowledge on the expected spectral ground motion models provide us simulation of time histories of possible earthquakes and design of earthquake resistant structures at a site of interest (Oth, 2007). Because of the high seismicity accommodating crustal deformation and stratigraphic conditions, on which have, urbanized and industrialized large cities in the central west Turkey, the importance of site-specific seismic hazard assessments becomes more crucial. For that reason, the main goal of this study is to separate source, site and regional/near-surface attenuation effects for the region.

The WASRE (Western Anatolia Seismic Recording Experiment) network data, collected in between November 2002 and October 2003 by the project of TÜBİTAK (YDABAG/102Y015) – NSF (NSF-INT-0217493) collaboration, was used in this study. To better understand the crust/upper mantle structure and the details of earthquake activity in western Anatolia, Saint Louis University (USA) and Dokuz Eylül University in Izmir (TURKEY) carried out a cooperative project entitled *"Integrated Seismological Studies of Crust/Upper Mantle Structure and Anisotropy in Western Anatolia"* (Akyol et al., 2006; Zhu et al., 2006a; 2006b).

The empirical methodologies commonly used for site effect assessment are non-reference-station technique which is also called as Nakamura (Nakamura, 1989) or "Horizontal to Vertical Spectral Ratio, HVSR" and "Standart Spectral Ratio, SSR" (Borcherdt, 1970). HVSR hypothesizes that the vertical component of motion is amplification free and not influenced by the local structure, whereas the horizontal components contain P-to-S conversions due to the local geological features around station (Parolai et al., 2004). SSR method assumes that the hard-rock site is transparent and has no site complexity of its own, and so, spectral ratio between the ground motions recorded at a site of interest and a nearby hard-rock site for the same source (e.g., Bonilla et al., 1997; Rogers et al., 1984) represents site transfer function. SSR method depends on the availability of an adequate reference site. Such a site may not be always available. The advantage of HVSR method is estimation of resonance frequency with low-cost, single station measurements. On the other hand, many researchers agree that 2D or 3D effects and low impedance contrast between sediments and basement can preclude HVSR applications (e.g., Parolai et al., 2004; Yalçınkaya et al., 2013).

In this study, firstly, site functions of 32 different locations were obtained by HVSR method from R-components of ground motions and compared with the ones from T-components (Çamyıldız, 2008). Additionally, the distance, magnitude and back-azimuth dependencies of the T-component HVSR estimates were evaluated to investigate data distribution effect on the results. Site functions were also obtained using SSR approaches and the results were compared in order to evaluate the differences between two different spectral ratio estimates.

Another fundamental requirement for seismic-hazard assessment is accurate knowledge of seismic attenuation and its frequency dependence (Sonley & Atkinson, 2006). Seismic attenuation is a significant quantity that affects the distribution of seismic waves travelling into the Earth and provides valuable information on the underground structure. It describes decrease in amplitude and change in frequency content of the seismic waves with distance. This amplitude decay may originate from geometrical spreading, energy absorption, and/or scattering (Erdik & Durukal, 2003). Determination of attenuation properties in a specific region is necessary in terms of shedding new light on the distribution of intensities of the previous strong earthquakes and understanding the implications of a possible earthquake (Oth et al., 2009). Up to now, seismic attenuation properties of west/northwest Turkey have been studied utilizing different kinds of waves and methods. For instance Akıncı et al. (1994) measured the attenuation of coda waves in west Turkey as a function of lapse time for a broad set of lapse times (30-190 s). They observed that the average coda quality factor Q_c depends strongly on lapse time and frequency. Several other researchers investigated the attenuation mechanism in west/northwest Turkey (e.g., Akıncı et al., 1995a, 1995b, 2004; Akyol et al., 2002a; Bindi et al., 2006), southwest Turkey (e.g., Şahin et al., 2007, 2013; Şahin, 2008) and the Marmara region (e.g., Horasan et al., 1998; Horasan & Boztepe-Güney, 2004; Kaşlılar-Özcan et al., 2002).

The common approach to separate the earthquake source processes, path effects and site amplification is to apply Generalized Inversion Technique (GIT) to the recorded ground motion data. GIT was first proposed by Andrews (1986) and developed by many researchers with different algorithms (e.g., Boatwright et al., 1991; Castro et al., 1990; Hartzell, 1992). In this thesis, the attenuation functions including anelasticity of heterogeneous media and geometrical spreading effects were obtained for T-, R- and V-component of the ground motions, using a non-parametric approach described by Castro et al. (1990). Utilizing another inversion step, these functions were parameterized *Q(f)* and *b(f)* values for three different distance ranges (10-200 km, 10-70 km and 120-200 km) to separate deeper and longer ray path effects from shallow and near ones.

After eliminating obtained attenuation functions effect and utilizing another inversion step, source and site spectral functions were decomposed from the spectra. GIT site estimates were compared with the HVSR estimates to examine whether or not there is any contamination effect of vertical motion on the site transfer function results. The decomposition of source and site spectral functions was also applied to two subsets of the data in order to see data distribution effect on the results. Finally, the near-surface attenuation parameter (κ) of the station sites was evaluated by utilizing the original method of Anderson & Hough (1984). This parameter is another quantity needed for seismic-hazard assessment and describes the asymptotic high frequency slope of the spectra (Kilb et al., 2012).

1.2 Thesis Outline

If we look at the concepts of this thesis, Chapter 2 presents general tectonic, geologic setting and seismicity of the central west Turkey. Characteristics of the network, stations, data and also initial data processing stages are presented in Chapter 3. The data from 436 earthquakes, recorded by 32 different locations have been used to quantify site effects of basin/graben structures in the region. Chapter 4 includes site function estimations from spectral ratio approaches, starting with a short introduction to meaning of the site effect and also information about HVSR and SSR methods. The distance, magnitude and back-azimuth dependencies of T-component HVSR estimates were also given. Chapter 5 includes separation of source, site and regional attenuation effects for three components by utilizing GIT and starts with theoretical information about the technique and fundamental seismological concepts of propagation characteristics. Some restrictions are applied to the data to improve the resolution of inversion processes, and so the remaining 322 events with 1764 three-component recordings were evaluated in this stage. Thus, data distribution was given again. In this chapter, non-parametric attenuation functions for T-, R- and V-components were parameterized to obtain $Q(f)$ and $b(f)$ values for three different distance ranges (10-200 km, 10-70 km and 120-200 km). Utilizing another inversion step, source and site spectral functions were decomposed not only for all-dataset but also for two subsets of the data. Finally, the near-surface attenuation parameter (κ) of the station sites was evaluated from T-component spectra. General discussions on the results are given in Chapter 6. Finally, the thesis ends with the main conclusions and recommendations in Chapter 7.

CHAPTER TWO
GENERAL TECTONIC, GEOLOGIC SETTING AND SEISMICITY

2.1 Tectonic Setting of the Region

Neotectonics in Anatolia (Turkey) that located in the Alpine–Himalayan orogenic belt are caused mainly by northward movement of the Arabian plate towards Eurasia (McKenzie, 1972). As a consequence of this collision, the Anatolian microplate extrudes westward away from the eastern Anatolia along the North Anatolian Fault Zone (NAFZ) and East Anatolian Fault Zone (EAFZ), respectively (Bozkurt, 2001). In addition, the northward subduction of African lithosphere along the Aegean Subduction Zone (ASZ) plays an important role in the tectonic development of the region (Biryol et al., 2011). The dextral NAFZ, sinistral EAFZ, the Aegean-Cyprean Arc and sinistral Dead Sea Fault Zone are the major structural elements that give rise to lithospheric deformation throughout Anatolia (Fig. 2.1). This ongoing complex deformation has resulted in four neotectonic provinces such as the East Anatolian contractional, the North Anatolian, the Central Anatolian and the West Anatolian extensional provinces in Turkey (Şengör et al., 1985).

The central part of west Turkey has experienced extensional tectonics since Late Oligocene times and the region includes a well developed metamorphic core complex, the Menderes Massif (e.g., Gessner et al., 2001; Seyitoğlu & Işık, 2009). Although the origin of the regional extension is still being debated; the crustal extension is related to the westward extrusion of the Anatolian Plate (Tectonic escape model; e.g., Dewey & Şengör, 1979; Şengör, 1979), subduction along the Hellenic arc (Back-arc spreading model; e.g., Le Pichon & Angelier, 1979; McKenzie, 1978) and the spreading and thinning of over-thickened crust following the latest Palaeocene collision across the Neotethys (Orogenic collapse model; e.g., Seyitoğlu & Scott, 1991; 1992). In the tectonic escape model, it is assumed that the N–S extension is related with the westward extrusion of the Anatolian microplate away from the zone of collision between the Arabian and Eurasian plates along the Bitlis-Zagros suture zone. According to this model, westward tectonic escape of

Anatolia towards the Aegean Sea has begun 12 Ma ago (e.g., Dewey & Şengör, 1979; Şengör, 1979). It is proposed that the combination of back-arc spreading (rifting) behind a Tethyan subduction zone to the south and subduction rollback accompanied by the subduction along the Aegean-Cyprian trench gave rise to an extensional regime in the region. Another idea widely accepted for the origin of the extension in the western Anatolia is the orogenic collapse model. This model suggests that the N-S extension is related to the spreading and thinning of over-thickened crust following suturing of the Neotethys Ocean. The orogenic collapse is inherited from Paleocene-Eocene closure of the northern branch of Neotethys (Çiftçi et al., 2010).

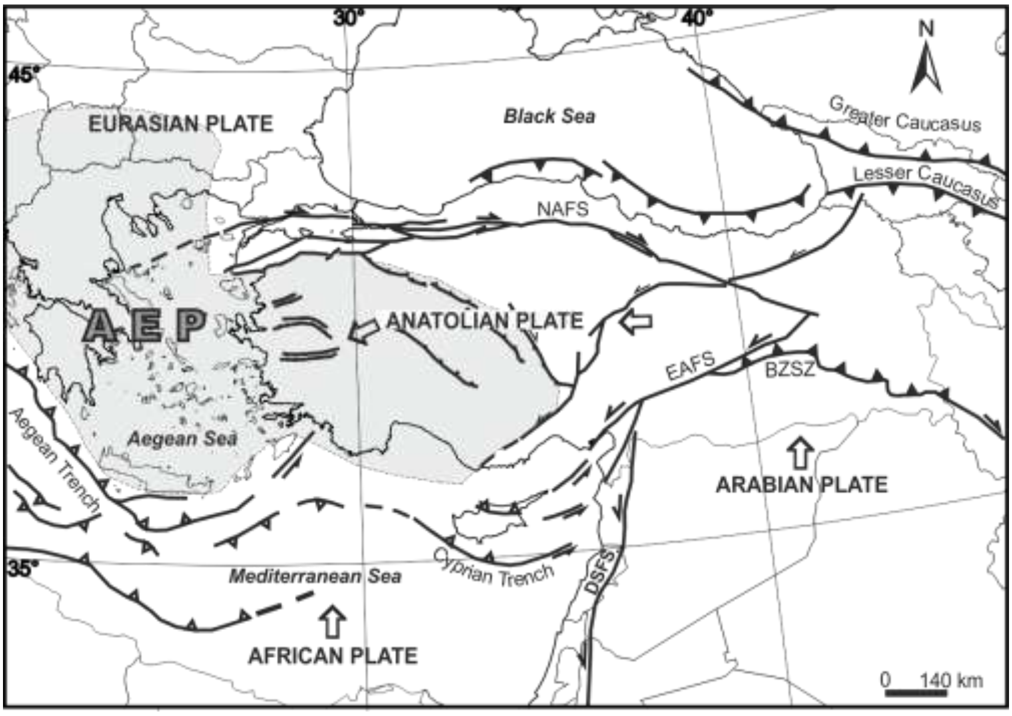

Figure 2.1 Simplified tectonic map of Turkey showing major neotectonic structures. AEP: Aegean extensional province, NAFS: North Anatolia fault system, EAFS: East Anatolia fault system, BZSZ: Bitlis Zagros suture zone, DSFS: Dead Sea fault system (after Çiftçi et al., 2010).

Despite of several controversies among different schools of thoughts, there is now a consensus that the NS-oriented continental extension in the region commenced by the latest Oligocene-Early Miocene time. Miocene time is expressed by two distinct structural styles: Miocene core-complex formation and Plio-Quaternary modern graben formation. It is most likely that the former has resulted from the combined effects of both orogenic collapse and back-arc extension, while the latter results from a combined effect of slab pull along the Aegean-Cyprian trench system and westward escape of the Anatolian Plate along its bounding structures, the North and East Anatolian Fault zones (Bozkurt & Mittwede, 2005). But there is still no consensus on whether the two distinct structural styles represent a single continuous or episodic extension (Çiftçi & Bozkurt, 2009; 2010).

Although the origin, timing of initiation, geometry and evolution of the major extensional features is still debated, it is known that post-collisional extension in the Aegean Extensional Province caused several Alpine metamorphic massifs to be exhumed. Jolivet et al. (2013) stated that the extension started with the formation of the Rhodope Metamorphic Core Complex since Eocene times and migrated to the Cyclades and the northern Menderes Massif from Oligocene to Miocene. It is accommodated by crustal-scale detachments and a first series of core complexes (Metamorphic Core Complexes-MCCs). Extension then localized in western Turkey, the Corinth Rift and the external Hellenic arc after Messinian times, while the NAF penetrated the Aegean Sea (Fig. 2.2).

Pn values were reported for the region (e.g., Hearn & Ni, 1994; Hearn, 1999; Papazachos et al., 1995) lower (7.5-8.1 km/s) than the worldwide average continental upper-mantle P_n velocity of 8.1 km/s (Mooney & Braile, 1989). This low P_n velocity distribution beneath the Aegean and western Turkey might also be an indicator of high upper mantle temperatures (Hammer et al., 2000) or a very thin to absent mantle lid, where P_n propagation is actually sampling asthenospheric rather than lithospheric mantle (Al-Lazki et al., 2004). Recently, Mutlu et al. (2011) computed P_n velocity distributions and estimated crustal thickness variations for Turkey and adjacent regions. They observed relatively uniform P_n velocities (7.9-8.1 km/s) for western

Turkey. They concluded that large Pn anisotropy is observed in the Aegean, central Anatolia and along the southern coast of Anatolia. The direction of the anisotropy in the Aegean Sea is consistent with the results of geodetic measurements and SKS splitting directions, aligned on the N-S direction in the extensional regime of west Turkey.

Recent studies on the crustal seismic properties of the region indicate that crustal thickness ranges between 28 and 35 km (e.g., Di Luccio & Pasyanos, 2007; Kalafat et al., 1987; Saunders et al., 1998; Sodoudi et al., 2006; Zhu et al., 2006a). Zhu et al. (2006a) obtained detailed crustal image for the central Menderes Massif. Their results showed that general trend of crustal thinning decreases westward from central Anatolia (36 km) to the central Menderes Massif (28-30 km) and beneath the Aegean Sea (25 km). The results also indicate that crustal thinning in the Aegean is not uniform in the N-S extensional direction. The crust is thinner in the central Menderes Massif (28-30 km of crustal thicknesses) and the Cycladic Massif (25-26 km) than in surrounding regions where crustal thicknesses are 32-34 km. Mutlu (2012) obtained crustal thicknesses range between 28±2 and 33±2 km for west Turkey and the Aegean Sea, respectively.

According to Jolivet et al. (2013), most of available models handle that the continental Aegean lithosphere is often treated as a stack of homogeneous layers and they have not taken into account complex tectonic history. Therefore, these models are insufficient to explain the inherited mechanical anisotropy of the continental crust. They also stated that the extrusion of Anatolia and the Aegean extension is at least partly controlled by underlying asthenospheric flow, whereas it is driven from the extrusion of a lid of rigid crust. Similarly, Le Pichon & Kreemer (2010) argue the role played by the asthenospheric flow in driving crustal deformation.

The eastern Mediterranean region has been subjected to the study of mechanics of the continental lithosphere more than 30 years. At first, it is generally proposed that most of the neotectonic activities in Anatolia were caused by the northerly movement of the Arabian plate towards Eurasia (McKenzie, 1972). However, recent GPS measurements have revealed a more complicated picture of contemporary deformation in the Aegean. The deformation is not uniform but is concentrated in zones separating a few near-rigid blocks. McClusky et al. (2000) found that the central and southern Aegean moves coherently toward the SW at 3 cm/year relative to Eurasia and the motion is accommodated by strike-slip and extension in the North Aegean and N-S extension in west Turkey. With increasing a precise present-day velocity field measurements by satellite geodesy, the present-day regional kinematics in the eastern Mediterranean dominated by a circular counterclockwise motion. The present-day motion of Anatolia increases toward the Aegean and the Hellenic subduction zone (Le Pichon & Kreemer, 2010). The GPS velocity field with a fixed Eurasia (Fig. 2.3) is compatible with the active extension (Jolivet et al., 2013). The current extension at the central west Turkey in N-S direction proceeds at a rate of 3-4 cm/year (Le Pichon et al., 1995; Oral et al., 1995).

Different models compatible with the current GPS data have been suggested for Turkey and surroundings. All models basically agree on the rigid motion of the main part of Anatolia about an Eulerian pole north of the Egyptian coast (Jolivet et al., 2013). Nyst & Thatcher (2004) suggested that present day Aegean deformation in both central Turkey and the central and southern Aegean can be characterized by relative motions of four rigid microplates as central Greece, the Sea of Marmara, the South Aegean, and Anatolia blocks. They also stated that west Turkey is under significant N-S extension. The strain rates were estimated to be 47 nanostrain/year extension at N27°E and 15 nanostrain/year contraction at N63°W. As opposed to block modeling, a model using fracture mechanics and a propagating strike-slip fault (e.g., Flerit et al., 2004) and continuum deformation models (e.g., England, 2003; Floyd et al., 2010) also have been suggested.

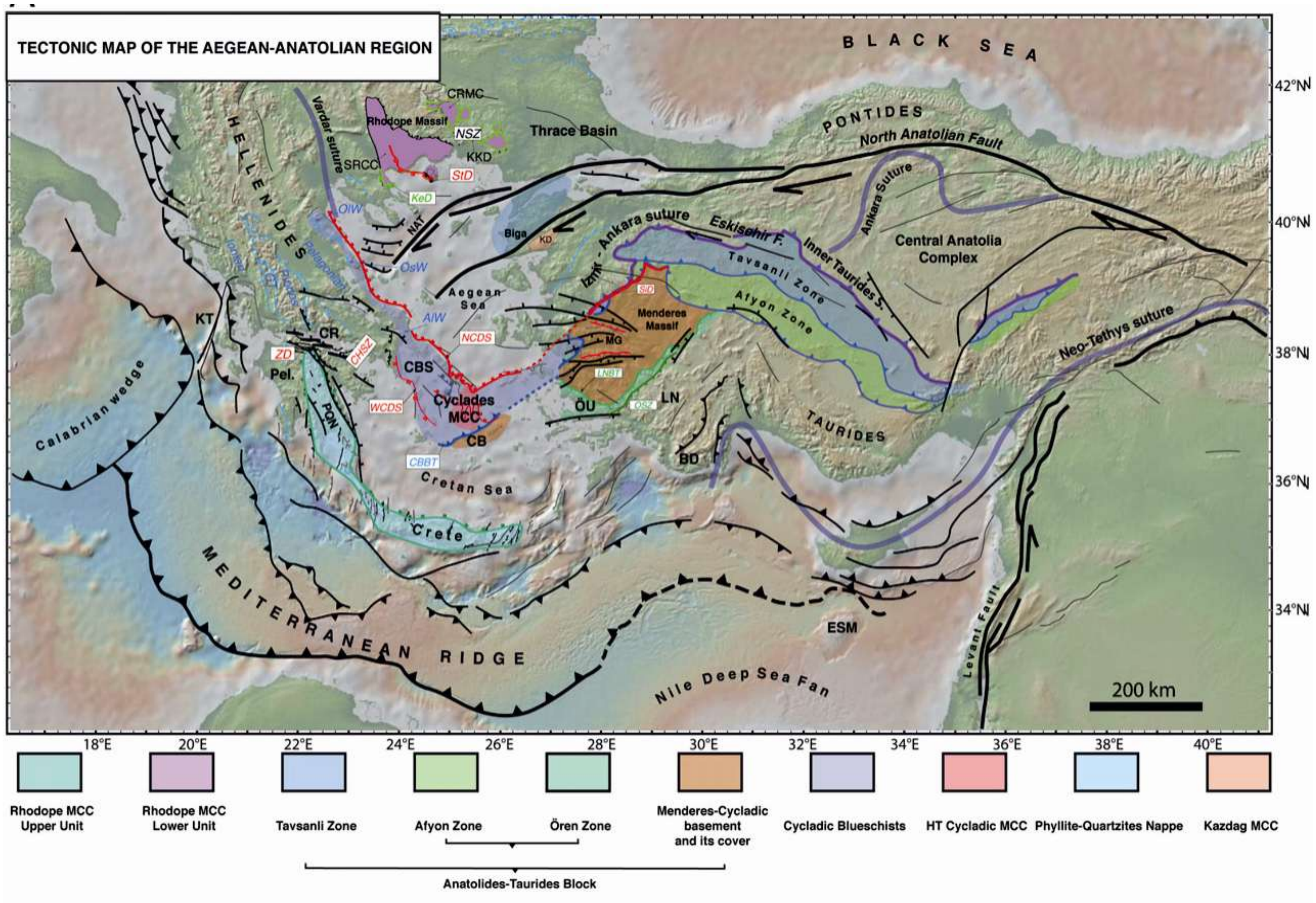

Figure 2.2 Tectonic map of the Aegean and Anatolian region showing the main active structures (black lines), the main sutures zones (thick violet or blue lines), the main thrusts in the Hellenides where they have not been reworked by later extension (thin blue lines), the North Cycladic detachment (NCDS, in red) and its extension in the Simav detachment (SD), the main metamorphic units and their contacts; AlW: Almyropotamos window; BD: Bey Dağları; CB: Cycladic basement; CBBT: Cycladic basement basal thrust; CBS: Cycladic blueschists; CHSZ: Central Hellenic shear zone; CR: Corinth Rift; CRMC: Central Rhodope metamorphic complex; GT: Gavrovo–Tripolitza Nappe; KD: Kazdağ dome; KeD: Kerdylion detachment; KKD: Kesebir–Kardamos dome; KT: Kephalonia transform fault; LN: Lycian nappes; LNBT: Lycian nappes basal thrust; MCC: Metamorphic core complex; MG: Menderes grabens; NAT: North Aegean trough; NCDS: North Cycladic detachment system; NSZ: Nestos shear zone; OlW: Olympos window; OsW: Ossa window; OSZ: Ören shear zone; Pel.: Peloponnese; ÖU: Ören unit; PQN: Phyllite–Quartzite nappe; SiD: Simav detachment; SRCC: South Rhodope core complex; StD: Strymon detachment; WCDS: West Cycladic detachment system; ZD: Zaroukla detachment; ESM: Eratosthenes Seamount. (after Jolivet et al., 2013).

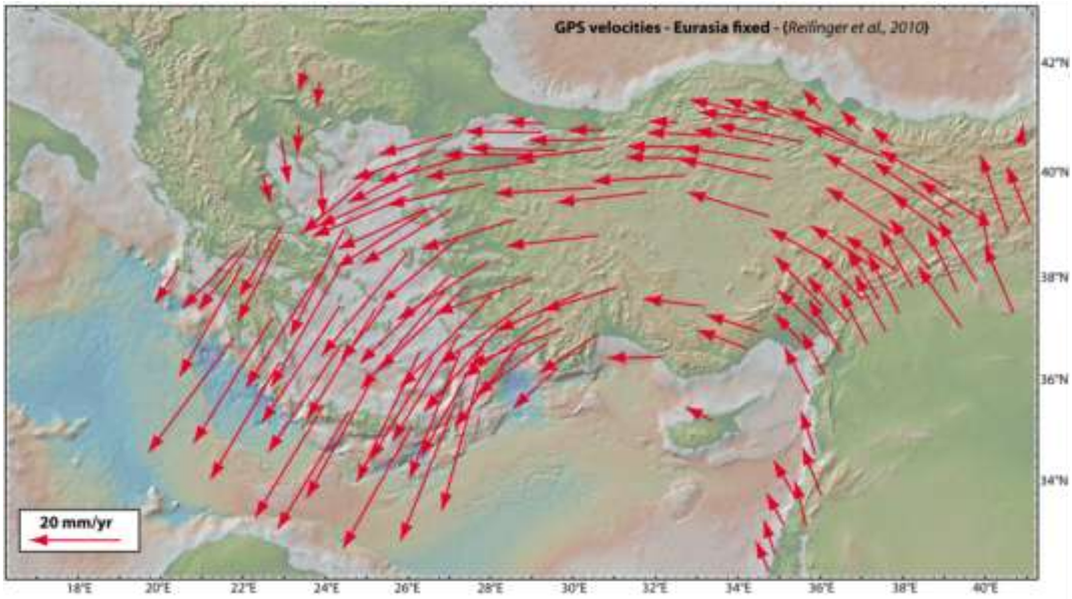

Figure 2.3 GPS velocity field (fixed Eurasia) of Turkey (after Reilinger et al., 2010).

Extension in the mid- and upper crust is mainly accommodated by large displacement along low-angle detachment faults (Gessner et al., 2001; Hetzel et al., 1995). The crustal deformation seen in the form of increasing lithospheric thinning involves intense seismic activity (e.g., Le Pichon et al., 1995; Taymaz et al., 1991), extensive volcanism (e.g., Aldanmaz, 2006; Tokçaer et al., 2005), mineralization (e.g., Sayın, 2007; Yılmaz, 2007) and geothermal systems (e.g., Mutlu, 2007; Tarcan et al., 2000).

2.2 Geology of the Region

The central part of west Turkey has experienced extensional tectonics since Late Oligocene times and the region includes as a well-developed metamorphic core complex (Fig. 2.4), the Menderes Massif (e.g., Gessner et al., 2001; Seyitoğlu & Işık, 2009). The Menderes Massif is one of the Alpine metamorphic belts, where high-grade metamorphic rocks of the middle to lower crust are now exposed. The Menderes massif consists of pre-Cambrian and Paleozoic to Lower Tertiary metamorphic rocks (e.g., Rojay et al., 2005; Şengör et al., 1984). During the Early-Middle Miocene period thick volcano-sedimentary associations were formed within approximately NS-trending fault-bounded continental basins under an E-W extensional regime (Yılmaz et al., 2000) and the massif is divided into northern, central, and southern sections by these EW-trending grabens (Çemen et al., 2006).

Post-collisional volcanism in west Turkey displays compositionally distinct magmatic episodes controlled by slab break-off, lithospheric delamination, asthenospheric upwelling with decompressional melting, and oceanic lithospheric subduction as part of the geodynamic evolution of the eastern Mediterranean region throughout the Cenozoic (e.g., Aldanmaz, 2002; Dilek, 2005; Pe-Piper & Piper, 2001). The Late Miocene volcanism was marked by alkali basalts and basanites erupted along the zones of localized extension in the region during Late Miocene to Quaternary time (e.g., Aldanmaz, 2002; Tonarini et al., 2005). The melt source carried no subduction component, and the main magma source was decompressional melting of the asthenospheric mantle flowing beneath attenuated continental lithosphere in the Aegean extensional province. Lithospheric-scale extensional fault systems provided natural conduits for the transport of uncontaminated alkaline magmas to the surface (Dilek, 2005). Trace-element modeling in the region indicated that the mafic magmas formed by variable degrees (~2%-10%) of martial melting and degree of partial melting decreased progressively from early-formed alkali olivine basalts to later basanites. The isotopically depleted nature of the alkaline rocks relative to bulk silicate earth indicates that this enrichment is a recent event related to small degree, multi-stage melting processes that involve local metasomatism of the mantle (Aldanmaz, 2002).

Active extension in west Turkey caused the formation of some Neogene grabens separated by intervening horst blocks in which the pre-Tertiary basement rocks are exposed (Fig. 2.4) (Çiftçi et al., 2010). Major breakaway faults were also formed during this time and approximately NS-trending cross-grabens were developed. It later cropped out in the Bozdağ Horst, ultimately lying above the upper plate (Şengör, 1987; Yılmaz et al., 2000). The horst-graben system in west Turkey exhibits E-W, NE-SW, and NW-SE trends. The Gediz, Küçük Menderes and Büyük Menderes grabens, separated by the Bozdağ and Aydın Mountain Horsts, are the most prominent neotectonic features of the region (Fig. 2.4). Individual grabens are composite basins and comprise multiple depocenters or subbasins with sediment thicknesses being more than 3000 m in some locations (Çiftçi et al., 2010). The grabens are filled with lower (?)-middle Miocene to Holocene continental fluvial clastics, with minor freshwater carbonates (Çiftçi et al., 2010). Middle Miocene sediments beneath the younger fill at some localities within actively extending grabens in the region (e.g., Bozkurt, 2001, 2003; Koçyiğit et al., 1999) indicate that, when extension began, some normal faults had cut through preexisting depocenters (Westaway et al., 2004). These areas contain a high degree of fracturing and permeability and because of being closer to the heating source, high thermal conductivity. İlkışık (1995) have reported the high average heat flow (107±45 mW/m^2) with geothermal activity in the region.

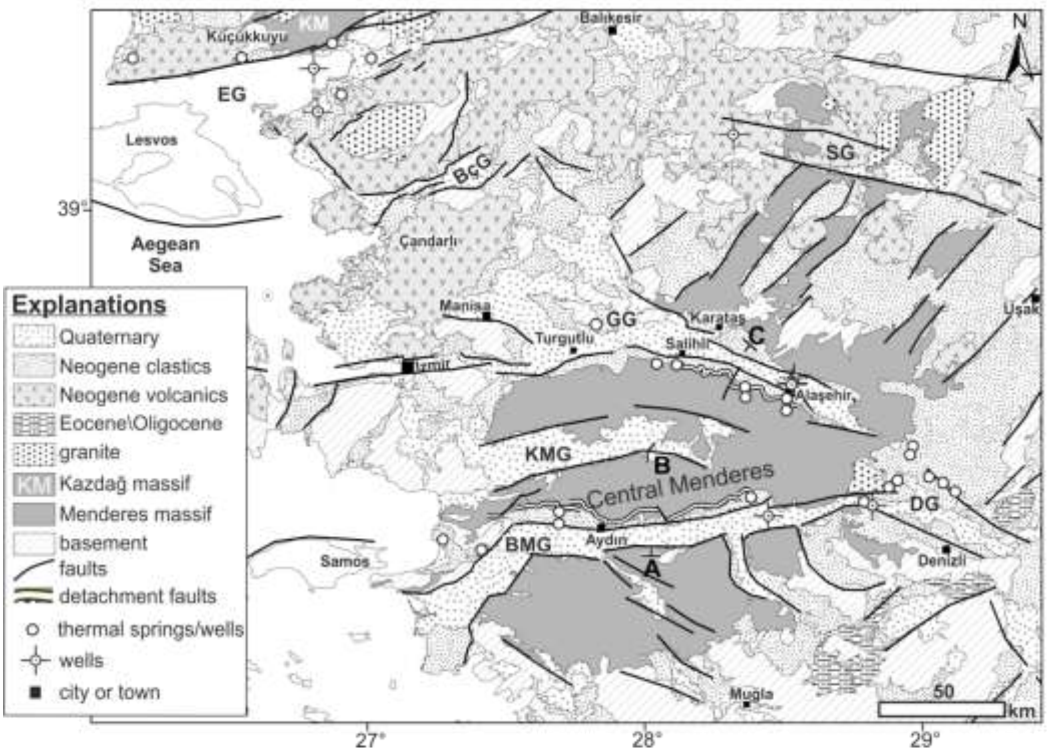

Figure 2.4 Simplified geologic map of the central west Turkey (after Çiftçi et al., 2010). A, B, C represent the location of 2D seismic profiles and inferred subsurface geology along them is given by Çiftçi et al. (2010). EG: Edremit graben; BçG: Bakırçay graben; GG: Gediz graben; KMG: Küçük Menderes graben; BMG: Büyük Menderes graben; DG: Denizli graben; SG: Simav graben.

Two largest grabens (GG and BMG in Fig. 2.4) are located at the northern and southern flanks of the central Menderes massif, respectively. Figure 2.5 shows subsurface geology inferred from 2D seismic profiles along the Büyük Menderes and Gediz grabens (after Çiftçi et al., 2010). As shown in this figure, these flanks have two sets of faults: (1) high-angle normal faults, including the master border faults of the grabens, and (2) shallow-dipping detachment faults. The high-angle normal faults cut the earlier low-angle normal faults. Compared with the other basins in the region, Gediz and the Büyük Menderes grabens contain thick sedimentary sequences (e.g., Çiftçi & Bozkurt, 2009; Gürer et al., 2009; Sarı & Şalk, 2006) displaced bounding faults (Fig. 2.5, after Çiftçi et al., 2010). The Miocene and recent continental clastics in the grabens uncomformably cover the Menderes metamorphics.

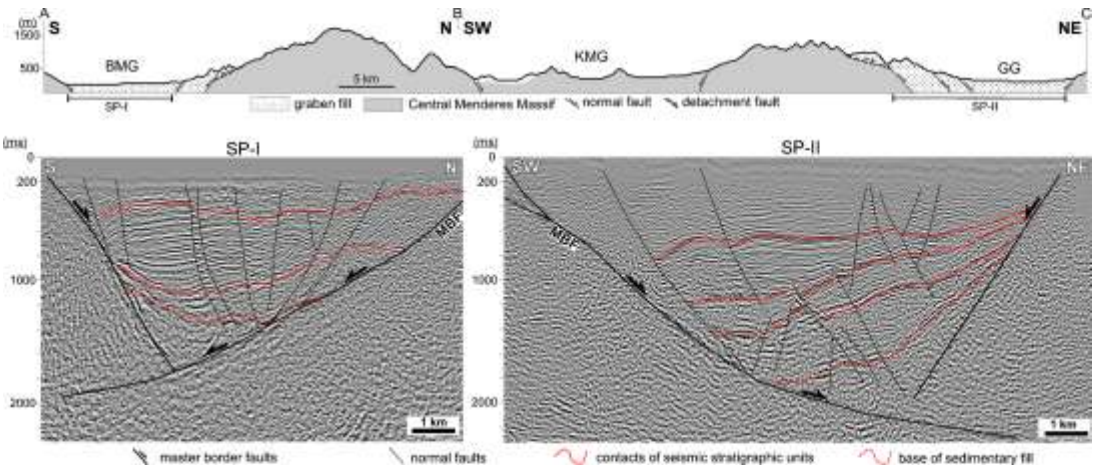

Figure 2.5 Cross section ABC across the central Menderes massif. See Fig. 2.4 for the location of the cross section. Subsurface geology of the Büyük Menderes (BMG) and Gediz grabens (GG) is derived from 2D seismic profiles. Note that the grabens face opposite directions with master border faults (MBF) located at the northern and southern margins of the Büyük Menderes and Gediz grabens, respectively. KMG: Küçük Menderes graben (after Çiftçi et al., 2010).

As a result of tectonic unloading along bivergent detachment faults, the lower plate has flexed upward to form a regional syncline along the central Menderes Massif. Thermochronologic data (Gessner et al., 2001) suggests that this occurred at ~5 Ma. The absence of Neogene deposits along the Küçük Menderes graben suggests that this graben is younger than the others (Rojay et al., 2005) and sedimentary thickness is up to 270 meters in the Ödemiş subbasin. Generalized tectonostratigraphic columnar section of west Turkey grabens is given in Fig. 2.6 (after Rojay et al., 2005). Çiftçi & Bozkurt (2009, 2010), Çiftçi et al. (2010) and Emre et al. (2010) also presented detailed stratigraphic sequences of the graben fills for the region.

2.3 Seismicity of the Region

Based on the historical and instrumental earthquake records, western Turkey is one of the most seismically active regions of the Eastern Mediterranean region. Moderate-sized earthquakes are actually the dominant sources of seismic hazard in the region (Akyol & Karagöz, 2009). Historical seismicity implied that many large earthquakes occurred in the region in BC 17, 60, 110,177, 253, 688, 1389, 1653, 1688, 1739, 1846, 1862, 1873, 1880, 1881, 1983, 1885, 1895, 1899 with the intensities of IX and X (MSK) (Kandilli Obsevatory and Earthquake Research Institute [KOERI], 2014). Instrumental seismicity demonstrates that activity on the faults is shown by numerous earthquakes (e.g., 1919 Soma, M=6.9; 1928 Torbalı, M=6.3; 1933 Gökova, M=6.8; 1956 Söke-Balat, M=7.1; 1965 Salihli, M=5.8; 1969 Demirci, M=5.9; 1969 Alaşehir, M=6.5; 1970 Gediz, M=7.2; 1986; Çubukdağ, M=5.5; 2003 Urla, M=5.8; 2003 Buldan, M=5.4; October 2005 Urla earthquakes swarm with M=5.0, 5.8, 5.5, 5.9).

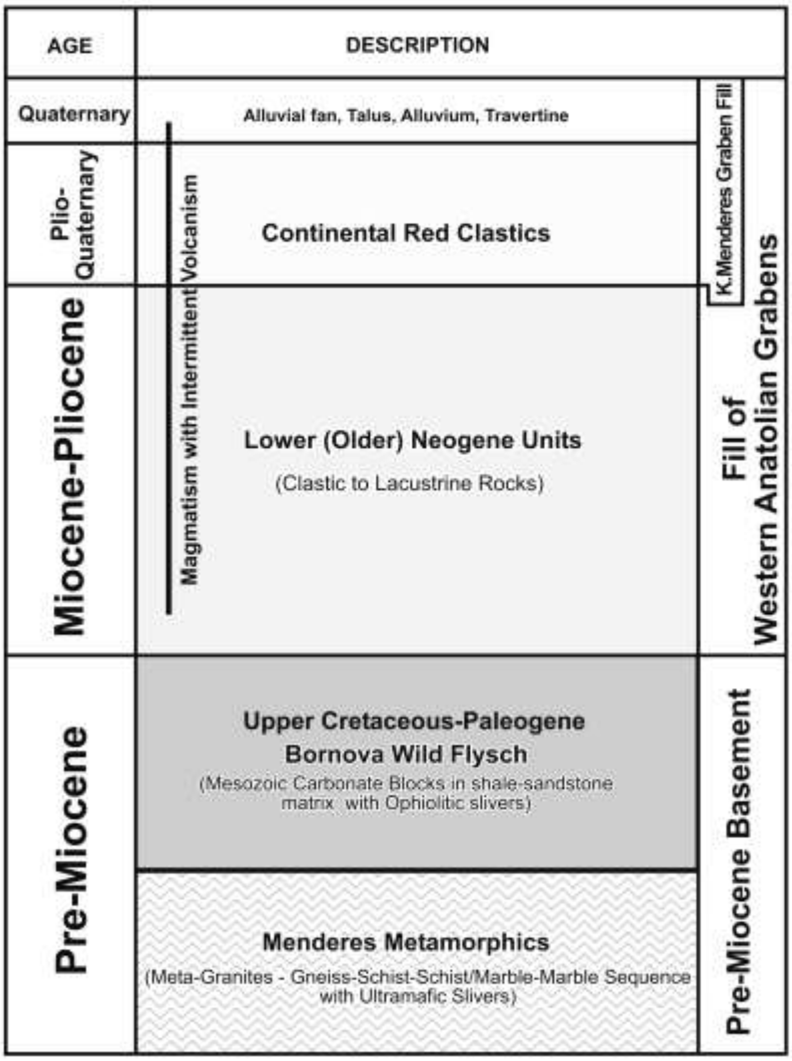

Figure 2.6 Generalized tectonostratigraphic columnar section of the grabens in the central west Turkey (after Rojay et al., 2005).

Figure 2.7 (after Jolivet et al., 2013) shows distribution of the fault mechanisms of normal, strike-slip and reverse earthquakes with magnitude greater than 4 over the Aegean region during 200-2011 period (source: Kiratzi & Louvari, 2003; National Earthquake Information Center [NEIC]). Different colored beach balls in this figure represent different focal mechanisms of the main types of faulting. Early seismic studies in western Turkey showed that most of the fault-plane solutions represent normal faulting and the crust is being stretched (McKenzie, 1978). Tensional axes for these solutions are nearly horizontal and perpendicular to the general E-W trend of graben structure (Sayıl & Osmanşahin, 2008). The region is dominated by N-S extension and crustal thinning, with very little E-W motion (Jackson & McKenzie, 1988). On the other hand, based on the some earthquake data (e.g., Kiratzi, 2002-March 28, 1970 Gediz M 7.1 event) and surface trace observations (Eyidoğan & Jackson, 1985; Yılmaz et al., 2000), strike-slip movements also identified corresponding to NE-SW-trending basins which are predominantly observable between the Gediz and Simav grabens as well as main EW-trending grabens. Zhu et al. (2006a) obtained similar results and they suggested that a small portion of the overall N-S extension is accommodated by slip on two conjugate strike-slip faults. This means that, in addition to crustal thinning by normal faulting, some E-W shortening occurred during the N-S extension.

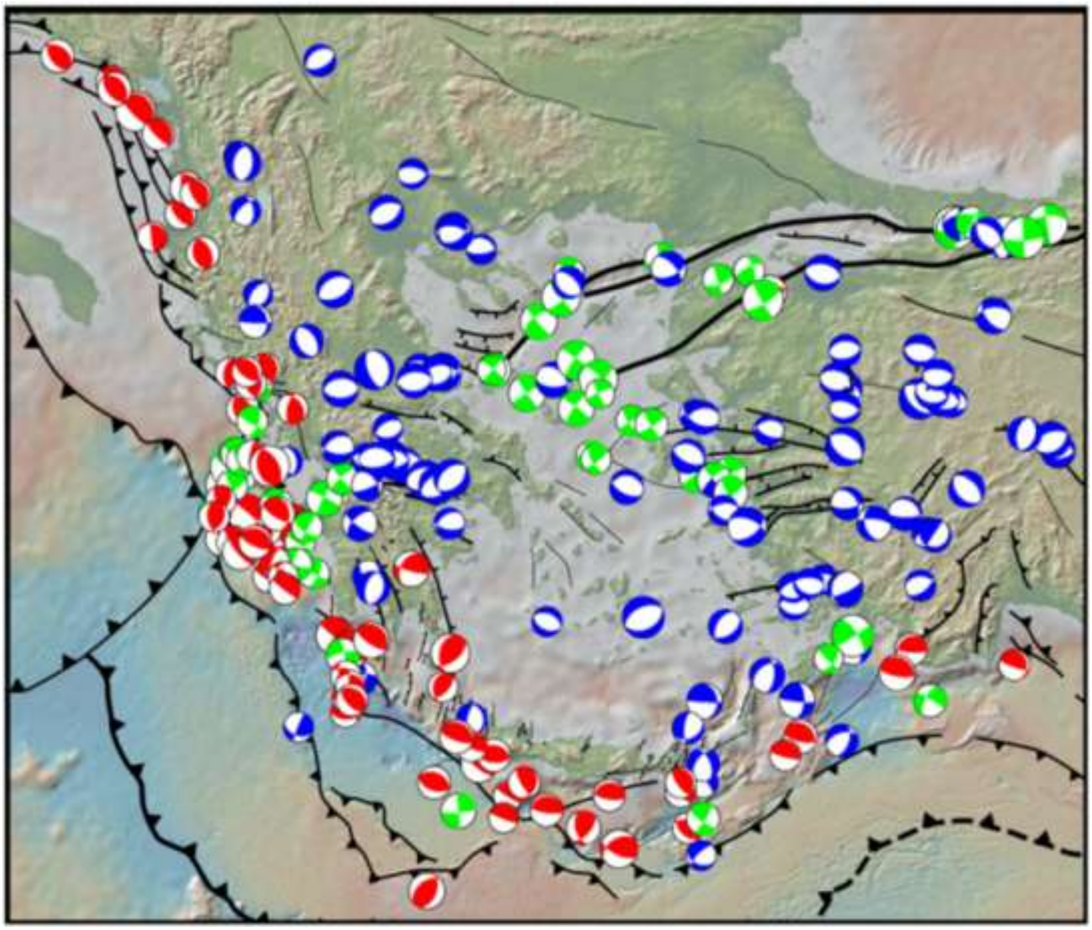

Figure 2.7 Focal mechanisms of earthquakes over the Aegean region. (after Jolivet et al., 2013; Source: NEIC 200-2011 and Kiratzi and Louvari, (2003)). Magnitude of earthquakes is greater than 4. Blue, green and red beach balls depict normal, strike-slip and reverse faults.

The general seismicity of the region is given in Fig. 2.8. Earthquake data are prepared by the catalogue of the KOERI, National Earthquake Monitoring Centre of Bosphorus University during the period between 1900 and 2013. Magnitude scales reported in the catalogue are M_s, M_d, M_b, M_L and M_W. Using the empirical relationships between different magnitude scales (Akyol et al., 2012), all magnitude values in the catalogue were converted to M_L scale. The seismicity of the region is high and displays swarm-type activity with remarkable clustering of low-magnitude earthquakes in time and space (Üçer et al., 1985). Akyol et al. (2006) studied the earthquake activity in west Turkey using the WASRE network data. They found that the seismicity of west Turkey is higher than previously reported. Utilizing a joint inversion scheme, they obtained earthquake locations, 1D P-wave crustal velocity model and station delays for the region. They concluded that velocity model, lower than average continental values, could be associated with high crustal temperatures, a high degree of fracture, or the presence of fluids at high pore pressure in the crust.

Several earthquake hazard studies have been performed in order to identify seismicity in and around the central west Turkey (e.g., Bayrak et al., 2005; 2009; Papazachos, 1999; Polat et al., 2008; Sayıl & Osmanşahin, 2008). Sayıl & Osmanşahin (2008) have been computed Gutenberg-Richter magnitude-frequency relation, seismic risk and recurrence period to investigate the seismicity of western Anatolia (coordinates of 36^o- 40^oN, 26^o- 32^oE). Using the historical and instrumental data, they evaluated 13 sub-regions in west Turkey. Their results showed that a and b values range between *3.19±0.17 - 5.15±0.52* and *0.42±0.05 - 0.66±0.07*, respectively. Bayrak & Bayrak (2012) computed the values of a, b and fractal dimension parameter (D_c) for 15 different seismogenic source zones in western Turkey (the region between 26^o-33^oE and 33^o-40.5^oN) to determine earthquake hazard potential. Regional distributions of these parameters revealed information about variation of stress level and geological complexity. They also pointed out that D_c/b ratios may be used as an indicator of earthquake hazard levels of different seismogenic zones in the region.

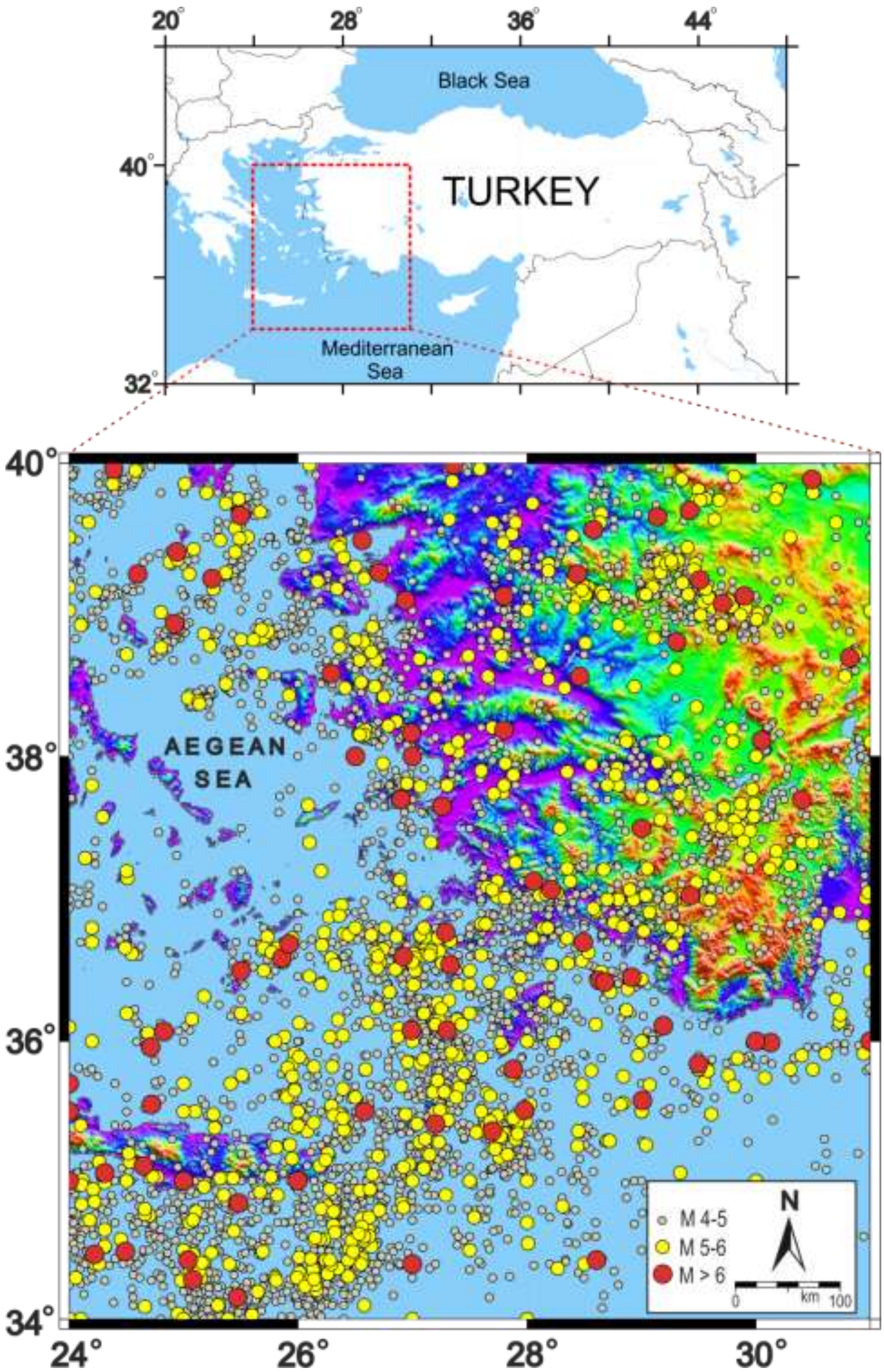

Figure 2.8 Seismicity map of the Aegean Sea and west Turkey region. Earthquake data are prepared by the catalogue of the KOERI, National Earthquake Monitoring Centre during the 1900-2013 period. This figure was produced using public domain software ‘Generic Mapping Tools- GMT’ (Wessel & Smith, 1995).

CHAPTER THREE
DATA ANALYSIS

3.1 Characteristics of the Network and Stations

The WASRE network data (Akyol et al., 2006; Zhu et al., 2006a, 2006b) collected by 5 STS-2 broadband and 24 Mark L-22 short-period (2 Hz) three-component sensors was used in this study. All stations in the network used Reftek 72A recorders to collect 24-bit ground motion data continuously at 40 samples per second. The network consists of two different array configurations during the deployment stage in between November 2002 and October 2003. The first one is Linear Array (LA) which traversed the Gediz Graben (GG), the Büyük Menderes Graben (BMG) and the Küçük Menderes Graben (KMG) with a station spacing of 3–4 km (Fig. 3.1). Twenty of the short-period instruments (ranging from LA01 to LA20) were first deployed for ~5.5 months along ~50-km-long N-S line, and then, eighteen of them (ranging from LA21 to LA38) were redeployed to extend the array southward for remaining ~5.5 months. LA01 and LA20 were deployed during whole data acquisition stage together with the regional array which surrounds the linear array (Fig. 3.1) and consists of four short-period (MAN, NAZ, SAR, SEL) and five broadband instruments (AKH, AYD, BOZ, DEU, KUL). Figure 3.2 shows geological cross-section along the linear array stations. As shown in this figure, the linear array stations were deployed on alluvium, conglomerate-sandstones, gneissic granites and marble-micaschist units. The station list including geological units on which they were deployed was given in Table 3.1 (after Akyol et al., 2013).

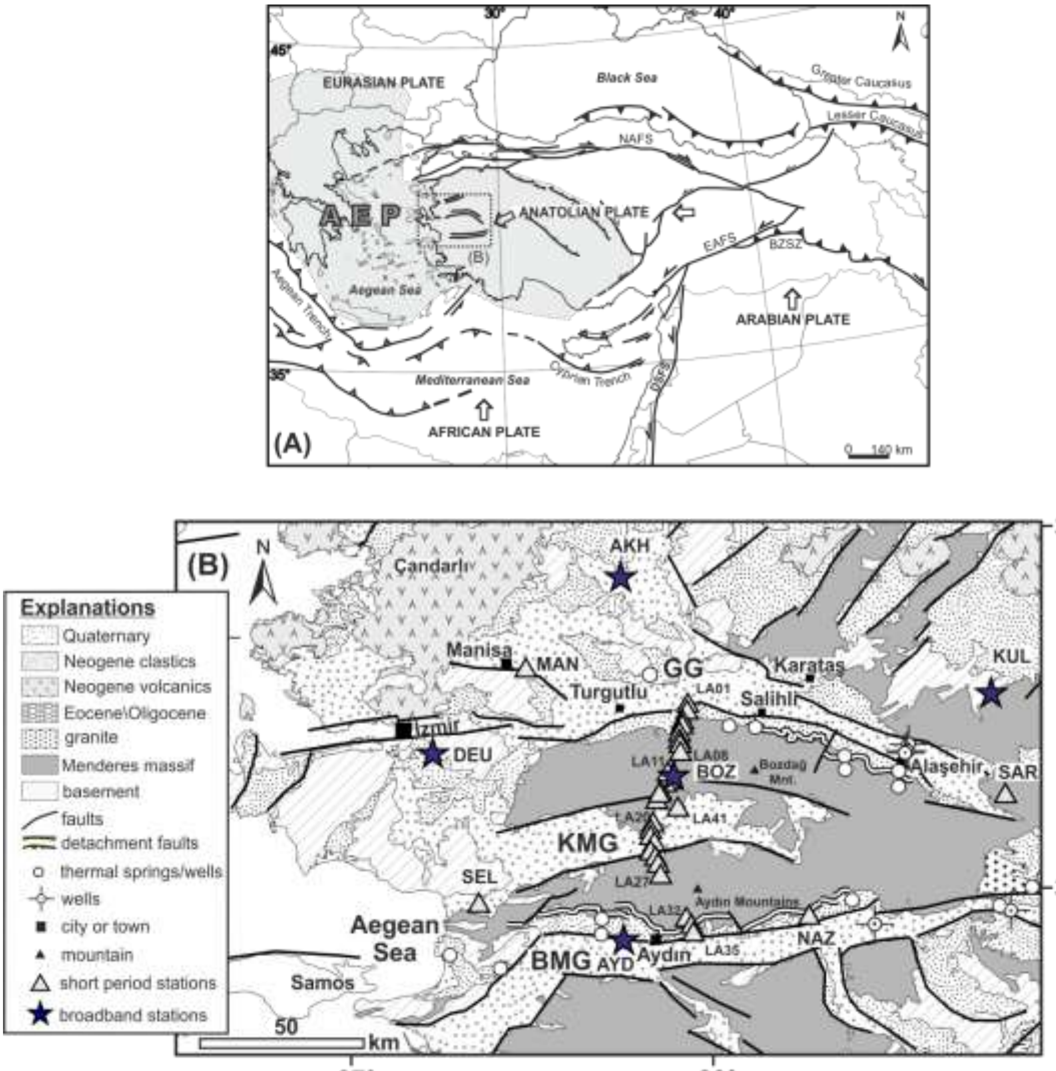

Figure 3.1 A) Simplified tectonic map of Turkey showing major neotectonic structures (after Çiftçi et al., 2010). B) Simplified geologic map of the central west Turkey (after Çiftçi et al., 2010) and stations used in this study. NAFS: North Anatolia fault system; EAFS: East Anatolia fault system; BZSZ: Bitlis Zagros suture zone; DSFS: Dead Sea fault system; EG: Edremit graben; BçG: Bakırçay graben; GG: Gediz graben; KMG: Küçük Menderes graben; BMG: Büyük Menderes graben; DG: Denizli graben; SG: Simav graben.

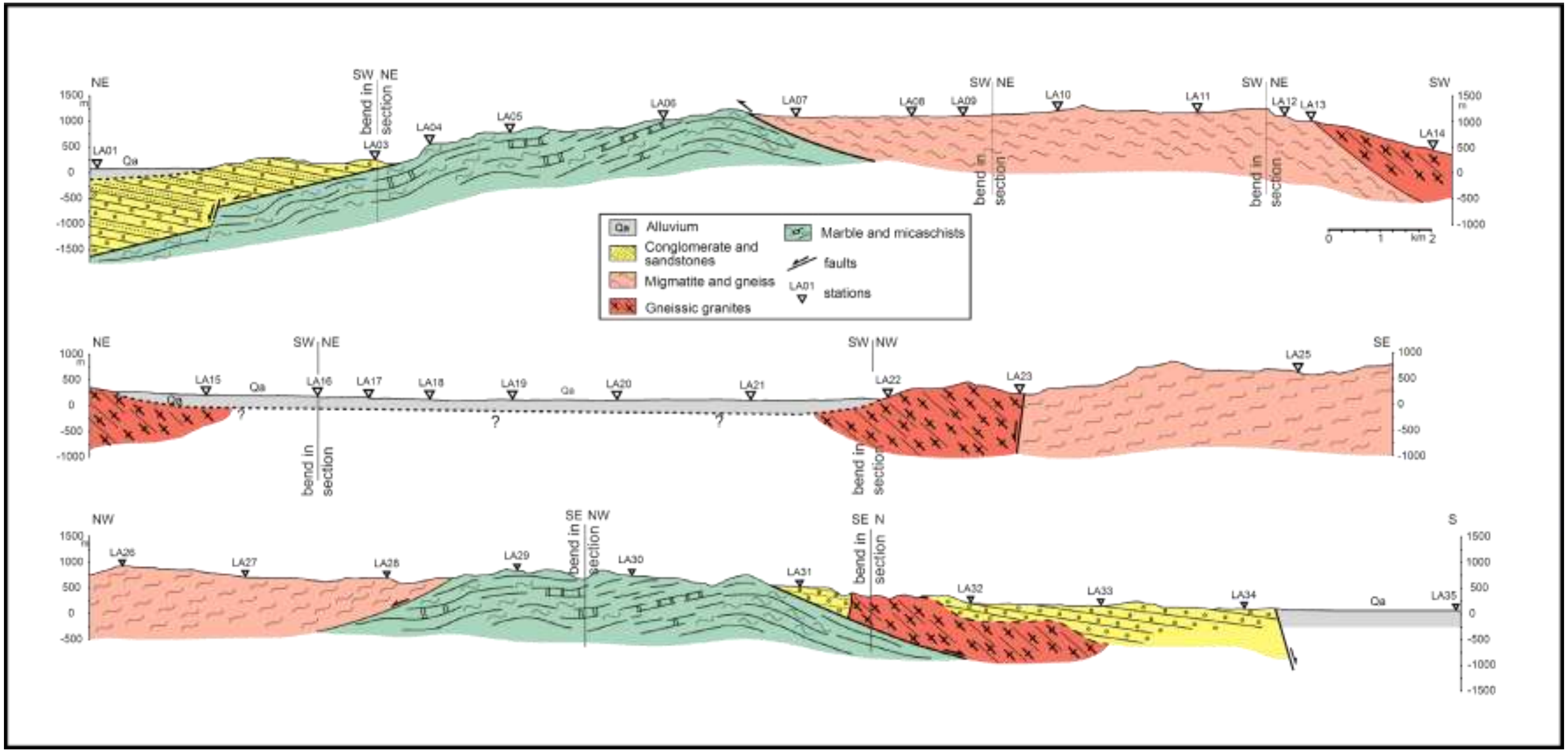

Figure 3.2 Geological cross-section along the linear array.

Table 3.1 The list of codes, coordinates, geologic formation and number of data for each station used in this study.* represents broadband stations (after Akyol et al., 2013).

Station Number	***Station Code***	***Latitude (N)***	***Longitude (E)***	***Elevation (m)***	***Site Formation***	***Number of data***
1	LA01	38.4987	28.1135	130	Alluvium	44
3	LA03(39)	38.4497	28.1136	309	Neogene conglomerate	70
4	LA04	38.4428	28.0915	654	Neogene conglomerate	45
5	LA05	38.4288	28.0903	802	Micaschist	17
6	LA06	38.4036	28.0804	1043	Micaschist	28
7	LA07	38.3805	28.0793	1093	Micaschist	119
8	LA08	38.3650	28.0807	1147	Agricultural soil on top of the micaschist	6
12	LA12	38.3022	28.0347	1219	Micaschist	6
13	LA13	38.2956	28.0213	989	Micaschist	96
15	LA15(40)	38.2593	27.9947	244	Micaschist	49
16	LA16	38.2391	27.9835	186	Alluvium & Micaschist	55
20	LA20	38.1841	27.9687	129	Micaschist	150
21	LA21	38.1619	27.9573	127	Micaschist	13
22	LA22	38.1404	27.9582	169	Gneissic granite	82
23	LA23	38.1196	27.9748	231	Gneissic granite	10
24	LA25	38.0710	27.9784	564	Micaschist	5
25	LA26	38.0495	27.9891	985	Micaschist	125
27	LA27	38.0301	27.9929	753	Micaschist	14
32	LA32	37.9148	28.0514	280	Sandstone	12
33	LA33	37.8937	28.0439	226	Sandstone	44
34	LA34	37.8692	28.0524	142	Sandstone & Conglomerate	41
35	LA35	37.8444	28.0509	102	Alluvium	12
41	LA41	38.2128	28.0699	238	Mylonitic granites with gneissic foliation	12
42	AKH*	38.9149	27.8081	128	Alluvium	77
43	AYD*	37.8407	27.8374	86	Alluvium	58
44	BOZ*	38.3002	28.0495	1216	Agricultural soil on top of the micaschist	244
45	DEU*	38.3710	27.2078	248	Limestone	145
46	KUL*	38.5401	28.6339	700	Agricultural soil on top of the micaschist	40
47	MAN	38.5931	27.5184	88	Alluvium & colluvium	149
48	NAZ	37.9134	28.3432	119	Alluvium	15
49	SAR	38.2345	28.6859	279	Sandstone	156
50	SEL	37.9443	27.3677	49	Alluvium	46

3.2 Data and Initial Processing

Initial data processing was done by Lupei Zhu, Nihal Akyol and Sebastiano D'Amico. In this study, pseudo accelerations generated from velocity recordings were analysed. First of all, high quality of data was rotated to transverse and radial ones and picking of first P- and S-arrivals was done visually by Nihal Akyol and Murat Çamyıldız. Examples of transverse component recordings from Buldan earthquake (M=5.2, 23.07.2003) are shown in Fig. 3.3. Because of the noise levels for some array stations in the grabens leading to poor signal-to-noise levels (significantly higher than for those on the horsts by a factor of 3 for selected S-wave window), the remaining 436 events with 1985 three component records were evaluated. Figure 3.4 shows the locations of the stations and distribution of earthquakes used in HVSR and SSR applications. The dataset includes events with local magnitudes ranging from 2.0 to 5.6, with hypocentral distance ranges between 6 and 294 km and focal depths from 1.4 to 30 km (Fig. 3.5).

For each component, the Fourier Transform of the shear-wave group of arrivals was computed after applying a 5% cosine tapered window. That taper was applied before the S-wave arrival to ensure that the selected window for spectral analysis did not disturb the beginning of the S-wave. The spectra were then smoothed with a 9-point moving average operator that corresponds to a rectangle function of 0.625 Hz width. Figure 3.6 represents three-component raw acceleration and smoothed spectra of time histories of Buldan earthquake in Fig. 3.3. In order to see the smoothing effects of different filter widths on the results, 5, 7 and 11-point moving averages were also applied to the spectra. Figure 3.7 depicts the effect of 4 different smoothing filter widths on HVSR results. For the determination of time windows, the effects of 3, 5, 7 and 9 sec window lengths on the results in terms of HVSR were also compared in a common frequency interval (Fig. 3.8). The time window starting with S-wave arrival was selected as 7 sec.

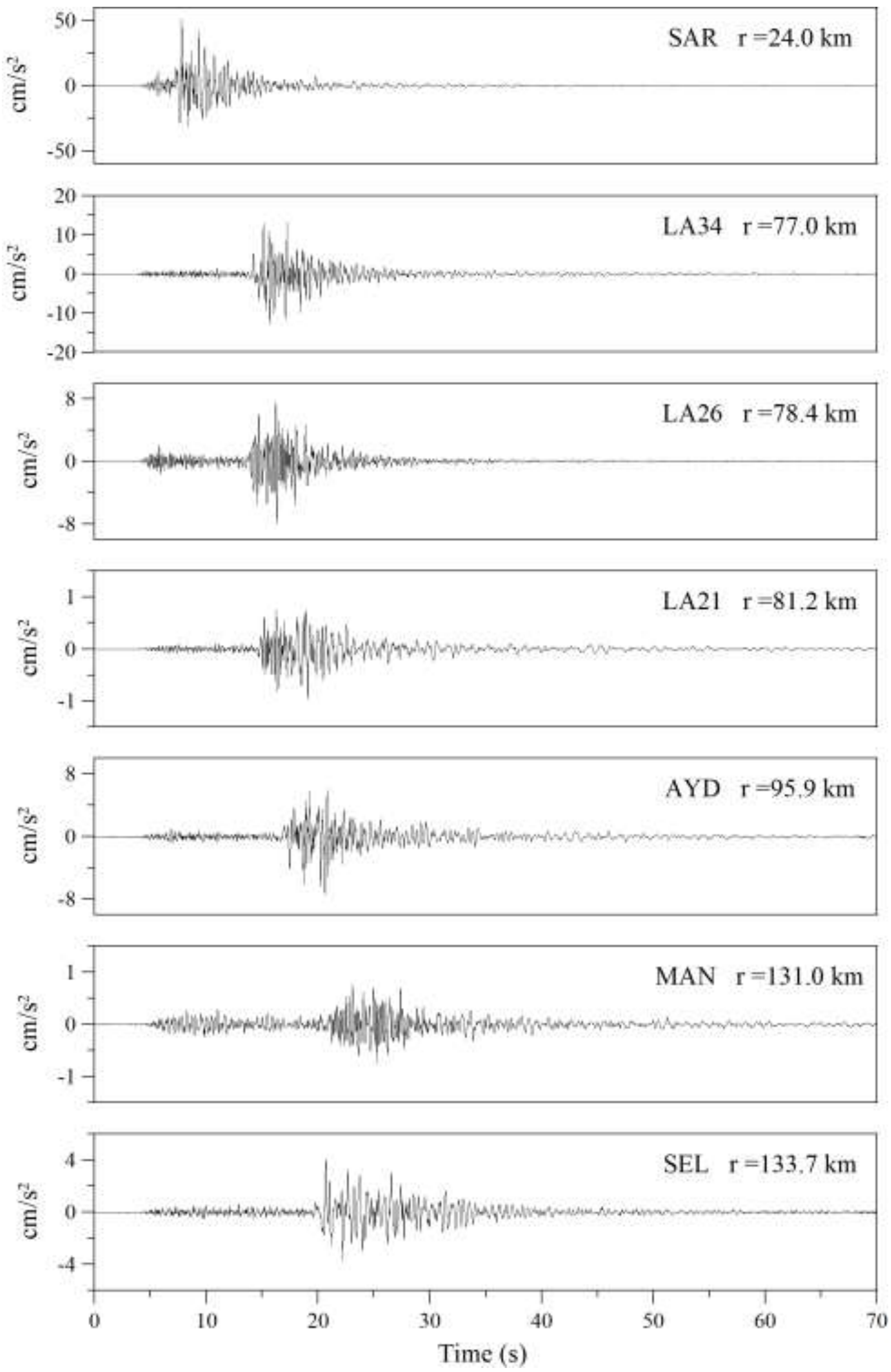

Figure 3.3 Examples of transverse component recordings from Buldan earthquake (M=5.2, 23.07.2003). The origin of the time axis has been adjusted for displaying purposes and it does not correspond to the origin time of the respective event. *r* represents hypocentral distances of this event at selected stations.

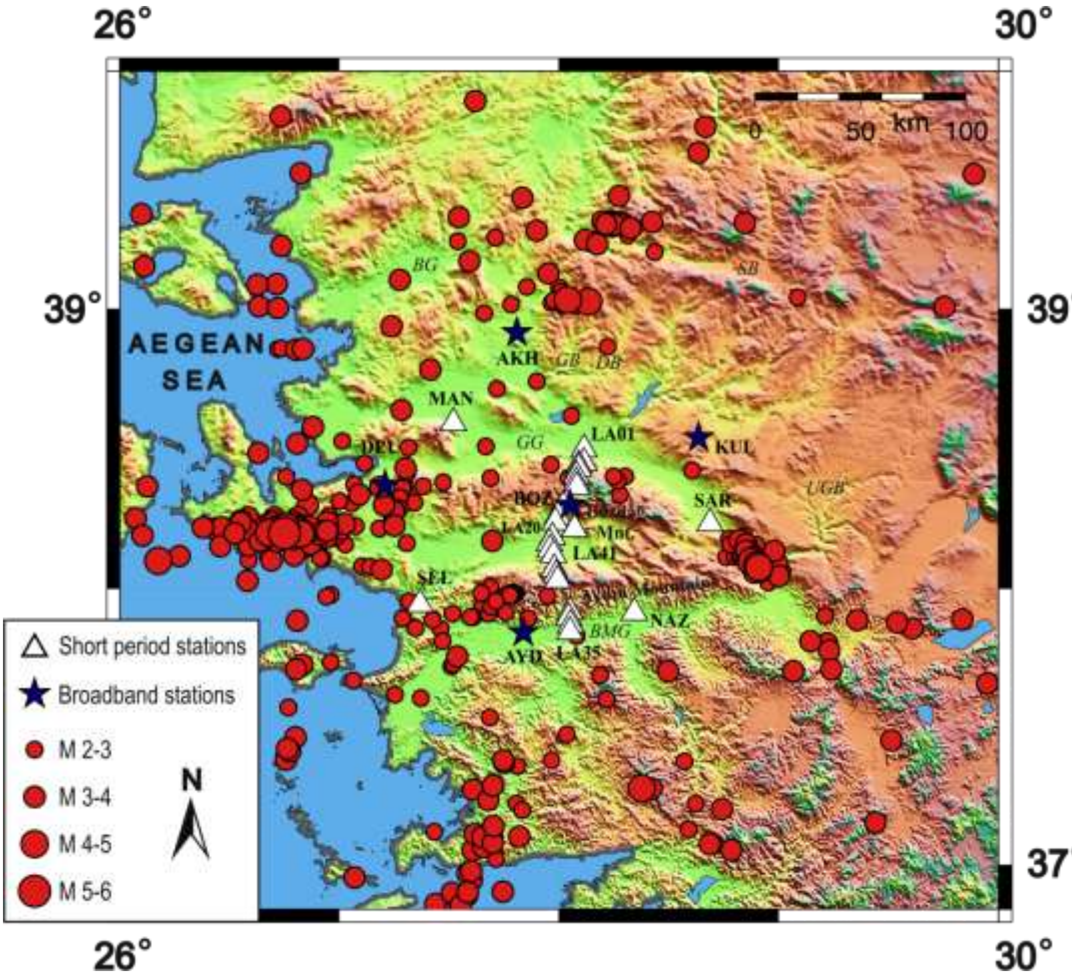

Figure 3.4 Regional map showing location of the stations and distribution of earthquakes (red dots) used in this study. White triangles and blue stars indicate short period and broadband stations of WASRE network, respectively. GG: Gediz graben, KMG: Küçük Menderes graben, BMG: Büyük Menderes graben.

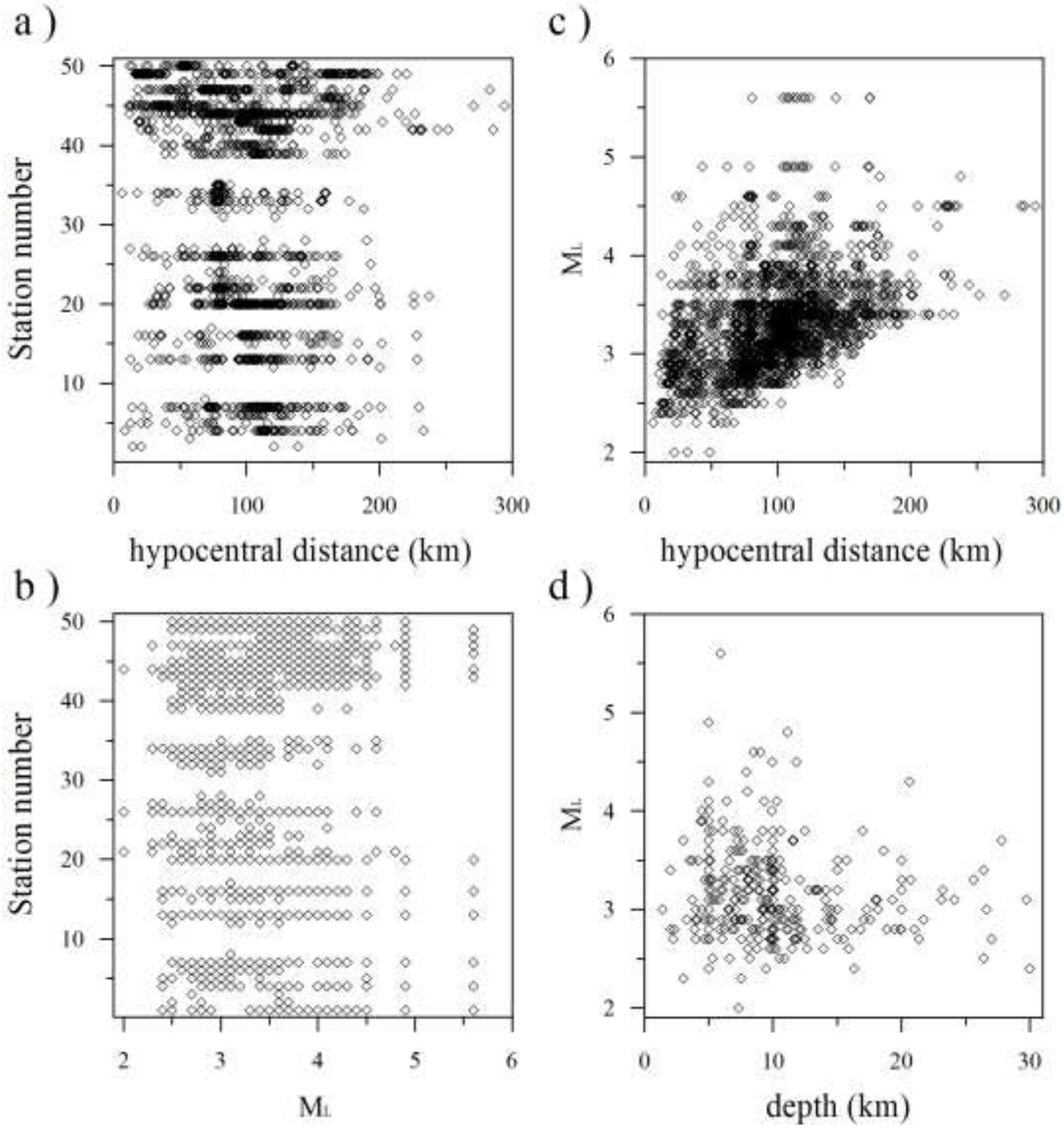

Figure 3.5 Distributions of dataset: (a) and (b) depict station numbers versus hypocentral distances and local magnitudes, whereas (c) and (d) represent local magnitudes versus hypocentral distances and depths of earthquakes, respectively.

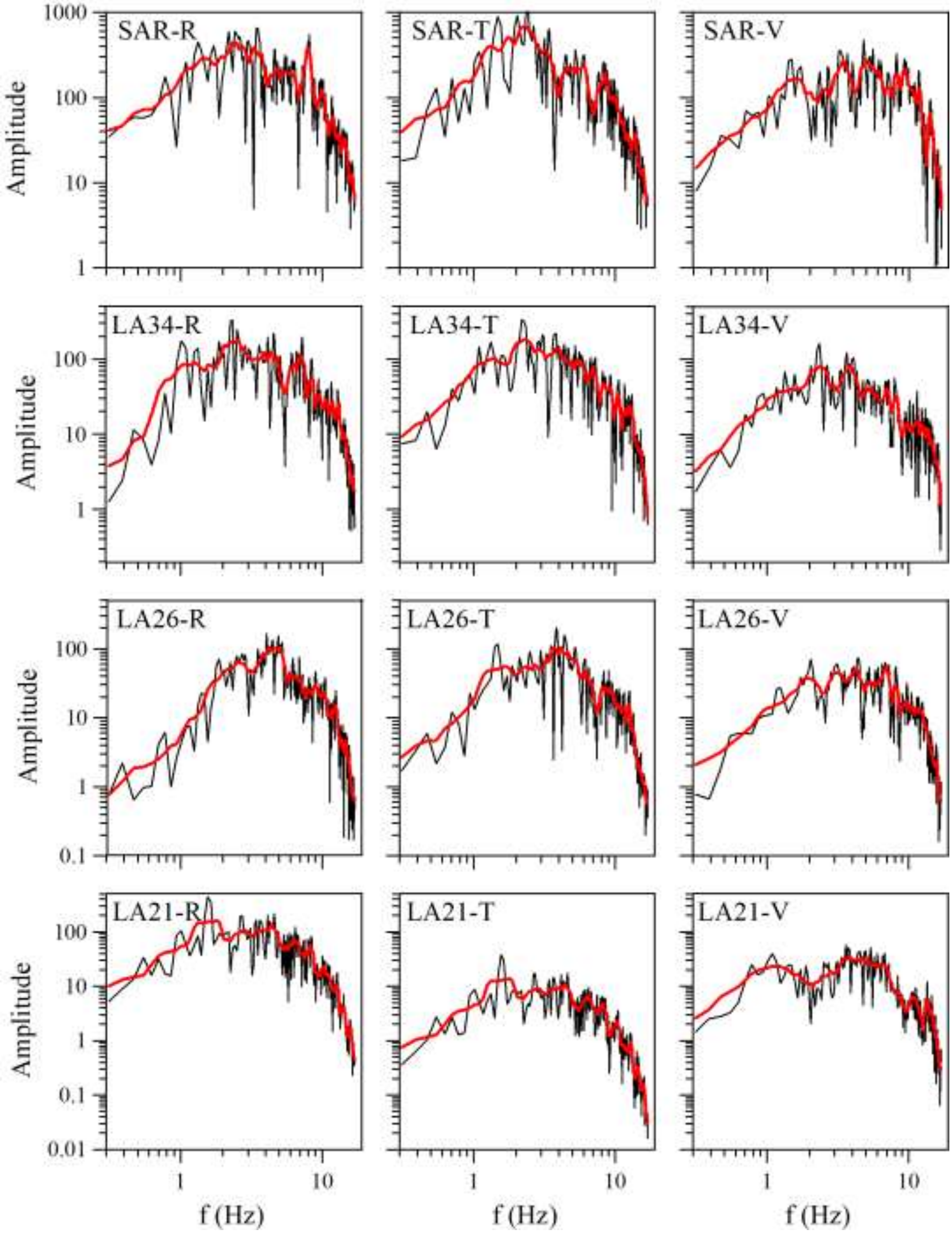

Figure 3.6 Three component raw acceleration spectra (black lines) and smoothed spectra (red lines) from Buldan Earthquake (M=5.2, 23.07.2003). The spectra were smoothed with a 9-point moving average operator.

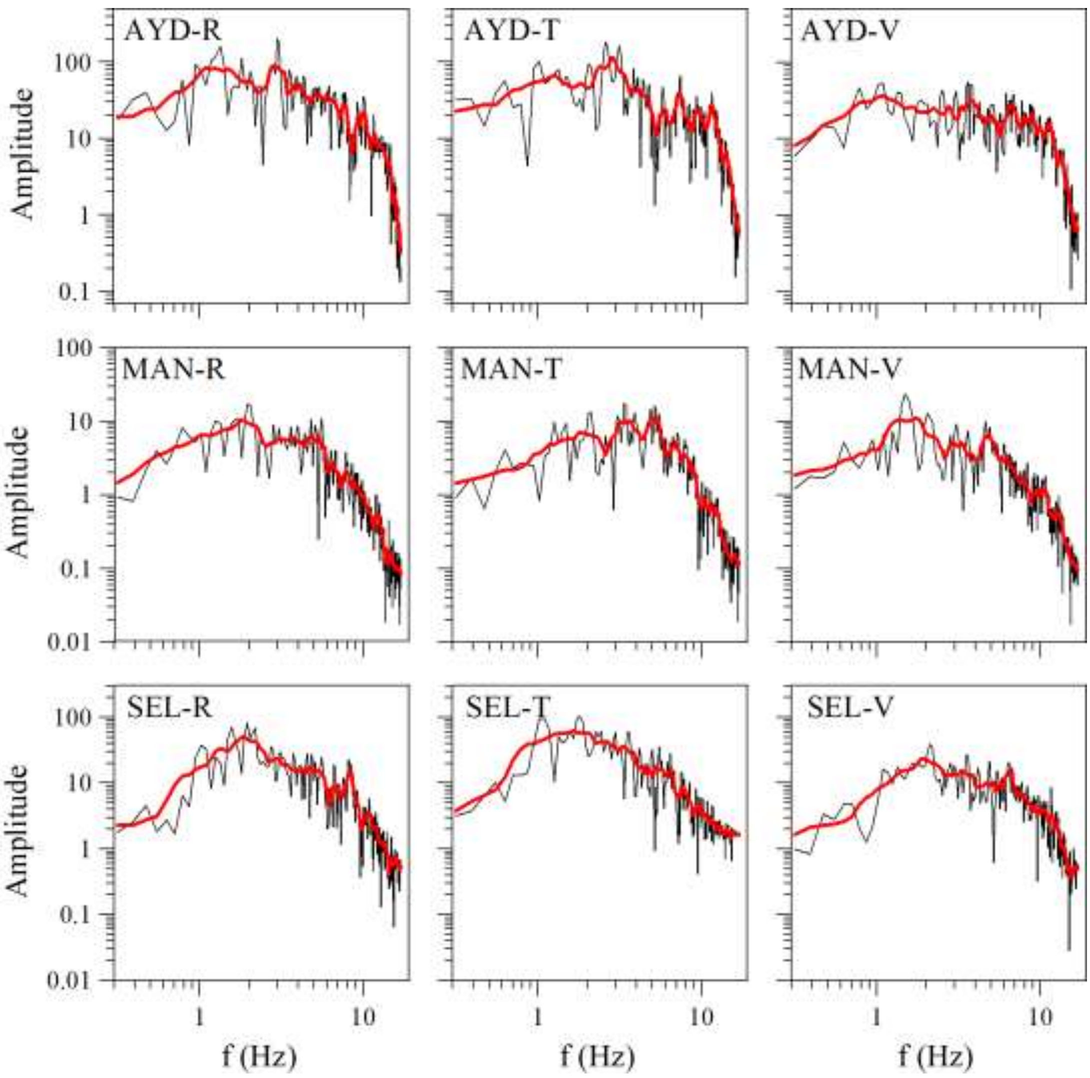

Figure 3.6 Three component raw acceleration spectra (black lines) and smoothed spectra (red lines) from Buldan Earthquake (M=5.2, 23.07.2003). The spectra were smoothed with a 9-point moving average operator (continued).

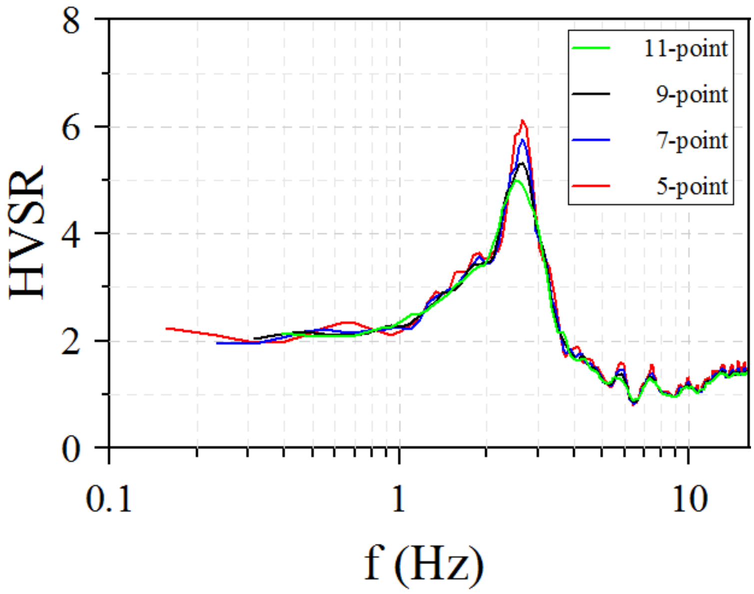

Figure 3.7 Effects of 4 different smoothing filter widths (5, 7, 9 and 11-point moving averages) on T-component HVSR results.

After spectral ratio estimates, a non-parametric inversion scheme described by Castro et al. (1990) was applied to the data to separate source, site and propagation characteristics. To improve the resolution of inversion processes, the data were restricted to the stations having at least ten records and to the earthquakes recorded by at least three stations during this stage. Thus, the remaining 322 events with 1764 three-component recordings were evaluated. The detailed information about the data used in inversion steps are given in the Chapter 5.

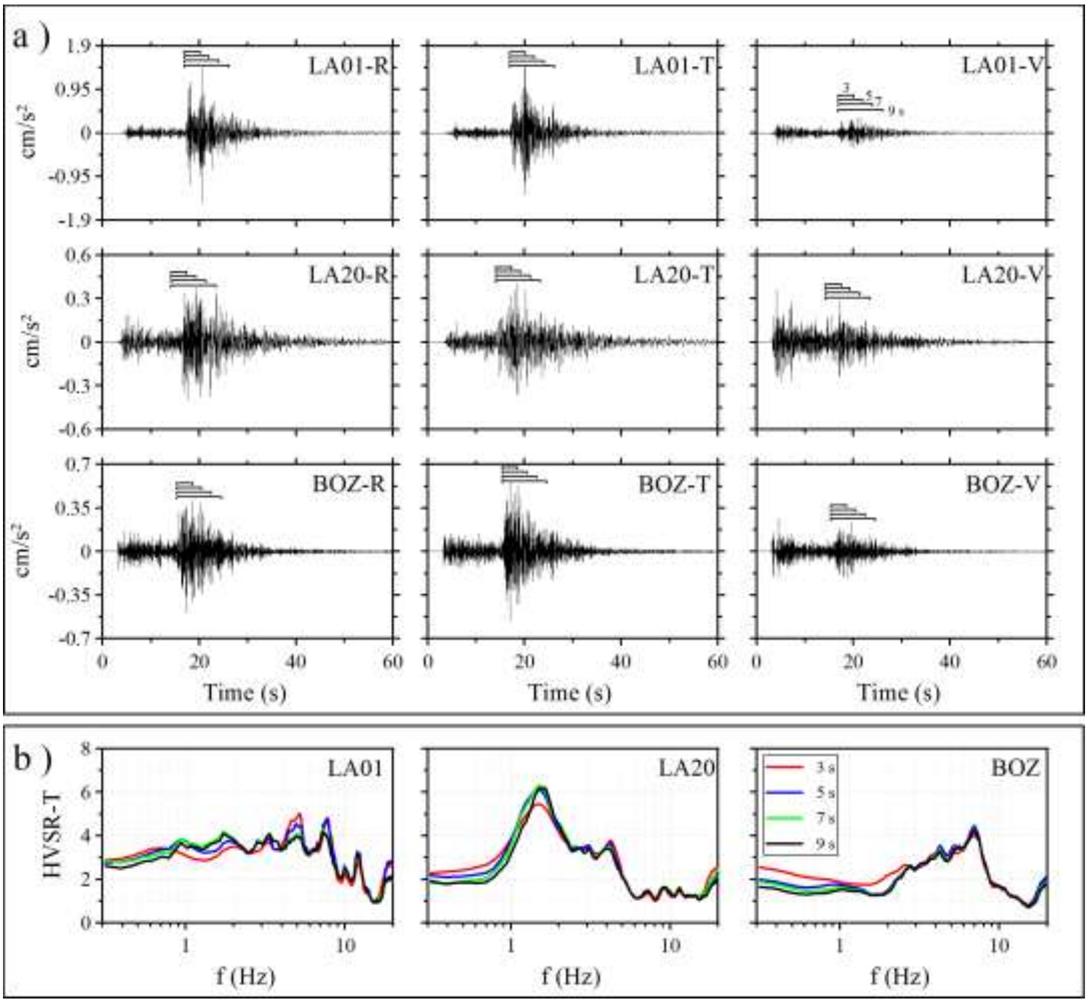

Figure 3.8 a) Examples of recordings (R: radial; T: transverse; V: vertical components) at three of the analyzed stations for an earthquake ($M_L = 4.1$) and b) the effects of 4 different window lengths (3, 5, 7 and 9 sec) on T-component HVSR results.

CHAPTER FOUR
AMPLIFICATION ESTIMATIONS FROM SPECTRAL RATIO TECHNIQUES

4.1 Overview

Perspective of seismology, ground motion is essentially caused by the movement of the earth's surface from earthquakes. It is produced by seismic waves that are generated by sudden rupture of a fault and travel through the earth and along its surface. Kramer (1996) describes *strong ground motion* as “the motion of sufficient strength to affect people and their environment”. Indeed earth continuously shakes; the great majorities of these motions are insensible and can be only detected by specialized precision instruments. This type of ground motion is referred to as *weak ground motion*. Strong ground motion studies have great importance for seismic hazard studies in the sense of earthquake engineering. The following questions can be enhanced to better understand and quantify the most important characteristics of strong ground motions: *“Which factors control the level of ground shaking?”*, *“What are the measures of ground motion?”*, “*Why the ground motion varies from a site to another?”* and *“What are the site effects?”* etc. All of the answers are directly related with frequency contents of the ground motion. The frequency content of the motion is mainly controlled by source, path and site effects. Note that source and path effects are beyond the scope of this chapter.

The uppermost geological layers modify the characteristics of the incoming seismic wave, resulting in an amplification or deamplification. Variability in ground motions generated by an earthquake at a particular site is mainly controlled by its near surface geology (Steidl et al., 1996). This effect of the local geology on the seismic wave is called *site effect* and generally seen as site amplification. Increment in the amplitudes of seismic waves is primarily caused by the seismic impedance contrast between the soil layer and the bedrock in the case of 1D ground model. Soil layers near the surface have low impedance (Şafak, 2001). Large impedance contrast between sediment-bedrock interface and basin geometry cause the trapping and focusing of body wave energy within the soil volume in the sediment-filled basins. Constructive interfering of these trapped waves (multiple reflections of body waves) may result in resonance at the fundamental frequency of the soft soil layers (Bindi et al., 2011). This is termed as *deep basin effect*. If low-velocity layers are present near the surface, the reflected waves can be trapped near the surface and start propagating as surface waves. Basin-induced surface waves that propagate back and forth as energy trapped within the near surface of sediments are the main sources of 2D or 3D site effects. These body-to-surface wave conversions occur at the edges of the basin, where the soils are laterally bounded by strong geological discontinuities such as rock and faults (Bindi et al., 2009).

Earthquake recordings provide experimental estimation of the site transfer function. On the other hand, alternative methods based on ambient noise recordings have developed in urbanized or low to moderate seismic areas over the last decades (Bonnefoy-Claudet et al., 2006). Site effects from recorded motions can be estimated by using of theoretical or experimental approaches (Parolai et al., 2004). The theoretical calculations of the site response can be performed by analytical analyses and numerical simulations when the geological structure and the geotechnical characteristics of the site are well known. The basic and initial approach is 1D analysis of soil columns. But accurate solutions require the knowledge of the geometry and thickness of all soil layers from surface to bedrock and their dynamic properties (e.g., density, velocity, near-surface attenuation). Many of the above mentioned parameters may be obtained through in-situ geophysical and geotechnical surveys. On the other hand, the development of computer technology has provided to obtain more realistic site effects simulations based on 2D or 3D wave propagation including the basic physical concepts and definitions of ground motions such as take-off angle, azimuth, near-fault rupture directivity, attenuation, diffraction, resonance, scattering, soil nonlinearity and topography, etc. (Bonilla et al., 2005; Field, 1996; Gao et al., 1996).

Site effects from recorded motions due to earthquakes or microtremors can be directly estimated by using experimental approaches. These methods, which are commonly used for microzonation studies, are mainly used for characterization of site function and fundamental frequency of the soil profile and do not require any prior knowledge of geology. The experimental methods can be divided in different groups as spectral ratio and separation (inversion) approaches as well as reference and non-reference techniques (Parolai et al., 2004). The reference site spectral ratio approach involves taking the ratio of the Fourier amplitude spectrum of the soil site recording to that of the rock-site recording (Borcherdt, 1970). The rock-site is regarded as free of site effect. This approach is referred to as 'the Standard Spectral Ratio-(SSR)' or 'the Reference Site Method-(RSM)'. Apart from this method, other spectral ratio techniques such as cross-spectral ratios (e.g., Steidl, 1993), response spectral ratios (e.g., Kitagawa et al., 1992) and ratios of peak, RMS or effective accelerations (e.g., Borcherdt & Wentworth, 1995) have also been used (Şafak, 1997). The main limitation of SSR approach is lack of appropriate reference site station. Alternatively, another spectral ratio method has become popular. It is commonly known as 'Nakamura Method' or 'Horizontal-to-Vertical Spectral Ratio-(HVSR)'. The method determines site function as the horizontal-to-vertical spectral ratio of recordings at a single station without any reference site station. This is widely used to estimate site transfer function from ambient noise even if in the areas have moderate to low seismic activity. Another method commonly applied to estimate site function is the separation of site, source and path effects. It is usually performed utilizing the generalized inversion technique (GIT) (e.g., Andrews, 1986; Boatwright et al., 1991; Castro et al., 1990; Hartzell, 1992; Oth et al., 2011; Parolai et al., 2004). It allows obtaining source, path and site effects, separately and/or simultaneously, from many observed data recorded by a regional seismic network.

SSR method is widely used to estimate site effects when the reference site station is available. Briefly, this technique involves spectral ratio of the same component of the ground motion recorded at two nearby stations. One of the stations, which will be used as the reference site station, has to be placed on an outcropping hard rock. The main assumptions of the method are: 1) two stations have the same source and propagation effects. Therefore, the stations having the same source records should be located closely; and 2) the reference site has no site complexity of its own. The technique has been introduced by Borcherdt (1970) to demonstrate local site effects at San Francisco Bay, California. He used five nuclear explosions in Nevada as recorded at 37 locations and five strong-motion recordings of the San Francisco earthquake (M=5.3) of March 22, 1957. He obtained consistent results related to the geologic setting of the recording sites. The results showed that spectral amplification curves have clear peak for younger bay mud sites whereas there is not any identical site resonance period for older, more consolidated sediments. Borcherdt & Gibbs (1976) expanded this work by adding explosions data from new stations. They confirmed earlier conclusions and also provided the estimates of site response of additional geological units. Rogers et al. (1984) made similar studies for the Los Angeles region using an extensive strong-motion dataset from 1971 San Fernando Earthquake and 159 three-component recordings of Nevada nuclear tests. Although there are minor discrepancies between the spectral ratios for the recordings of the earthquake and nuclear tests due to the differences in strain levels, propagation paths and azimuths of two sources; they concluded that the site effects derived from the two source types are statistically equivalent.

In fact, the source term is not the same for the reference site and the site of interest because of radiation and directivity effects. However, these effects are expected to be averaged out by using a large number of events (Bindi et al., 2009) with good azimuthal distribution. It is not always possible to find appropriate reference site allowing the assumption that similarity in the wave paths towards these two stations due to the distance between the stations is not smaller than their hypocentral distances. Another crucial point of this technique is the assumption that the hard rock site at the surface acts as like the bedrock below the soil layers. The assumption is that hard rock site is transparent towards the input motion comes from base of a soil column and has no site complexity of its own (Hartzell, 1992). It is not always valid due to the rock stations may have their own response; however, this 1D assumption can be acceptable for practical reasons. Recently, some of studies on reference sites in the literature show that they got some deviations from this matter (e.g., Bindi et al., 2009; Bonilla et al., 1997; Parolai et al., 2004) and ideal reference sites would require uniform, perfectly elastic half-spaces (Malagnini et al., 2004). Malagnini et al. (2004) suggested that site functions obtained by the SSR method can be misleading in inferring true site transfer functions especially for high frequencies, since most of the reference site transfer functions showed large variability at high frequencies. As being another caution, SSR approach expires in the case of basin and valley areas dominated by basin-edge-induced waves and could underestimate the absolute amplification levels (e.g., Bindi et al., 2009; Field, 1996; Lachet et al., 1996).

As an alternative to SSR, non-reference methods have emerged and are widely used in the absence of appropriate reference site station. Thus, researchers have had the opportunity to test different methods with the emergence of alternative methods. Since then, many studies have been carried out (e.g., Akyol et al., 2002b, 2013; Bindi et al., 2011; Bonilla et al., 1997; Field & Jacob, 1995; Parolai et al., 2000; Riepl et al., 1998; Triantafyllidis et al., 1999). HVSR method involves comparison of the spectral ratio between horizontal and vertical components of the ground motion at the same site. It is assumed that these components contain the same source and propagation effects and the vertical component of motion at a site of interest is not influenced by any local site conditions in the case of 1D soil column model. So, the method hypothesized that the spectral ratio will only give the amplified frequency peaks due to site resonance (Lermo & Chavez-Garcia, 1993). The main advantage of this method is that it is not required reference site station. Also, the HVSR method is more rapid, cost effective and efficient (Goetz, 2009). To estimate the site effects, firstly, Nogoshi & Igarashi (1970) introduced this technique; however, Nakamura (1989) made it popular. Then, Lermo & Chavez-Garcia (1993) applied the approach to data from three different cities in Mexico. They concluded that their site function estimates using both HVSR and SSR methods consistent and the HVSR method can obtain the dominant frequency of the site. They also used numerical modeling of SV-waves and obtained that the HVSR can give a robust estimate for the first resonant mode, but not for higher modes. After then, many studies utilizing the method have been carried out using different earthquake datasets (e.g., Akyol et al., 2002b, 2013; Oth et al., 2009; Riepl et al., 1998; Sokolov et al., 2005; Theodulidis & Bard, 1995).

Although there is a disagreement among the researchers related to the nature of ambient seismic noise and the amount of which types of waves included in microtremor, the HVSR technique has also become a standard tool to estimate site effects from ambient noise due to its simplicity, practicality and low costs in urbanized areas where space is limited and large arrays cannot be placed. It is known that microtremors consist of both body and surface waves. Nakamura (1989, 2000) claims that the source of ambient noise is multiply refracted vertical incident SH waves and the fundamental resonance frequency of soft near-surface layer could be obtained by HVSR of microtremor data. According to him, the vertical component of ambient noise keeps the characteristics of source to sediments surface ground. It also relatively includes the effects of Rayleigh waves on the sediments. Thus, it can be used to remove both of the source and the surface wave effects from the horizontal components (Nakamura, 2000). On the contrary, some of researchers suggest that microtremors are composed of Rayleigh waves which propagate in a surface layer over a half-space (e.g., Bonnefoy-Claudet et al., 2006; Dravinski et al., 1996; Lermo & Chavez-Garcia, 1994; Lunedei & Albarello, 2009). Lermo & Chavez-Garcia (1994) proposed that the Nakamura’s assumptions are result of Rayleigh wave propagation. Parolai et al. (2004) suggested that the fundamental resonance frequency of the site can be reliably estimated by HVSR of noise recordings.

Many comparison efforts with other techniques, utilizing some theoretical and numerical studies, have started in order to better understand the capability and/or drawbacks of the HVSR method. Several studies indicate that the fundamental resonance frequency of a site can be estimated by the method (e.g., Bindi et al., 2011; Bonilla et al., 1997; Parolai et al., 2000). Huang & Teng (1999) also concluded that the amplification level of a site response can be estimated by HVSR especially for sites in the vicinity of the epicenters. Nonetheless, HVSR generally shows different amplification levels than SSR and GIT estimates: These differences are caused by both the influence of the incidence angle and converted waves at the sediment-bedrock interface (Parolai et al., 2004). Parolai & Richwalski (2004) showed these differences by utilizing numerical simulations. They obtained that deamplification in the HVSR at frequencies higher than the fundamental one is due to *S*-to-*P* conversion leads to amplification of the vertical component in the *S*-wave window. However, HVSR has widely used in the evaluation of site amplification in deep sedimentary basin structures (e.g., Bindi et al., 2009, 2011) and it is suggested as successful technique to identify the fundamental resonant frequency and can be used to infer the 1D resonant frequency of the sites.

4.2 HVSR Method and Results

The observed waveform in the time domain $u(t)$ can be modeled as a convolution of the source, $s(t)$; propagation path effect, $p(t)$; and site amplification effect, $z(t)$ assuming linear systems:

$$u(t) = s(t) * p(t) * z(t) \tag{4.1}$$

The observed amplitude spectrum is expressed as a product of these effects in the frequency domain:

$$U(f) = S(f)P(f)Z(f) \tag{4.2}$$

where $U(f)$, $S(f)$, $P(f)$ and $Z(f)$ are the Fourier transform of the $u(t)$, $s(t)$, $p(t)$ and $z(t)$ functions, respectively. If we consider a half-space with a horizontal sedimentary layer on top, site effect occurs due to this soft low-velocity soil layer. The ground amplification will be given by the transfer function in the frequency domain:

$$T(f) = \left(t_v(f)^2 + t_h(f)^2\right)^{1/2} \tag{4.3}$$

where $t_v(f)$ and $t_h(f)$ are the vertical and horizontal components of $T(f)$, respectively. To establish empirical transfer functions t_h and t_v on the basis of the horizontal and vertical earthquake measurements on soil surface and at bedrock level, $t_v(f)$ and $t_h(f)$ can be expressed by using following equations:

$$t_v(f) = \frac{U_{vs}(f)}{U_{vb}(f)} = \frac{S_v(f)P(f)Z_{vs}(f)}{S_v(f)P(f)Z_{vb}(f)} \tag{4.4}$$

where U_{vs} is amplitude spectrum of the vertical component of motion at the surface and U_{vb} is amplitude spectrum of the vertical component of motion at the base of sediments. $S_v(f)$ and $P(f)$ contain the contribution of source and path effects. $Z_{vs}(f)$ and $Z_{vb}(f)$ indicate the site amplifications induced by the sediments and bedrock of the vertical component. Similarly for the horizontal component of transfer function:

$$t_h(f) = \frac{U_{hs}(f)}{U_{hb}(f)} = \frac{S_h(f)P(f)Z_{hs}(f)}{S_h(f)P(f)Z_{hb}(f)} \tag{4.5}$$

where U_{hs} is amplitude spectrum of the horizontal component of motion at the surface and U_{hb} is amplitude spectrum of the horizontal component of motion at the half-space. $S_h(f)$ and $P(f)$ contain the contribution of source and path effects. $Z_{hs}(f)$ and $Z_{hb}(f)$ indicate the site amplifications induced by the sediments and the base of sediments of the horizontal component, respectively.

Because of the use of an event recorded by a single station, without a doubt, the source and path effects in the two components can be neglected. Therefore, the HVSR ratio of the transfer function can be written from equations (4.4) and (4.5) as:

$$T_{site} = \frac{t_h(f)}{t_v(f)} = \frac{U_{hs}(f)}{U_{vs}(f)}\frac{U_{vb}(f)}{U_{hb}(f)} = \frac{Z_{hs}(f)\cdot Z_{vb}(f)}{Z_{vs}(f)\cdot Z_{hb}(f)} \tag{4.6}$$

Many borehole observations indicate that the site amplification ratio between the horizontal and vertical components from bedrock is approximately equal to 1 (Nakamura, 1989). If we assume that on the base of the sediments the spectral amplitude of both components is the same ($U_{hb}(f)=U_{vb}(f)$) and due to the assumption that the vertical component of motion does not have any significant amplification, modified site transfer function is the site amplification of horizontal component can be given as following:

$$T_{site} = \frac{U_{hs}(f)}{U_{vs}(f)} = Z_{hs}(f) \tag{4.7}$$

After initial data processing stages mentioned in Chapter 3, HVSR method was applied to ground motion transverse and radial components of 436 earthquakes and for 32 different sites, to highlight site-specific seismic hazard potential of basin/graben structures in the central west Turkey. Here after, HVSR-T and HVSR-R abbreviations will represent HVSR site functions from transversal and radial S-waves, respectively. Figure 4.1 shows the results of HVSR-R estimates for individual events and average values for LA01 and AKH stations. The detailed results of HVSR-T estimates for all individual events together with data distribution for each station were given beforehand by Çamyıldız (2008). Average HVSR-T and HVSR-R estimates for 32 different sites together with 90% confidence levels appear in Fig. 4.2. Estimations of site amplification factors of two components at each site were compared in Fig. 4.3. In general, HVSR-T and HVSR-R estimates are similar within a factor of 2. Beyond the bounds of this factor, clear systematic differences were observed for LA03, LA06, LA13, LA21 and LA35 sites. In the next section, only for LA13 site, this systematical difference could be examined since the number and azimuthal distribution of the data have not been sufficiently abundant for the other sites.

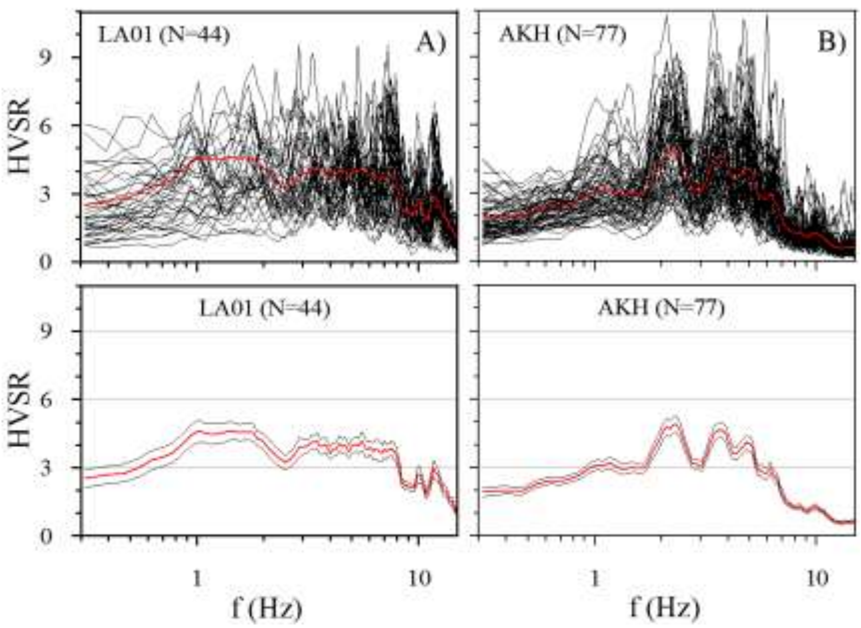

Figure 4.1 Site amplification for all events (black lines) and the average HVSR-R results (red lines) for LA01 and AKH sites with 90% confidence interval from *t*-test. *N* number of data used for these stations.

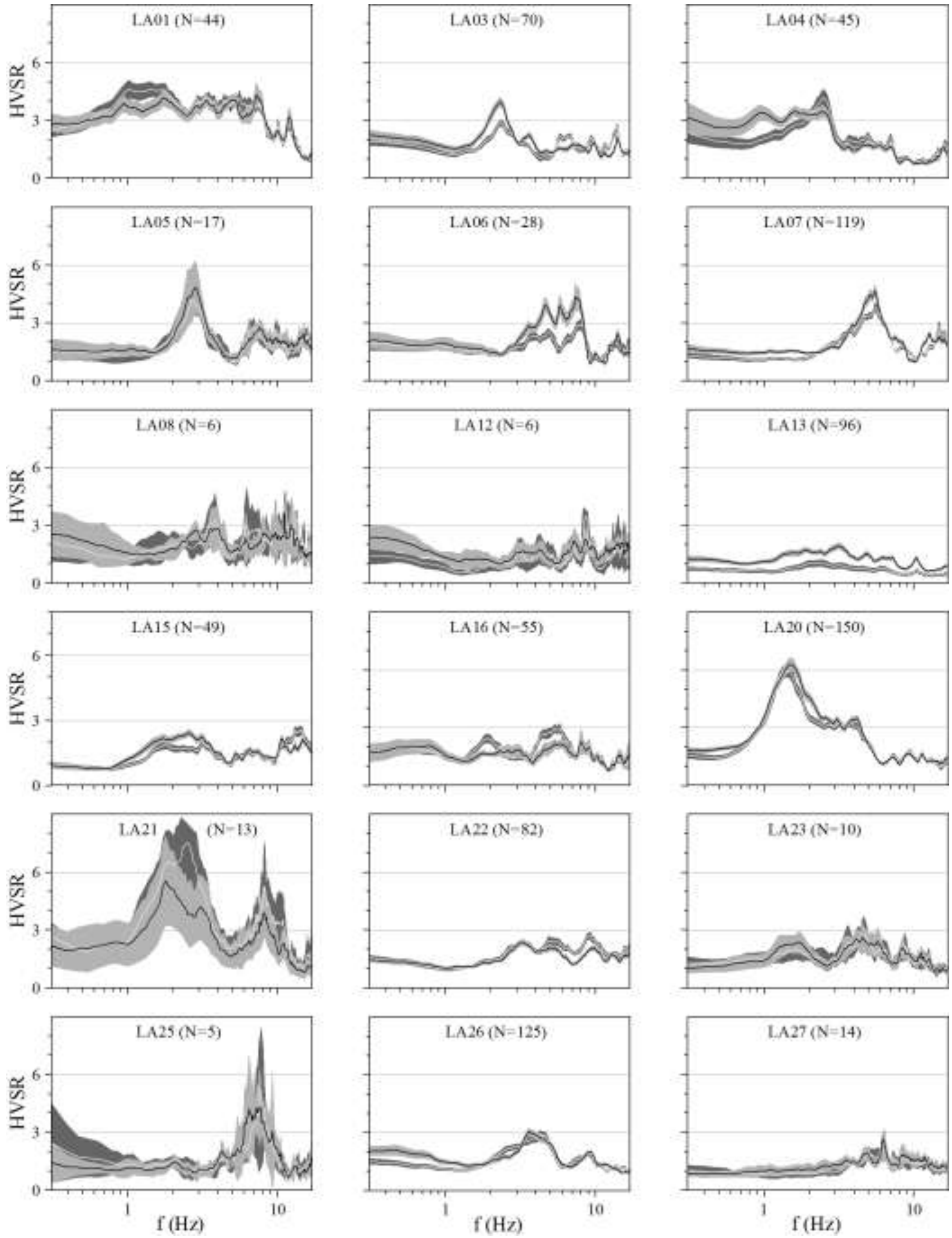

Figure 4.2 The average HVSR results for all sites with 90% confidence interval from *t*-test. Black and white lines represent HVSR-T (Çamyıldız, 2008) and HVSR-R estimates, respectively. *N* number of data used for each station.

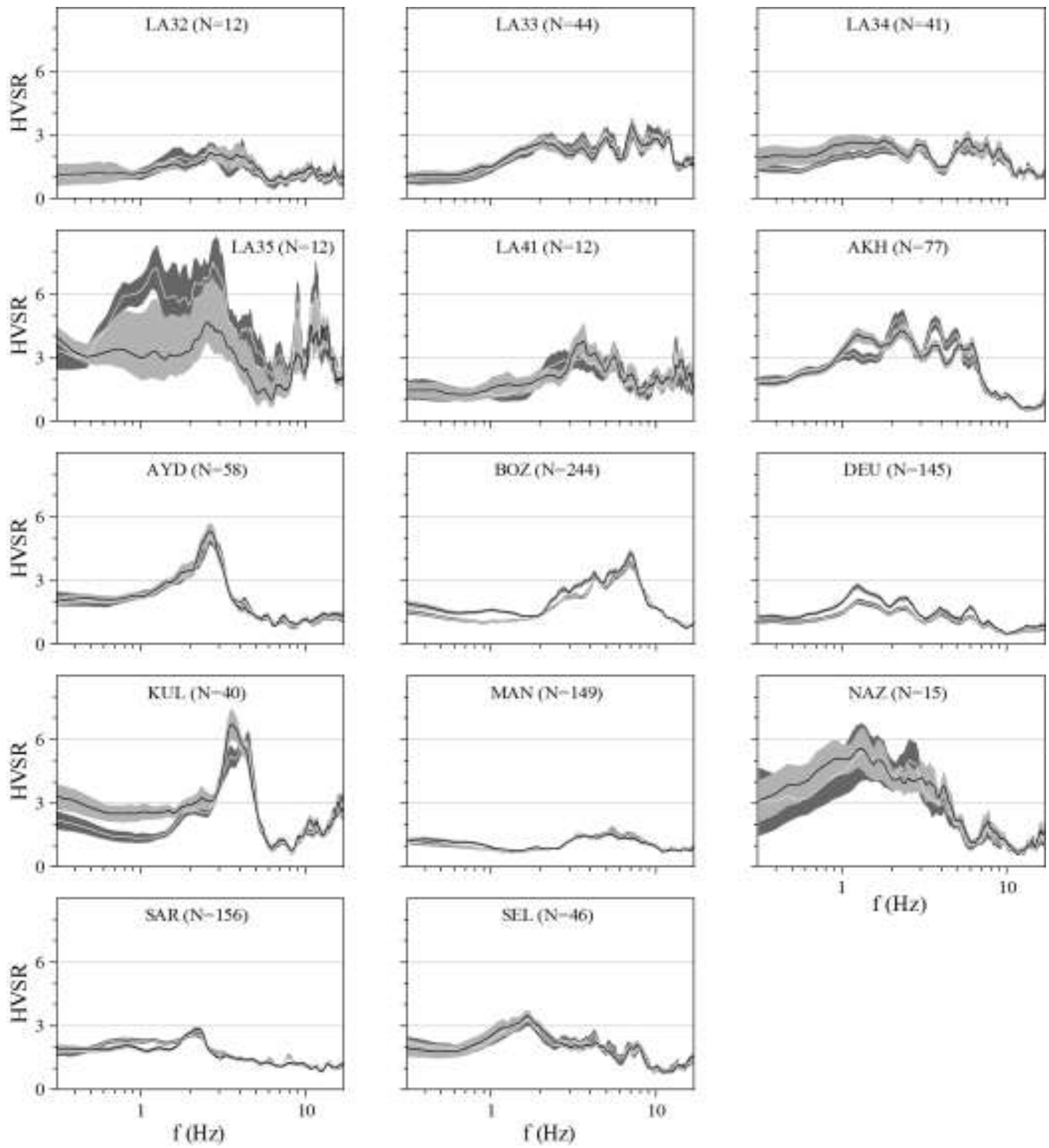

Figure 4.2 The average HVSR results for all sites with 90% confidence interval from *t*-test. Black and white lines represent HVSR-T (Çamyıldız, 2008) and HVSR-R estimates, respectively. *N* number of data used for each station (continued).

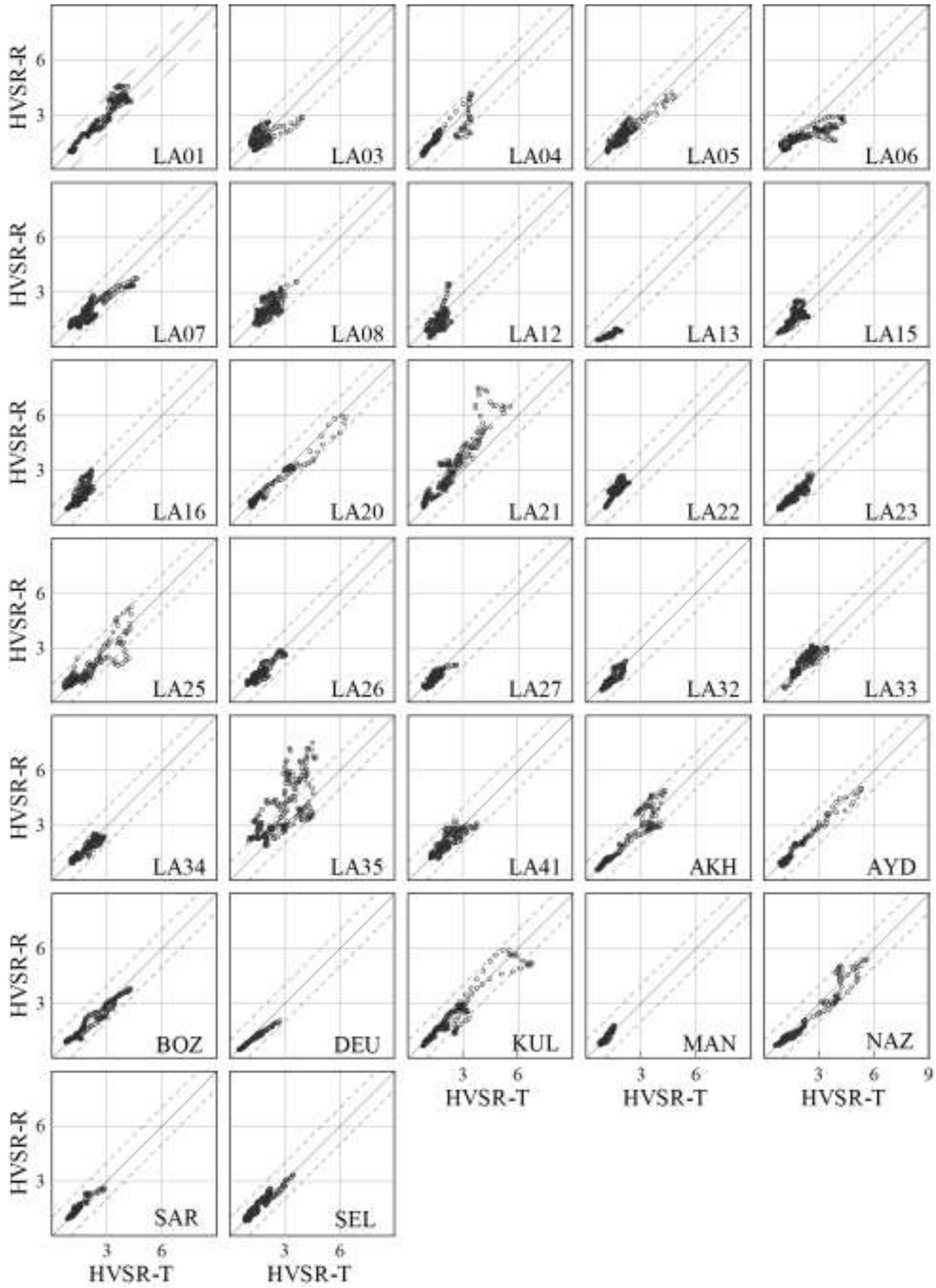

Figure 4.3 Comparison of average HVSR-T (Çamyıldız, 2008) and HVSR-R estimates in whole frequency range interested. The solid line represents the 1:1 correspondence between the two components, and the dashed lines represent a factor of 2 of difference between components. In general, HVSR amplitude values from transverse and radial S-waves are similar within this factor.

4.2.1 Magnitude, Distance and Back-Azimuth Dependencies of HVSR-T Estimates:

HVSR-T results for five linear (LA07, LA13, LA20, LA22, and LA26) and five regional array stations (BOZ, DEU, KUL, MAN and SAR), having good azimuthal distributions, were examined to see distance, magnitude and back-azimuth dependencies of the site functions. For this purpose, epicentral distance values were divided into two groups (DIST1 ≤ 100 km < DIST2). Local magnitude values were divided into three groups ($M_l < 3$; $3 \le M_l < 4$; $4 \le M_l$). Back-azimuth values were divided as four groups (0 ≤ BAZ1 < 90; 90 ≤ BAZ2 < 180; 180 ≤ BAZ3 < 270; 270 ≤ BAZ4 < 360). For each group, scattering of individual results versus the average HVSR-T values for ten sites are given in Fig. 4.4. Observed back-azimuthal scattering of the results are more significant than distance and magnitude dependencies. For that reason, detailed back-azimuth dependencies for these sites were examined as in Fig. 4.5. As being examples, detailed results of two linear array (LA07 and LA13) and two regional (BOZ and DEU) array stations results are given in Fig. 4.6. As shown in these figures, in general, scatterings of back-azimuth groups HVSR values from general average larger than distance and magnitude groups.

Systematical difference between HVSR-T and HVSR-R estimates (Figs 4.2, 4.3 and 4.6) were examined for LA13 site in Fig. 4.7. Firstly, HVSR-T and HVSR-R estimates which obtained by averaging site functions from all individual events were compared in Fig. 4.7a. Clear systematical difference is observed between the results. General average of these HVSR-T and HVSR-R estimates is given as HVSR-1. Secondly, HVSR-T and HVSR-R estimates for the LA13 site give better correlation by averaging of each back-azimuth group and then averaging these four group arithmetic mean values (in Fig. 4.7b). General average of these HVSR-T and HVSR-R estimates is given as HVSR-2. Finally, comparison of these averages, HVSR-1 and HVSR-2, is given in Fig. 4.7c.

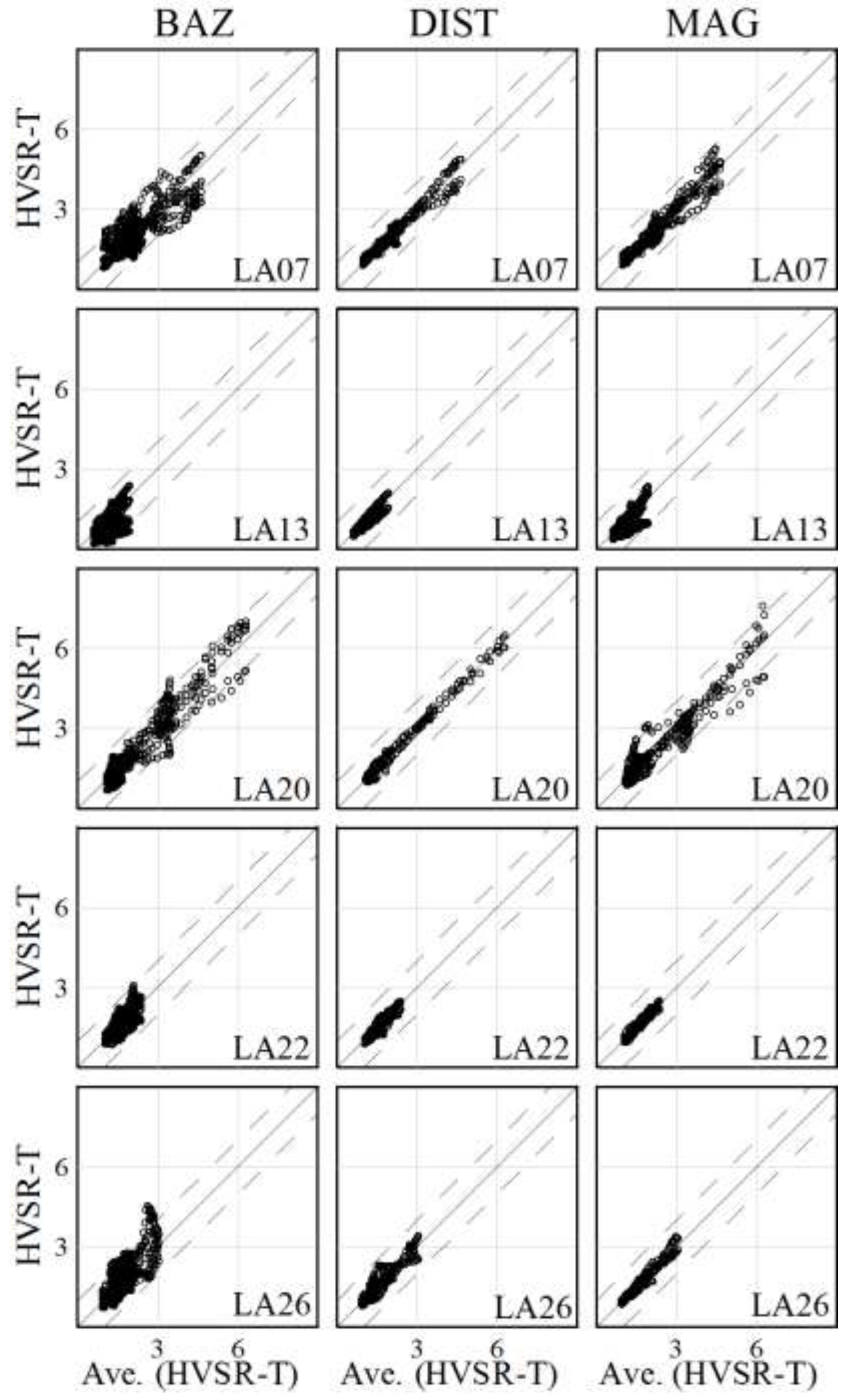

Figure 4.4 Scattering of individual HVSR-T results versus the average HVSR-T values (*Ave*) for the sites. Black solid line (linear fit trough origin) represents correlation between average of all individual event results and average of each subgroup arithmetic mean results for each station. Black dashed lines indicate a linear fit within a factor of 2.

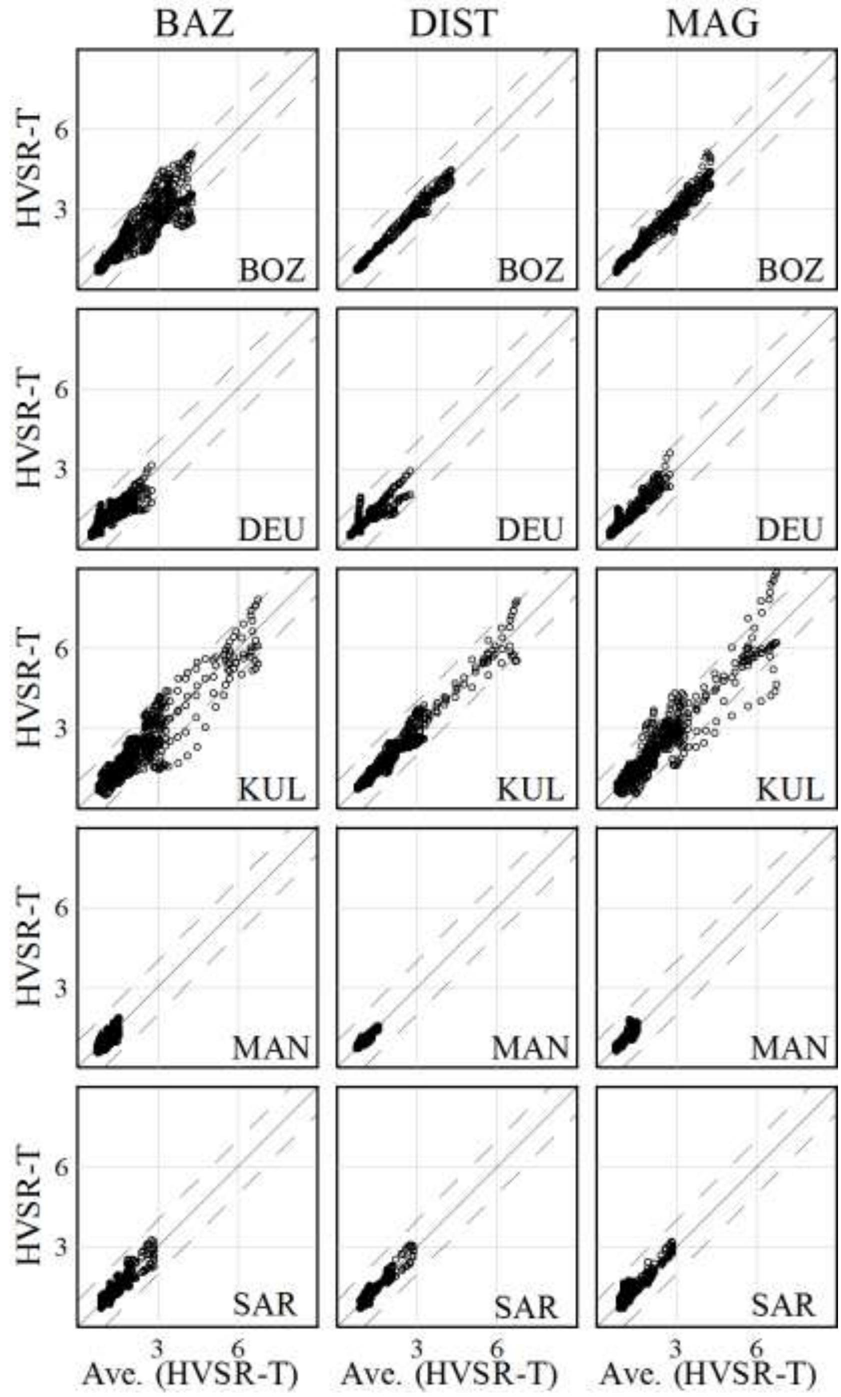

Figure 4.4 Scattering of individual HVSR-T results versus the average HVSR-T values (*Ave*) for the sites. Black solid line (linear fit trough origin) represents correlation between average of all individual event results and average of each subgroup arithmetic mean results for each station. Black dashed lines indicate a linear fit within a factor of 2 (continued).

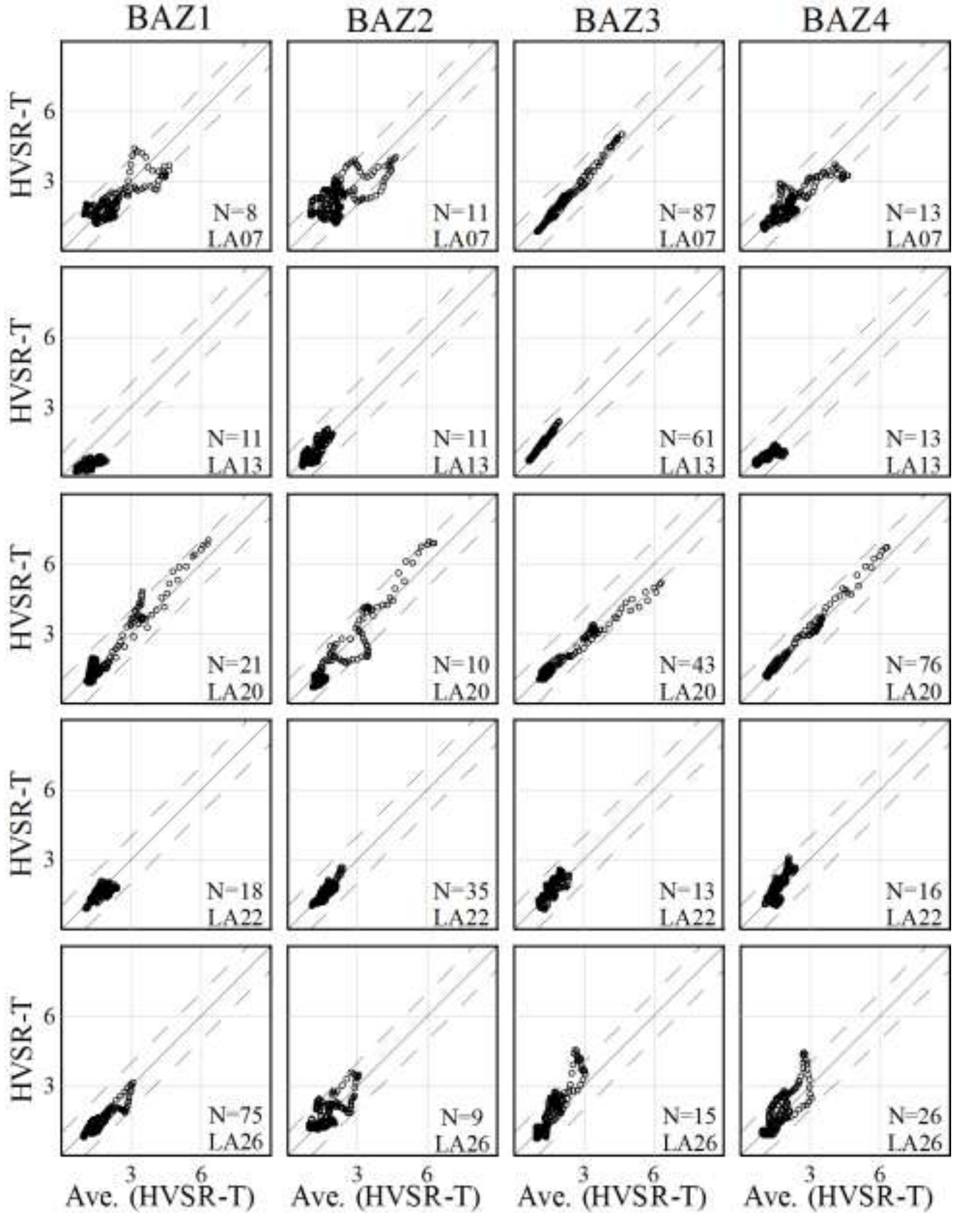

Figure 4.5 Scattering of individual HVSR-T results versus the average HVSR-T values (*Ave*) of each back-azimuth group for ten sites. Back-azimuth values were divided as four groups ($0 \leq$ BAZ1 < 90; $90 \leq$ BAZ2 < 180; $180 \leq$ BAZ3 < 270; $270 \leq$ BAZ4 < 360). Black solid line (linear fit trough origin) represents correlation between average of all individual event results and average of each subgroup arithmetic mean results for each station. Black dashed lines indicate a linear fit within a factor of 2. *N*: number of data used for each subgroup.

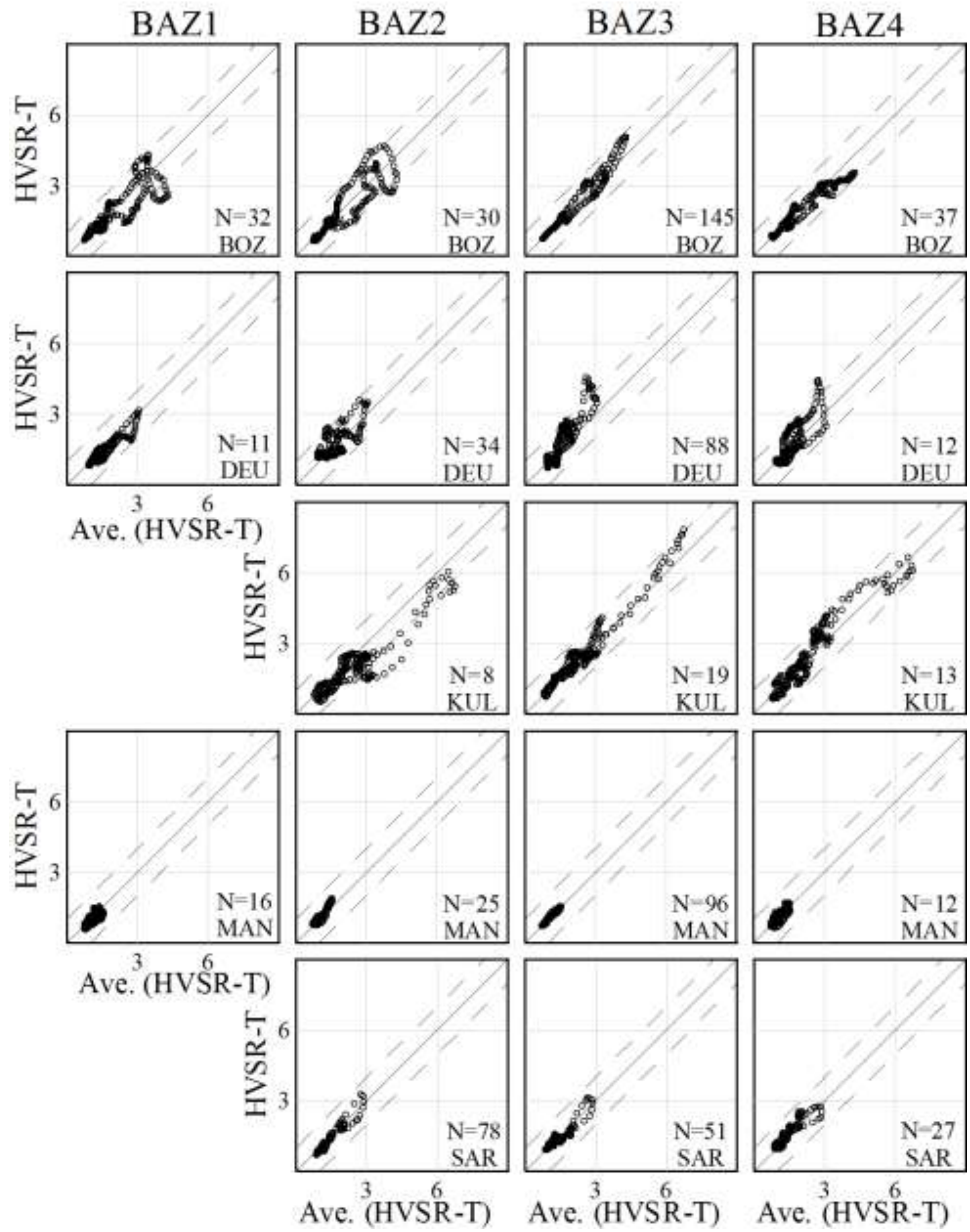

Figure 4.5 Scattering of individual HVSR-T results versus the average HVSR-T values (*Ave*) of each back-azimuth group for ten sites. Back-azimuth values were divided as four groups ($0 \leq$ BAZ1 < 90; $90 \leq$ BAZ2 < 180; $180 \leq$ BAZ3 < 270; $270 \leq$ BAZ4 < 360). Black solid line (linear fit trough origin) represents correlation between average of all individual event results and average of each subgroup arithmetic mean results for each station. Black dashed lines indicate a linear fit within a factor of 2. *N*: number of data used for each subgroup (continued).

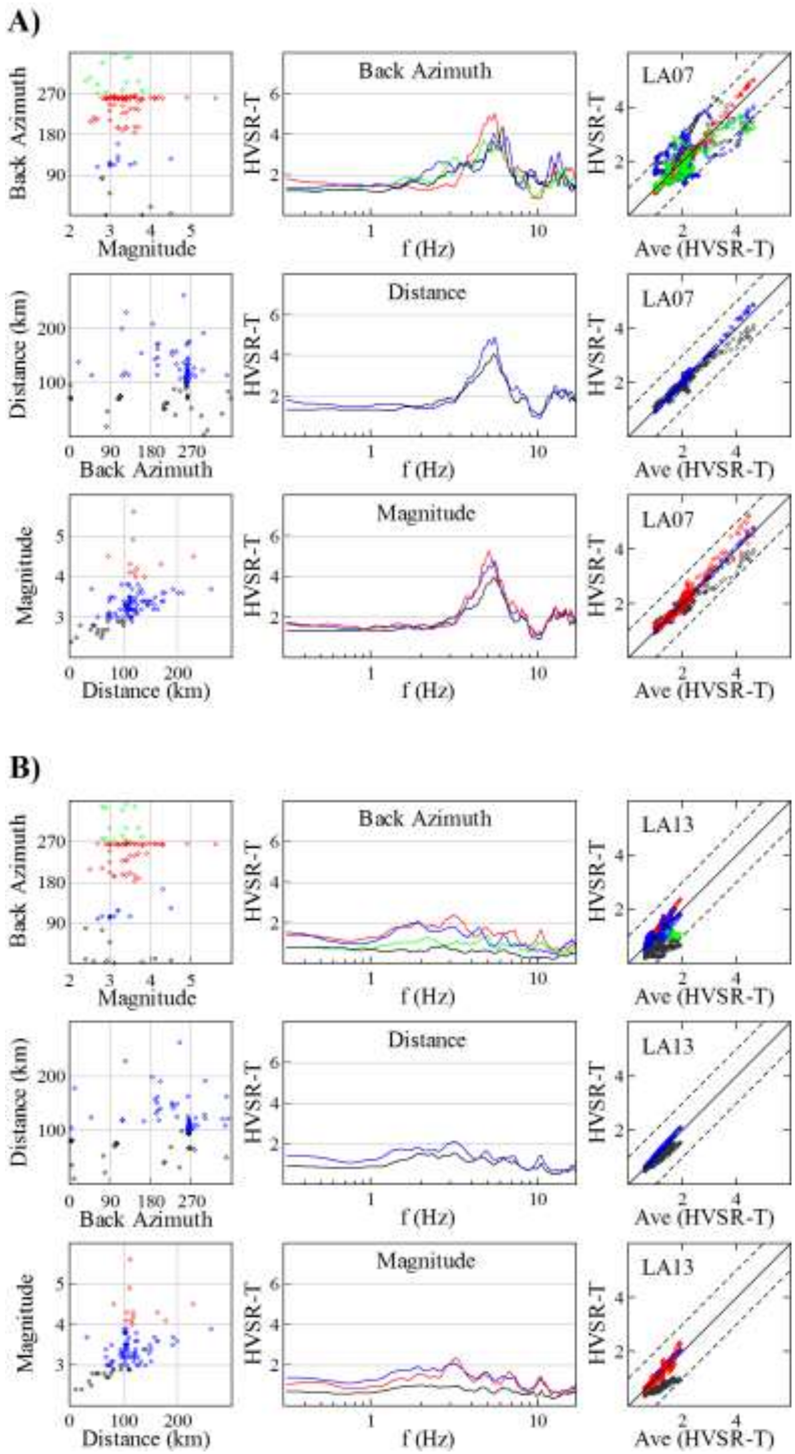

Figure 4.6 Scatterings from average HVSR-T estimates of different back-azimuth, distance and magnitude groups for the A) LA07, B) LA13, C) BOZ and D) DEU sites. Back-azimuth values were divided as four groups (0 ≤ BAZ1 < 90; 90 ≤ BAZ2 < 180; 180 ≤ BAZ3 < 270; 270 ≤ BAZ4 < 360). Epicentral distance values were divided into two groups (DIST1 ≤ 100 km < DIST2). Local magnitude values were divided into three groups (M_l < 3; 3 ≤ M_l<4; 4 ≤ M_l). *Ave* Arithmetic mean of HVSR-T results for the site.

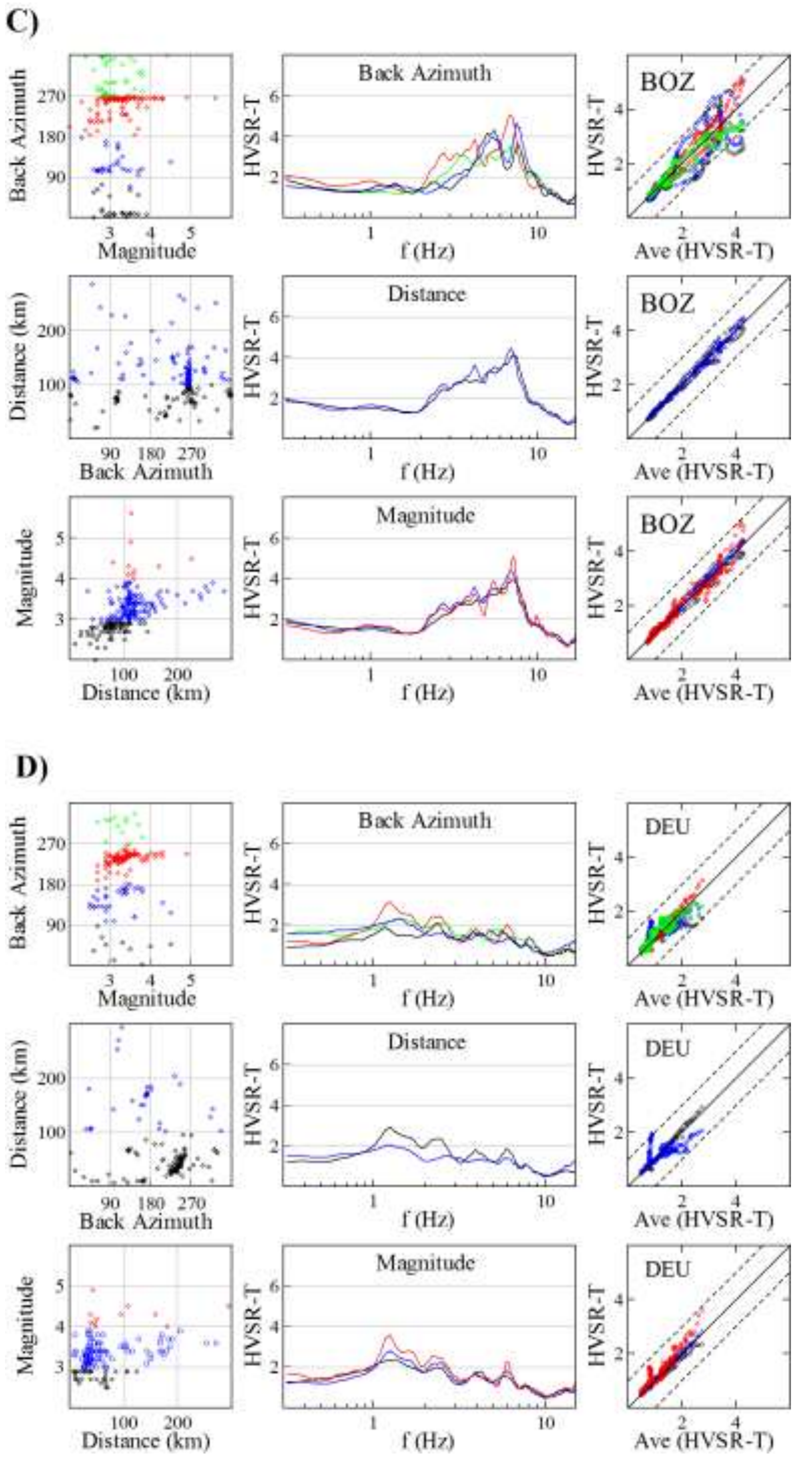

Figure 4.6 Scatterings from average HVSR-T estimates of different back-azimuth, distance and magnitude groups for the **A)** LA07, **B)** LA13, **C)** BOZ and **D)** DEU sites. Back-azimuth values were divided as four groups (0 ≤ BAZ1 < 90; 90 ≤ BAZ2 < 180; 180 ≤ BAZ3 < 270; 270 ≤ BAZ4 < 360). Epicentral distance values were divided into two groups (DIST1 ≤ 100 km < DIST2). Local magnitude values were divided into three groups (M_l < 3; 3 ≤ M_l<4; 4 ≤ M_l). *Ave* Arithmetic mean of HVSR-T results for the site (continued).

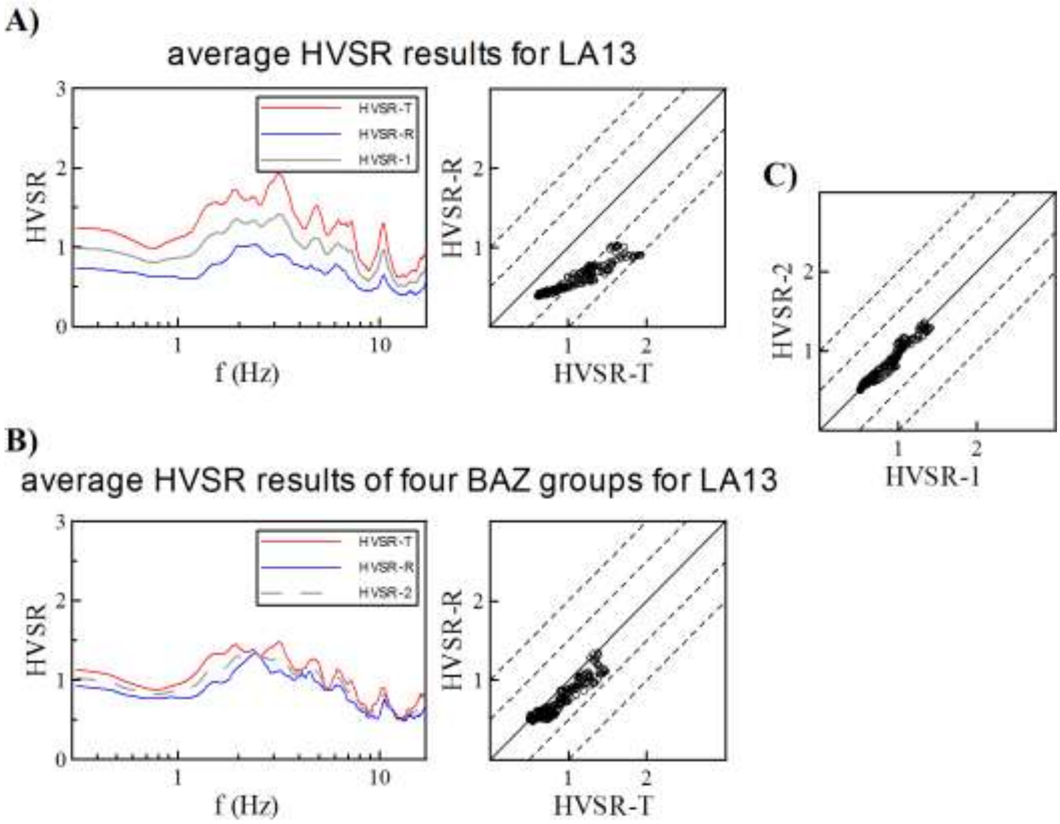

Figure 4.7 HVSR-T (Çamyıldız, 2008) and HVSR-R estimates for LA13 site. Comparison of: A) Average HVSR-T and HVSR-R functions (HVSR-1 is average of them). B) HVSR-T and HVSR-R functions by averaging of four back-azimuthal group arithmetic mean HVSR values (HVSR-2 is average of them). C) HVSR-1 and HVSR-2 results.

4.3 SSR Method and Results

If it is assumed that the records from two nearby stations contain the same source and propagation effects; the spectral ratio of the sedimentary site with respect to the reference site is:

$$\frac{U_{ij}(f,r)}{U_{ik}(f,r)} = \frac{S_i(f)P_{ij}(f,r)Z_j(f)}{S_i(f)P_{ik}(f,r)Z_k(f)} \tag{4.8}$$

where $U_{ij}(f,r)$ and $U_{ik}(f,r)$ are the spectral amplitudes of the ground motions observed at a recording site j and a reference station k for an event i. f is the frequency, r is the hypocentral distance, $S_i(f)$ is the source function, $P_{ij}(f,r)$ and $P_{ik}(f,r)$ are path effects at site j and reference station k, respectively. $Z_j(f)$ is the response of site j and $Z_k(f)$ is the response of reference station k (Parolai, 2012). Because k is the reference station, $Z_k=1$ and then $P_{ij}(f,r) \approx P_{ik}(f,r)$. Thus, the spectral ratio can be written by the following equation:

$$\frac{U_{ij}(f,r)}{U_{ik}(f,r)} \approx Z_j(f) \tag{4.9}$$

As can be seen eq. (4.9) the spectral ratio should directly give the site response at the station j.

In this study, only the LA13 and LA22 sites were chosen as reference sites for SSR applications, although they got some deviations from HVSR estimate ~1 value. Most of reference rock sites in the literature show same matter (e.g., Bindi et al., 2009; Bonilla et al., 1997; Parolai et al., 2004) and ideal reference sites would require uniform, perfectly elastic half-spaces (Malagnini et al., 2004). To calculate SSR, epicentral distance ratio of station to reference site was limited between the values of 0.9 and 1.1. Only the data with epicentral distances at least four times larger than station-reference site distance were evaluated. Because of these restrictions, a few stations have enough data recorded at both a site of interest and the reference site. For that reason, SSR of transverse S-waves were obtained only for 8 stations as shown in Fig. 4.8. While LA13 and LA22 were evaluating as the reference sites, SSR estimates were checked for four back-azimuth groups and averaged to avoid back-azimuth dependency effects of chosen reference sites. Note that, SSR results for the BOZ site were estimated by utilizing both of the chosen reference sites in Fig. 4.8.

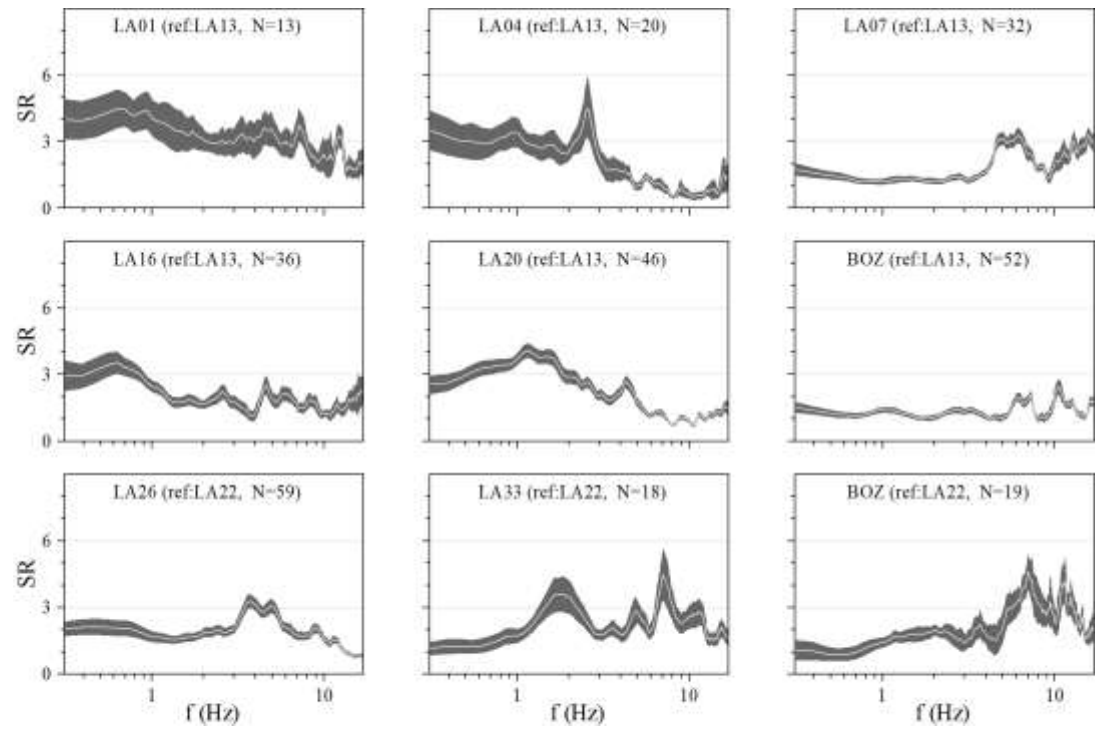

Figure 4.8 The average SSR results of transverse S-waves for 8 sites with 90% confidence interval from *t*-test. SSR results for the BOZ site were estimated by utilizing both of the chosen reference sites.

CHAPTER FIVE
SEPARATION OF SOURCE, SITE, REGIONAL AND NEAR-SURFACE ATTENUATION EFFECTS

5.1 Overview

The purpose of this chapter is to estimate source spectra, attenuation along the path and site amplification effects in the central west Turkey using a generalized inversion scheme. Describing of these effects is needed for simulation of possible large earthquakes which provides both assessing the seismic hazard in the region and generation of the building codes/or renewing previous ones. The common approach to separate the earthquake source processes, path effects and site amplification is to apply generalized inversion techniques (GIT) to the recorded ground motion data. GIT was first proposed by Andrews (1986). He used a reference site assumption in two different ways: 1) the site amplification at the stations chosen as reference sites have a flat transfer function with amplitude of one or; 2) the average of the site effect over all sites is unity. Then, this technique has been developed by many researchers (e.g., Boatwright et al., 1991; Castro et al., 1990; Hartzell, 1992) to decompose source, propagation and site terms, separately and/or simultaneously. Nowadays, it has become a standard tool to evaluate these effects at engineering seismology.

In general, the amplitude spectrum of a ground motion observed at a site *j* from an event *i* can be expressed as following:

$$U_{ij}(f,r) = S_i(f)A\left(f,r_j\right)Z_j(f) \tag{5.1}$$

where $S_i(f)$ denotes the source function, $A(f,r_j)$ is the attenuation effect along the hypocentral distance r_j and $Z_j(f)$ is the local site function (Castro et al., 2003). By taking the logarithm, the problem can be linearized for a fixed frequency *f*:

$$logU_{ij}(f,r) = logS_i(f) + logA\left(f,r_j\right) + logZ_j(f) \tag{5.2}$$

There are two inversion approaches to evaluate this linear system. In the first approach; the attenuation, source and site functions are described parametrically, whereas, the inversion is carried out without adopting any assumed parametric shape in the second one. Effective results have been acquired applying both parametric (e.g., Andrews, 1986; Castro et al., 1990; Drouet et al., 2008; Salazar et al., 2007) and non-parametric approaches (e.g., Bindi et al., 2006; Castro et al., 1990; Oth et al., 2011; Parolai et al., 2000, 2004) of GIT. The latter approach provides to obtain average amplitude decay as a function of distance and also allows us splitting the problem into sub-inversion steps. Calculating these steps makes the inversion problem more suitable and reduces the number of unknowns for each step (Castro et al., 2003; Oth, 2007; Parolai et al., 2004). Additionally, one can also has a chance to easily test non-parametric form of attenuation functions against any parametric form (Castro et al., 1990). Another advantage of the approach is that negative Q values can also be avoided in the non-parametric form of attenuation functions. This issue commonly arises due to improper geometrical spreading assumptions, when the seismic waves are amplified with increasing distance traveled, in the case where focusing effects play a role (Oth, 2007).

5.2 Propagation Characteristics

In order to estimate potential seismic hazard due to ground motion in an area, understanding the nature of the transmitting medium on the seismic waves are required. Seismic attenuation can be described as the amplitude decay and change in frequency content of seismic waves during the passage of them through the earth's interior (Erdik & Durukal, 2003). Velocity properties of a medium affect propagation of seismic waves. Refraction, reflection, diffraction, wave conversion, multipathing (focusing and defocusing) and attenuation (due to anelasticity, scattering and geometric spreading) are the propagation phenomena effecting seismic wave amplitudes. Some of them can be described by elastic wave theory. All of them cause increase or decrease of arrival's amplitude as a shift in energy within the wave field. Anelasticity, which is sometimes called intrinsic attenuation, is an irreversible conversion of seismic energy to heat and reduces elastic wave amplitudes (Stein & Wysession, 2003).

The velocities and attenuation of seismic waves are two major properties affecting the propagation of seismic waves. The determination and describing the distribution of them gives us the chance to better understand the mineralogical, chemical, and thermal structure of the earth's interior (Stein & Wysession, 2003). Although measuring of attenuation and understanding its physical causes are difficult, the studies related to the loss mechanism bring additional information about the physical state of the earth. Using this new additional information, a more realistic model describing the energy transport phenomenon within the earth can be created (Stein & Wysession, 2003).

5.2.1 Anelasticity or Intrinsic Attenuation

Attenuation is mainly caused by anelastic wave damping and scattering properties of medium as well as the geometric spreading of seismic waves. Scattering involves redistribution of seismic energy, when the seismic waves encounter with small-scale heterogeneities such as cracks or other lateral velocity variations. It does not dissipate the elastic energy, but the energy of the seismic waves is redistributed in different directions or with different polarizations (Syuhada, 2010). Thus, scattering causes arrival's amplitude as a shift in energy within the wave field. Anelasticity or intrinsic attenuation arises in response to deviation from elasticity and the seismic energy of a propagating wave transforms into heat. It may be caused by thermal currents, microscopic mechanisms and inter-atomic forces such as frictional sliding on crystal grain boundaries, stress-induced migration of defects in minerals (Lay & Wallace, 1995; Stein & Wysession, 2003). These processes that involve the irreversibly conversion of energy are known as *internal friction* and represent deviation from elasticity within the earth.

The attenuation of seismic waves is generally described by quality factor (Q) which is defined as the fractional loss of energy per cycle as:

$$\frac{2\pi}{Q} = -\frac{\Delta E}{E} \tag{5.3}$$

where ΔE is the energy loss in per cycle and E is the total elastic energy stored in the wave. Q describes the performance of an oscillatory circuit and has come from electric circuit theory into the geophysical literature. Dimensionless parameter Q is generally parameterized in terms of Q^{-1} since it represents multiplicative reciprocal of attenuation parameter. In order to theoretically describe intrinsic attenuation, a damped harmonic oscillator composed of a spring and a dashpot can be used (Stein & Wysession, 2003). A frictionless system which has a purely elastic response can be analyzed. So a general solution of this system is given by:

$$u(t) = A_0 \cos(\omega_0 t) \tag{5.4}$$

where ω_0 and A_0 represent natural frequency of the system and amplitude value at the source. To take into account the loss of energy, a dashpot or damping factor, γ, can be added into the system. It is assumed that attenuation is linear and is approximately linearly dependent on frequency for the solution. The quality factor is defined to simplify this as following:

$$Q = {}^{\omega_0}/_{\gamma} \tag{5.5}$$

Thus, the solution for the damped harmonic displacement is:

$$u(t) = A_0 e^{-\omega_0 t/2Q} \cos(\omega t) \tag{5.6}$$

The exponential term states the temporal decay of seismic wave amplitude:

$$A(t) = A_0 e^{-\omega_0 t/2Q} \tag{5.7}$$

Q can be used to describe the spatial decay of oscillation in a propagating wave at fixed frequency. t can be replaced with r/v, where r is the distance traveled and v is the velocity, for traveling waves (Stein & Wysession, 2003). Thus, following equation describes how the amplitude decays with the distance:

$$A(r) = A_0 e^{-\omega_0 r/2vQ} \tag{5.8}$$

The most basic way to measure Q within the earth is taking the logarithm of eq. (5.7):

$$lnA(t) = lnA_0 - \omega_0 t/2Q \tag{5.9}$$

and fitting a straight line to the logarithmic attenuation functions. Thus, Q can be found from the slope of the decay. Alternatively, if we consider the damping of a seismic wave as a function of the distance and we have explicit peaks which separated from each other along to the wavelength (λ) of the wave

$$A_1(k_1) = A_0 \exp(-\omega_0 k_1/2vQ) \tag{5.10}$$

and

$$A_2(k_1 + \lambda) = A_0 \exp(-\omega_0 (k_1 + \lambda)/2vQ) \tag{5.11}$$

where *A1* and *A2* are amplitudes at two different distances. Their ratio is:

$$A_1/A_2 = \exp[-\omega_0 k_1/2vQ - \omega_0 (k_1 + \lambda)/2vQ] = \exp(\pi/Q) \tag{5.12}$$

so Q can be found from logarithmic decrement of a harmonic wave as:

$$Q = \pi/ln\,(A_1/A_2) \tag{5.13}$$

The damping of a seismic wave could be clarified as a function of the distance. A cycle of an oscillation corresponds to the distance traveled of seismic wave and is represented by the wavelength (λ) of the wave (Lowrie, 1997). Thus, eq. (5.3) can be rewritten for this case as:

$$\frac{2\pi}{Q} = -\frac{1}{E}\lambda\frac{dE}{dr} \tag{5.14}$$

$$\frac{dE}{E} = -\frac{2\pi}{Q}\frac{dr}{\lambda} \tag{5.15}$$

The energy of wave is proportional to the square of its amplitude A. Thus the following equation can be written from eq. (5.15):

$$\frac{dE}{E} = \frac{2dA}{A} \tag{5.16}$$

By using eqs (5.15) and (5.16), the attenuation of a seismic wave at distance r from its source is given by as following:

$$A = A_0 exp(-\frac{\pi r}{Qv}) \tag{5.17}$$

The quality factor is an important parameter in seismology. The knowledge of the Q structure of the earth provides new insights on its internal structure and evolution of the Earth. This parameter is also used for magnitude determination and predicting earthquake ground motion (Mitchell & Romanowicz, 1998). It has long been known that attenuation is dependent on the variations of temperature and pressure in the Earth and varies both laterally and vertically (Romanowicz, 1995). Lay & Wallace (1995) stated that tectonically active regions typically have relatively high heat flow and high attenuation than colder regions. Besides, movement of solid-state defects, partial melt and fluid content have a great effect on the damping of seismic wave amplitudes (Mitchell & Romanowicz, 1998).

The greatest attenuation (lowest Q~10) observed near the surface in the crust (~ in the upper 100 m) especially in active tectonic regions and increases rapidly with depth to a few kilometers. This near-surface attenuation appears to be almost independent of rock type. The observations suggest that the main cause of near-surface attenuation is the generation of cracks and fractures with decreasing lithostatic pressure and the fluid flow in these structures (Abercrombie, 1998; Stein & Wysession, 2003). Attenuation in the crust reaches its lowest level around 20-25 km and then increases again probably due to increasing temperature (Mitchell, 1995). The deeper parts within the interior, Q does not indicate a significant change until the 80 km. Between 80 and 220 km, attenuation is highest in the upper mantle, most probably due to the temperature reaches and perhaps exceeds the melting temperatures of rock. Q-structure estimates have stated that the most of the anelastic losses in the upper mantle roughly corresponds to the depth of the low velocity zones (Der, 1998). Beneath the astenosphere, Q increases gradually with depth, presumably because temperature increases at a slower rate than pressure (Stein & Wysession, 2003). As a result, the distribution of regional difference in Q values can be used to distinguish tectonically active regions for seismic hazard studies. Significant lateral variations of Q values can occur in the upper mantle. Low Q values are observed in the hot back-arc basin and the mid-ocean ridge, whereas high Q values indicate the old oceanic crust and shield areas (Barazangi et al., 1975; Der, 1998; Oliver & Isacks, 1967). The anelastic structure within the earth shows significant lateral variations. Low crustal Q values indicate more attenuative areas in the tectonically active regions. By contrast, stable areas have higher Q values.

5.2.2 Geometrical Spreading

The most obvious effect causing amplitude decay with distance is geometrical spreading, in which the energy per unit varies as a wave front expands and contracts (Stein & Wysession, 2003). If there is no energy loss due to friction in a homogeneous medium, the propagation of seismic waves can be figured as spherical wavefronts, and then the amplitude decay can be described by the decrease in energy distributed over the wavefront surface (Oth, 2007). The geometrical spreading can be expressed as follows:

$$G(r) = \frac{1}{r^b} \tag{5.18}$$

where r is the distance from source to site and b is the geometrical spreading coefficient of amplitude decay. The corresponding b coefficients of amplitude decay are 1 and 0.5 for body and surface waves, respectively. These assumptions are only valid in a purely homogenous media at short distances. Many studies on body-wave attenuation (e.g., Castro et al., 2008b, 2009; Ibáňez et al., 1993) show that the geometrical spreading coefficient associated with distance may be more complicated than a simple assumption of $b=1$. In fact, the geometrical spreading of regional phases is a complicated function of crustal and upper mantle velocity structure (Olafsson et al., 1998; Padhy 2009; Sereno & Given, 1990) of heterogeneous media. Thus, the geometrical spreading models are path specific and depend on several factors: focal depth, crustal thickness and the existence of a strong discontinuity as well as crustal velocity gradient (Akıncı et al., 2006).

5.3 Applied Inversion Steps and Results

5.3.1 Data

Although the data and its initial processing stages have already been described in Chapter 3, to improve the resolution of the inversion steps, the data were restricted to stations having at least ten records and earthquakes recorded by at least three stations. Remaining 1764 three-component recordings for 322 events were evaluated. Figure 5.1 shows the locations of the stations and earthquakes used in inversion steps. Figure 5.2 represents ray path coverage of the dataset. This dataset includes events with local magnitudes ranging from 2.0 to 5.6, hypocentral distances range between 3.5 and 205 km, and focal depths range from 1.4 to 27 km (Fig. 5.3).

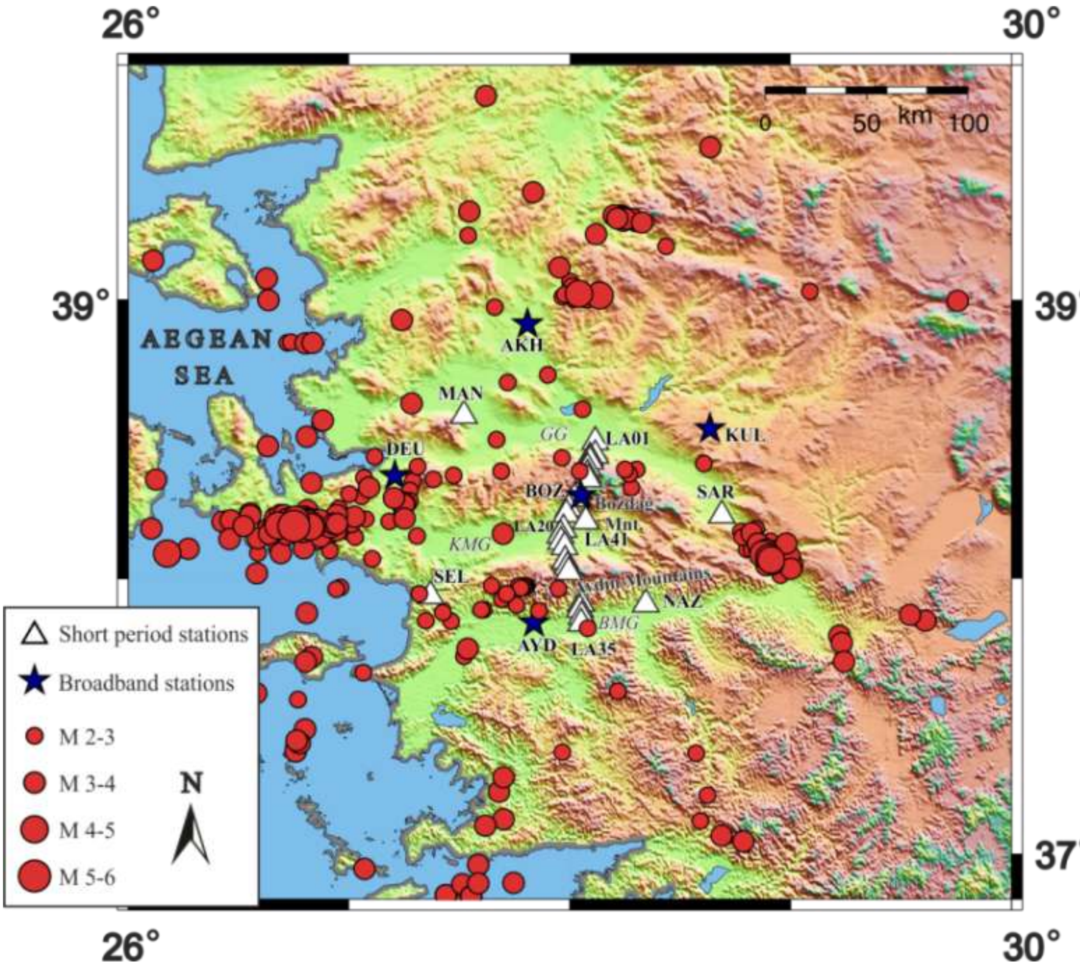

Figure 5.1 Locations of the stations and distribution of earthquakes (red dots) used in inversion steps. White triangles and blue stars indicate short period and broadband stations of WASRE network, respectively.

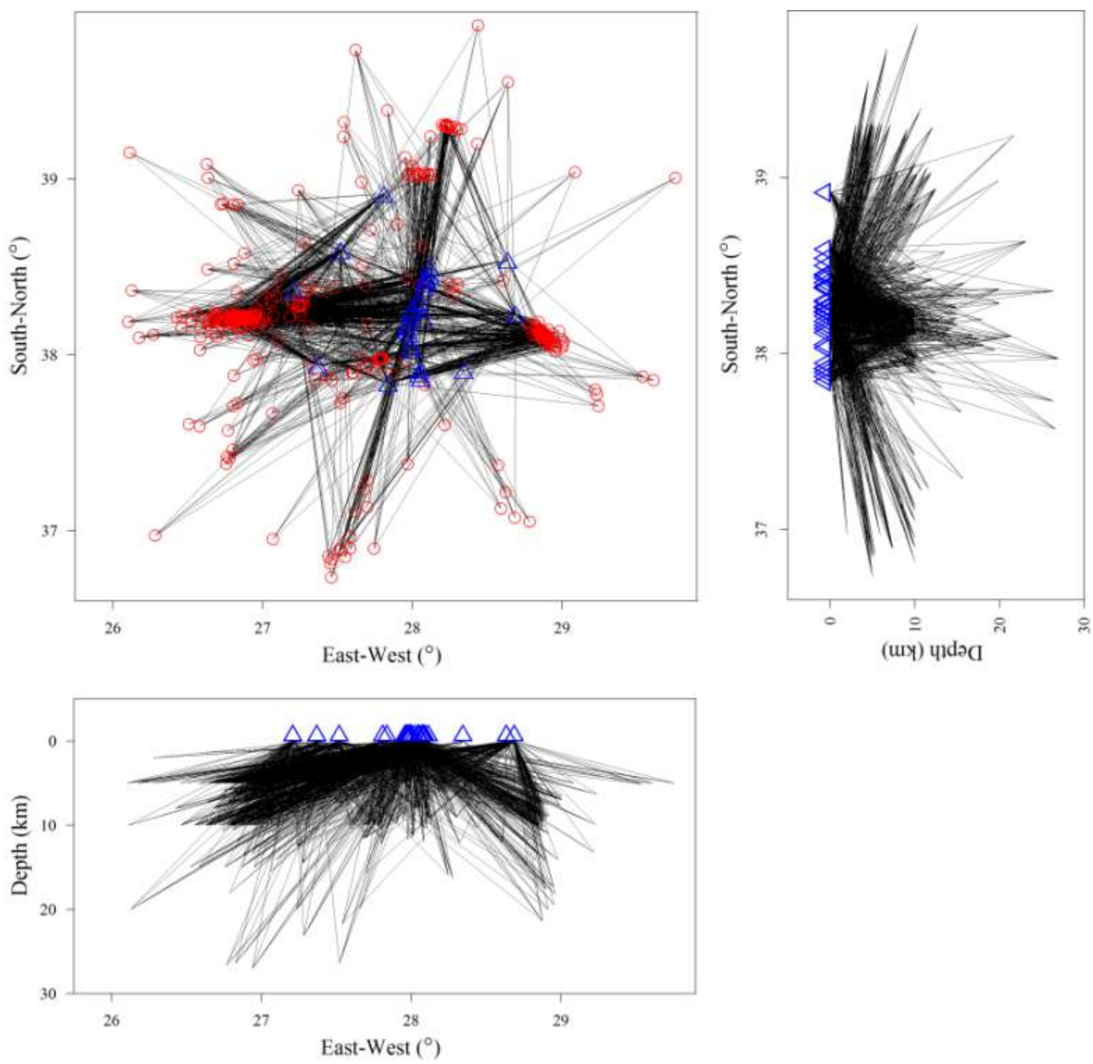

Figure 5.2 Schematic ray coverage of 322 events used in inversion steps. Solid lines represent schematic ray paths from the epicenters to stations.

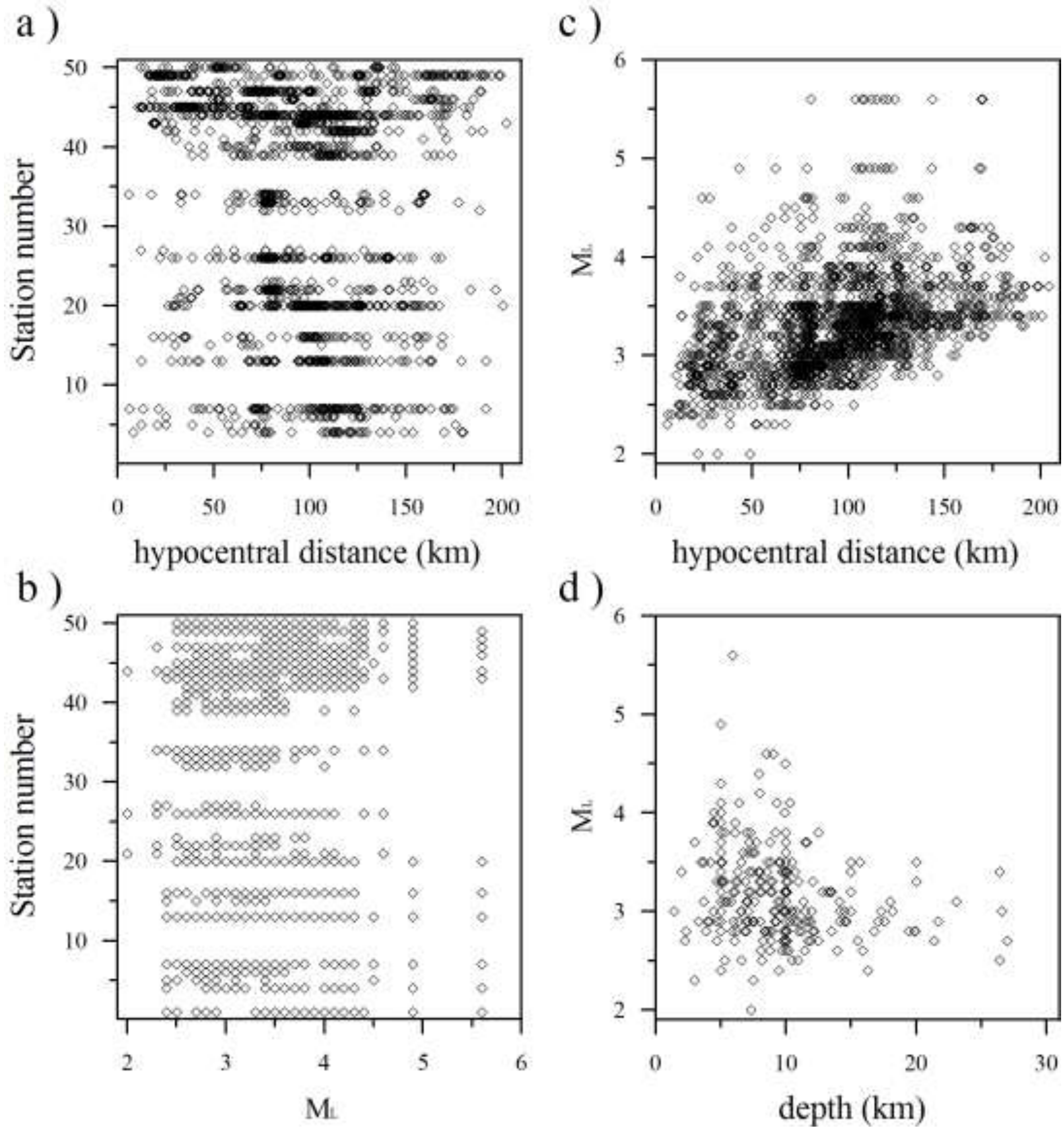

Figure 5.3 The distributions of dataset used in inversion steps: (a) and (b) depict station numbers (denoted in Table 3.1) versus hypocentral distances and local magnitudes, whereas (c) and (d) represent local magnitudes versus hypocentral distances and depths of earthquakes, respectively.

5.3.2 Non-parametric Attenuation Model

The attenuation functions, including anelasticity of heterogeneous media and geometrical spreading effects, were obtained using a non-parametric approach described by Castro et al. (1990). The observed spectral amplitude decay versus hypocentral distance in eq. (5.1) can be explained as following:

$$U_{ij}(f,r) = M_i(f)A(f,r_j) \tag{5.19}$$

where $U_{ij}(f,r)$ represents the observed spectral amplitude for event i at station j, while $A(f,r_j)$ and $M_i(f)$ represent the attenuation function and source term, respectively. $M_i(f)$ is a scalar source term (one for each earthquake i at frequency f) that depends on the size of the earthquake. In this approach, $A(f,r)$ is just constrained to be a smooth decaying function of hypocentral distance. It is assumed that it exactly includes all attenuation effects such as geometrical spreading, anelasticity, scattering and refracting arrivals (Cantore et al., 2011; Oth et al., 2011). This equation can be linearized as following:

$$logU_{ij}(f,r) = logM_i(f) + logA(f,r_j) \tag{5.20}$$

Matrix form of eq. (5.20) can be written as:

$$\left(\underbrace{\begin{matrix} 1 & 0 & 0 & . & \dots \\ 0 & 1 & 0 & . & \dots \\ . & . & . & . & \dots \\ 1 & 0 & 0 & . & \dots \\ \vdots & \vdots & \vdots & \vdots & \vdots \\ \omega_1 & 0 & 0 & . & \dots \\ -\omega_2/2 & \omega_2 & -\omega_2/2 & \cdot & \cdots \\ 0 & -\omega_2/2 & \omega_2 & -\omega_2/2 & \cdots \\ . & . & . & . & \dots \end{matrix}}_{attenuation\ parameters} \middle| \underbrace{\begin{matrix} 1 & 0 & 0 & \cdot & \cdots \\ 1 & 0 & 0 & \cdot & \cdots \\ \cdot & \cdot & \cdot & \cdot & \cdots \\ 0 & 1 & 0 & . & \cdots \\ \vdots & \vdots & \vdots & \vdots & \vdots \\ \cdot & \cdot & \cdot & \cdot & \cdots \\ \cdot & \cdot & \cdot & \cdot & \cdots \\ \cdot & \cdot & \cdot & \cdot & \cdots \\ . & . & . & . & \dots \end{matrix}}_{source\ terms}\right) \cdot \begin{pmatrix} a_1 \\ \cdot \\ \cdot \\ \cdot \\ a_j \\ m_1 \\ \cdot \\ \cdot \\ m_i \end{pmatrix} = \begin{pmatrix} u_{11} \\ \cdot \\ \cdot \\ u_{ij} \\ \vdots \\ 0 \\ 0 \\ 0 \\ \cdot \end{pmatrix} \tag{5.21}$$

in where $m_i = \log M_i(f)$ and $a_j = \log A(f,r_j)$ are logarithm of source terms and attenuation function, respectively. ω_1 is a weighting factor to constrain the attenuation function to take the value $A(f, r_0) = 1$ at the reference distance r_0 ($r_0 = 0$ is commonly chosen). ω_2 is used to determine the degree of smoothness of the solution by placing a small second derivative of the curves. It controls the smoothness of attenuation function and choosing an optimal ω_2 value allows us preserving the monotonic characteristic of the attenuation function. There is not a certain criteria related to the selection of the weighting factor. In practice, it is selected by visual examination in multiple runs (Castro et al., 1990). If ω_2 is too small, the undulations of the data regard to site effects are not effectively suppressed. On the other hand, if chosen ω_2 is too large, the attenuation functions will result in straight lines which means that the attenuation function cannot preserve properly the variations of attenuation characteristics with distance (Oth, 2007; Syuhada, 2010). This linear matrix system in eq. (5.21) can be written in following form:

$$Ax = b \tag{5.22}$$

where x is the solution vector contains the model parameters m_i and a_j, b is a vector in the data space containing observed spectral amplitudes and A is, called the data kernel, a matrix relating x to b. GIT problems in seismology are generally over-determined, because the dataset includes at least one record for each station and one record for each source (Oth, 2007). In this study, S-wave amplitudes were restricted to stations having at least ten records and earthquakes recorded by at least three stations in order to increase the resolution of the inversion steps. Thus, the solution can be expressed by means of least-square solution:

$$x = (A^T A)^{-1} A^T b \tag{5.23}$$

Singular Value Decomposition method (Menke, 1989) is used to solve this linear system and all calculations are carried out for 26 different frequencies. In order to see whether or not there is any significant site effect of vertical components and also to be able to compare site functions obtained from non-parametric inversion method with the HVSR and SSR results, eq. (5.20) was applied to T-, R- and V-component of the ground motions. Figure 5.4 shows observed spectral amplitudes for an M_L = 4.3 event along with estimated amplitude decrease from T- component spectra. The attenuation functions were obtained by inverting all data from 322 events, simultaneously. The general characteristics of the attenuation functions are consistent with the data. The dispersion of the data could be attributed to site response of the stations used (Castro et al., 1999). Figure 5.5 shows the estimated non-parametric attenuation functions of T-, R- and V-components. Apparent lack of attenuation was observed between 70 and 120 km. The slopes of attenuation curves show significant changes for 10-70 and 120-200 km distance ranges at lower frequencies. RMS values of the residuals associated with the inversion results are given in Fig. 5.6.

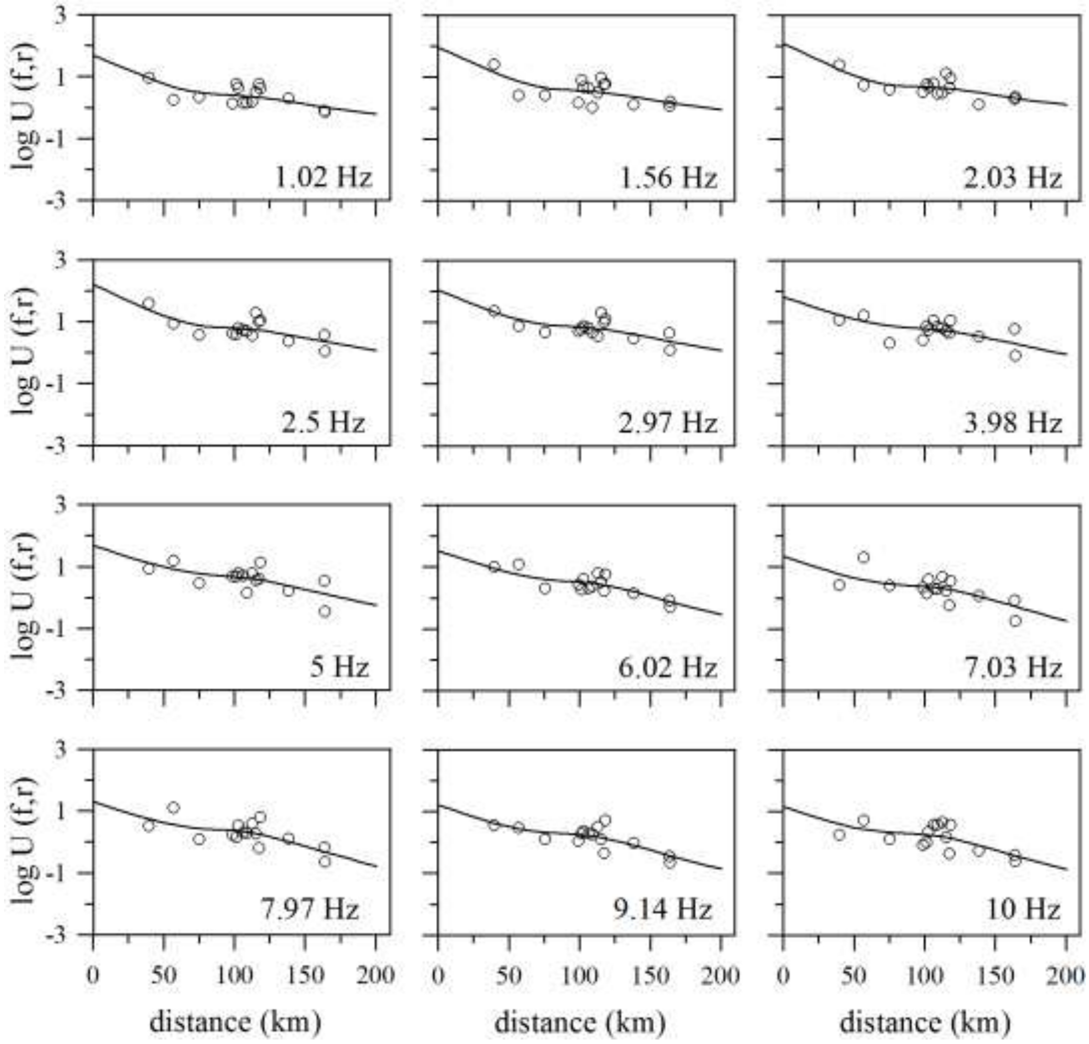

Figure 5.4 Observed spectral amplitudes (circles) for an event (M_L= 4.3) and estimated amplitude decrease from T-component (solid lines) for 12 frequencies.

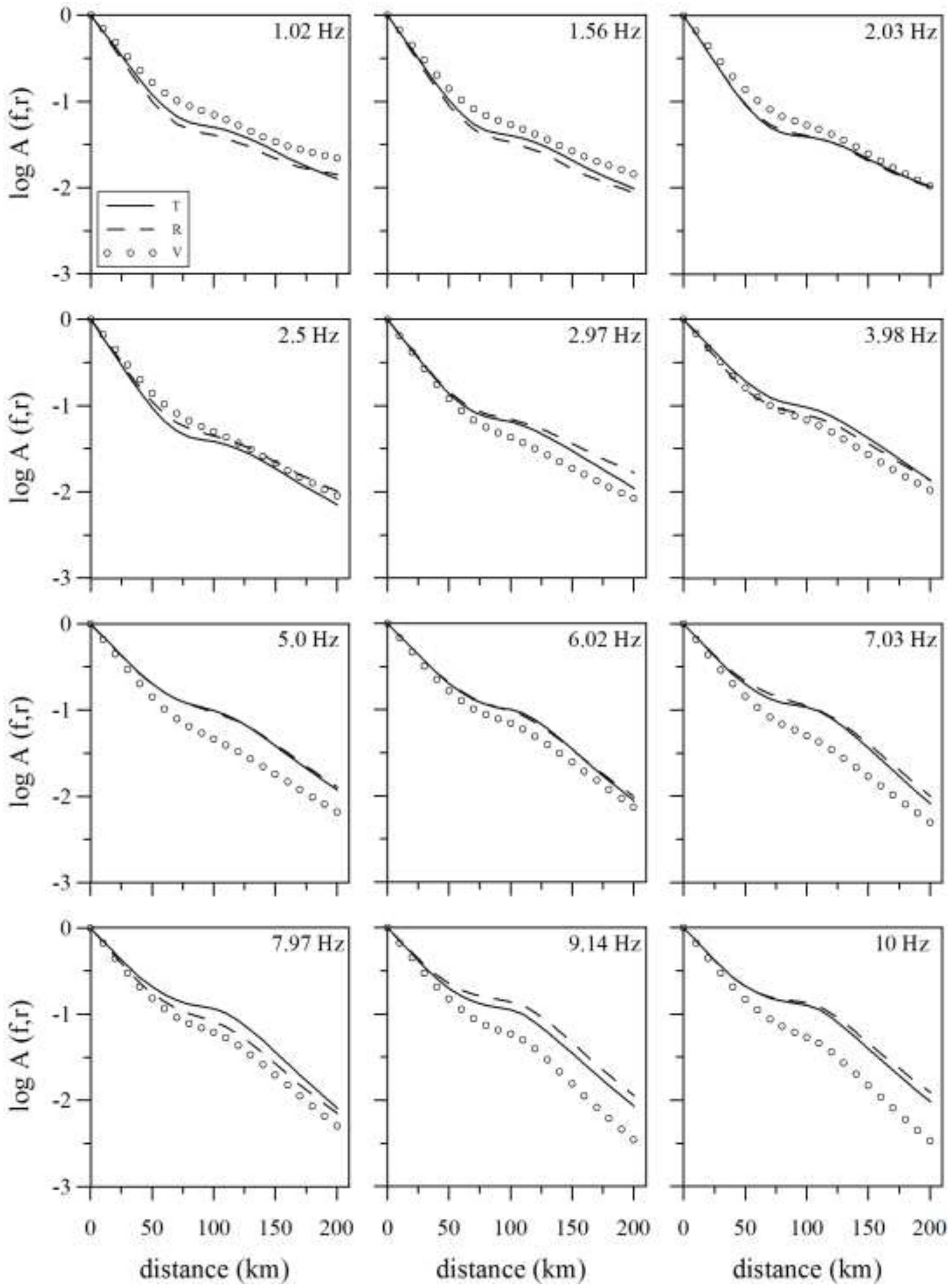

Figure 5.5 Comparison of the estimated non-parametric attenuation functions for 12 frequencies. Black solid-, dashed-lines and white dots represent T-, R- and V- component results, respectively.

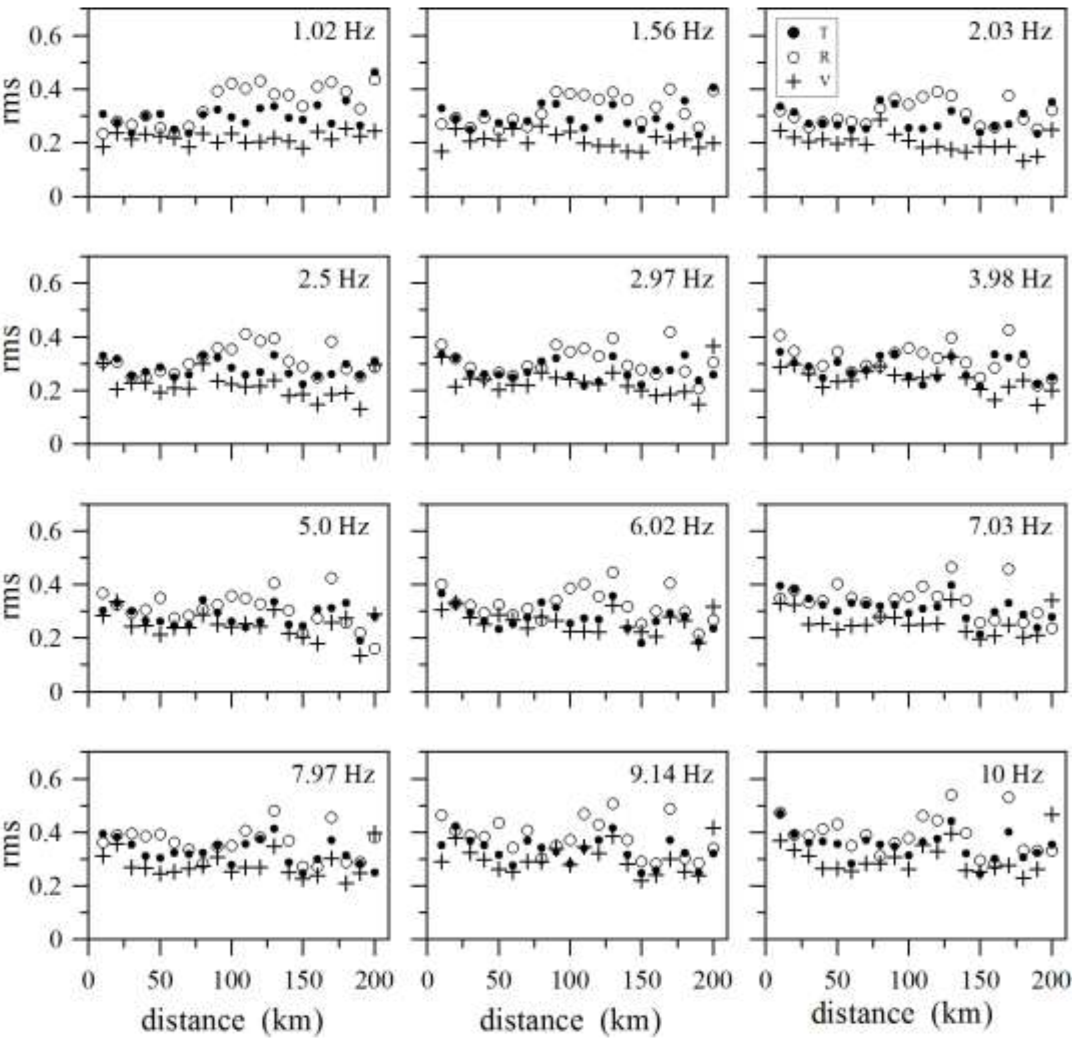

Figure 5.6 RMS values of residuals associated with the first inversion step in eq. (5.20) and the results in Fig. 5.5. Dots, circles and crosses represent RMS values of residuals for T-, R- and V- component, respectively.

5.3.3 Parameterization of Attenuation Function, A(f,r)

Assuming that residuals in eq. (5.20) is the product of source spectra, site response, and near-surface propagation effects are carried by the site term, and also the source term probably includes the array coverage of the near-surface attenuation effect (e.g., Castro et al., 1990, 1999, 2008a), the attenuation function can be modelled as following:

$$A(f,r) = G(r)e^{\frac{-\pi f r}{vQ}} \tag{5.24}$$

where $A(f,r)$ represents the attenuation curve at a fixed frequency f and r is the hypocentral distance in km. The first right-hand term accounts for geometrical spreading and the second right-hand term is for amplitude decrease due to total Q (intrinsic and scattering). To describe the observed frequency dependence of the estimated values of Q, well known functional form was used:

$$Q(f) = Q_0 f^n \tag{5.25}$$

where Q_o is the value of Q at 1 Hz and n is frequency dependence of Q values. The parameter v in eq. (5.24) is the average S-wave velocity (v_s= 3.2 km/s), based on the crustal structure, given by Akyol et al. (2006) for the region. Eq. (5.24) can be linearized as:

$$logA(f,r) = -blog(r) - \frac{\pi f}{vQ} rlog(e) \tag{5.26}$$

This linear system can be written in the form as in eq. (5.22). x is the solution vector contains the model parameters b_i and $m_i = \frac{\pi f}{vQ}$, b is a vector in the data space containing attenuation values and A is a matrix relating x to b. In order to estimate the quality factor, two approaches have been followed: the first one is to fit a straight line to the logarithm of the attenuation functions, assuming b=1 for body waves, to obtain $Q(f)$ from the slope (e.g., Castro et al., 1990). In the latter one, instead of using a predefined geometrical spreading function, Q and b values for a fixed frequency were decomposed, simultaneously (e.g., Bindi et al., 2006).

Because there is no enough data at the distance smaller than 10 km (see Fig. 5.3), $A(f,r)$ functions were normalized at 10 km for each fixed frequency. Figure 5.7 shows obtained Q and b values of T-, R- and V-component for the entire distance range. The frequency dependencies of Q values are $Q_T(f)$= 177.29(±12.34) $f^{\,0.65(\pm 0.04)}$ $Q_R(f)$=200.32(±18.21) $f^{\,0.63(\pm 0.06)}$ and $Q_V(f)$=166.99(±6.88) $f^{\,0.58(\pm 0.03)}$. Slight decrease in b values for the T-, R- and V-components was observed at the frequencies higher than 2 Hz.

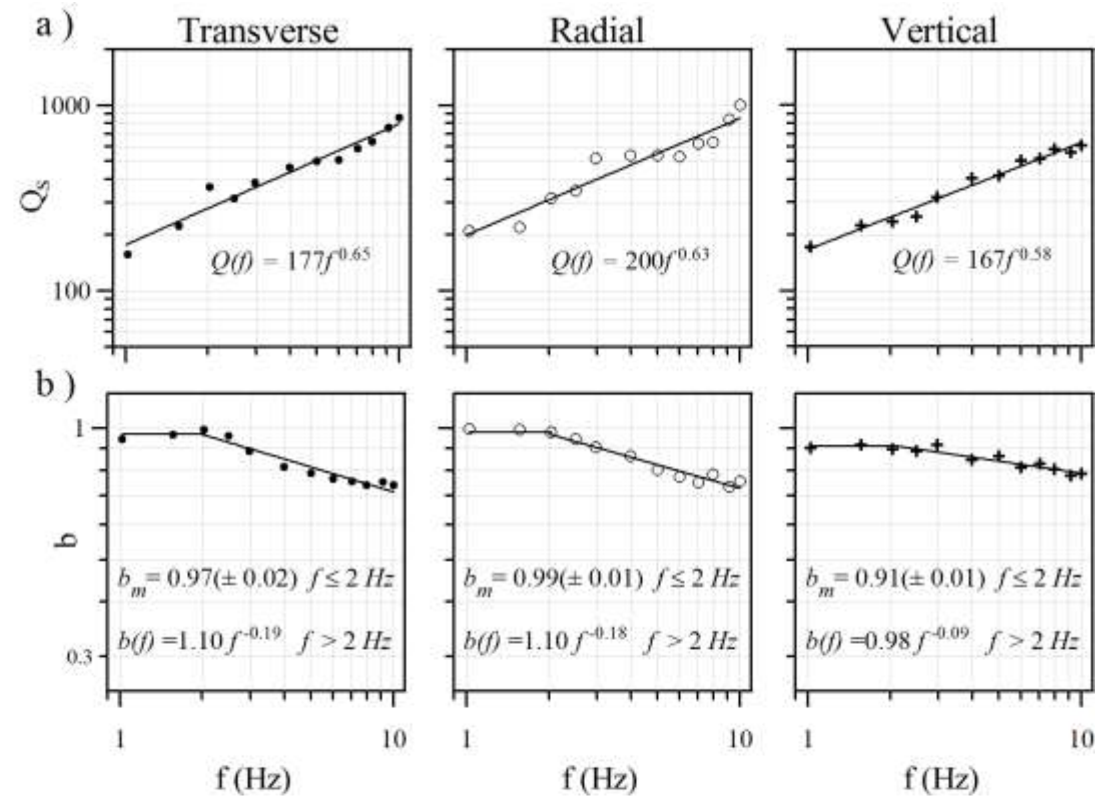

Figure 5.7 (a) Q and (b) b values versus frequency for the distance range between 10 and 200 km. Dots, circles and crosses represent Q and b values of T-, R- and V-component, respectively. b_m indicates the arithmetic mean of b values. Solid lines are the least-square fits of Q and b values. Note that, b values were modeled as piecewise linear fits.

Because of an apparent lack of attenuation between 70 and 120 km, Q and b estimates for short (10-70 km) and large (120-200 km) distance ranges were separately performed. Figure 5.8 shows Q estimates for the T-, R- and V-components for short and large distances. The frequency dependencies of Q are $Q_T(f)$ = 60.97(±7.92) $f^{\,1.42(\pm 0.08)}$, $Q_R(f)$ = 57.55(±6.51) $f^{\,1.46(\pm 0.07)}$ and $Q_V(f)$= 107.23(±8.99) $f^{\,0.94(\pm 0.05)}$ for short distances, and $Q_T(f)$ = 113.45(±7.81) $f^{\,0.47(\pm 0.04)}$, $Q_R(f)$ = 173.60(±11.29) $f^{\,0.28(\pm 0.04)}$ and $Q_V(f)$= 161.16(±13.15) $f^{\,0.34(\pm 0.05)}$ for large distances. The frequency dependencies of b values for two different distance ranges are given in Fig. 5.9. The arithmetic mean values of the T- and R-component b estimates are

0.88(±0.03) for short distances. This value is 0.89(±0.01) for V-component. The *b* estimates beyond 2 Hz have significant decrease with increasing frequency for long distances (Fig. 5.9b). RMS values of residuals associated with the second inversion step in eq. (5.26) are given in Fig. 5.10.

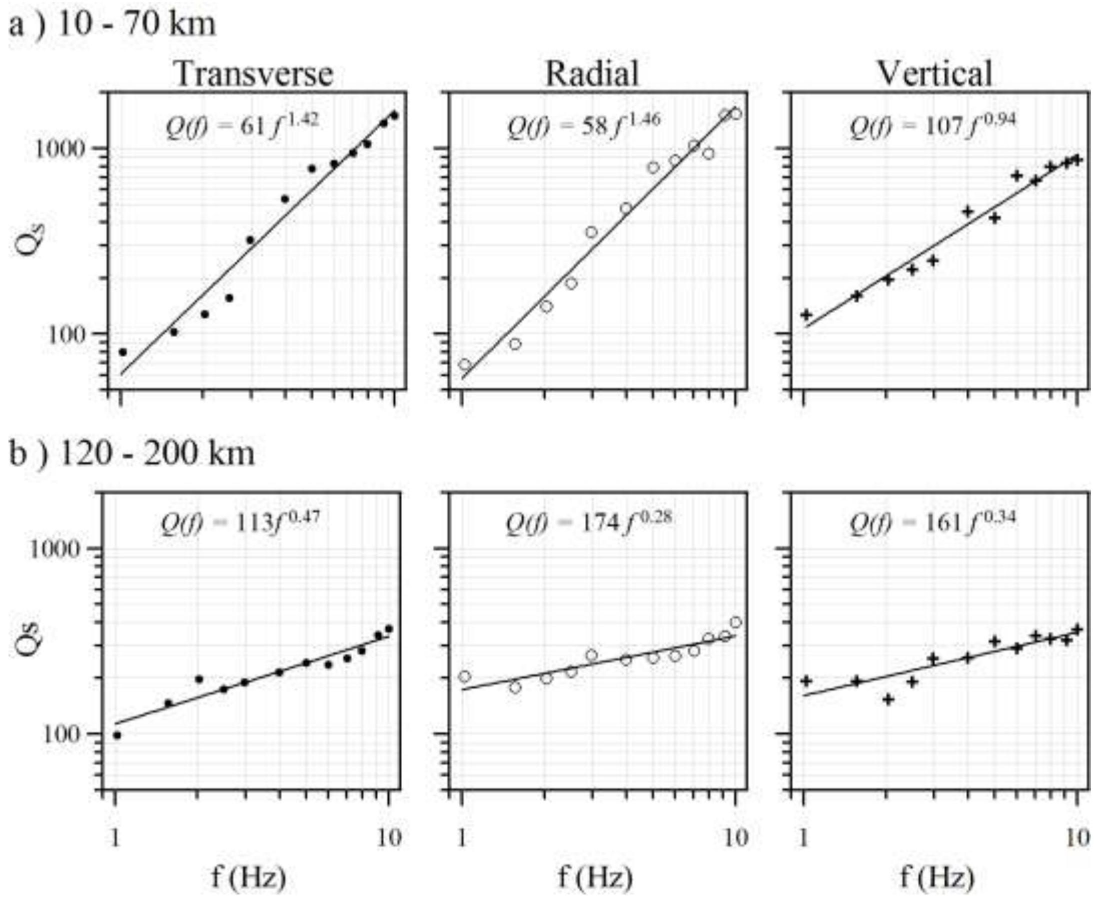

Figure 5.8 *Q* values for (a) short (10-70 km) and (b) large (120-200 km) distance ranges. Dots, circles and crosses represent *Q* values of T-, R- and V-component, respectively. Note that solid lines are the least-square fits of *Q* values.

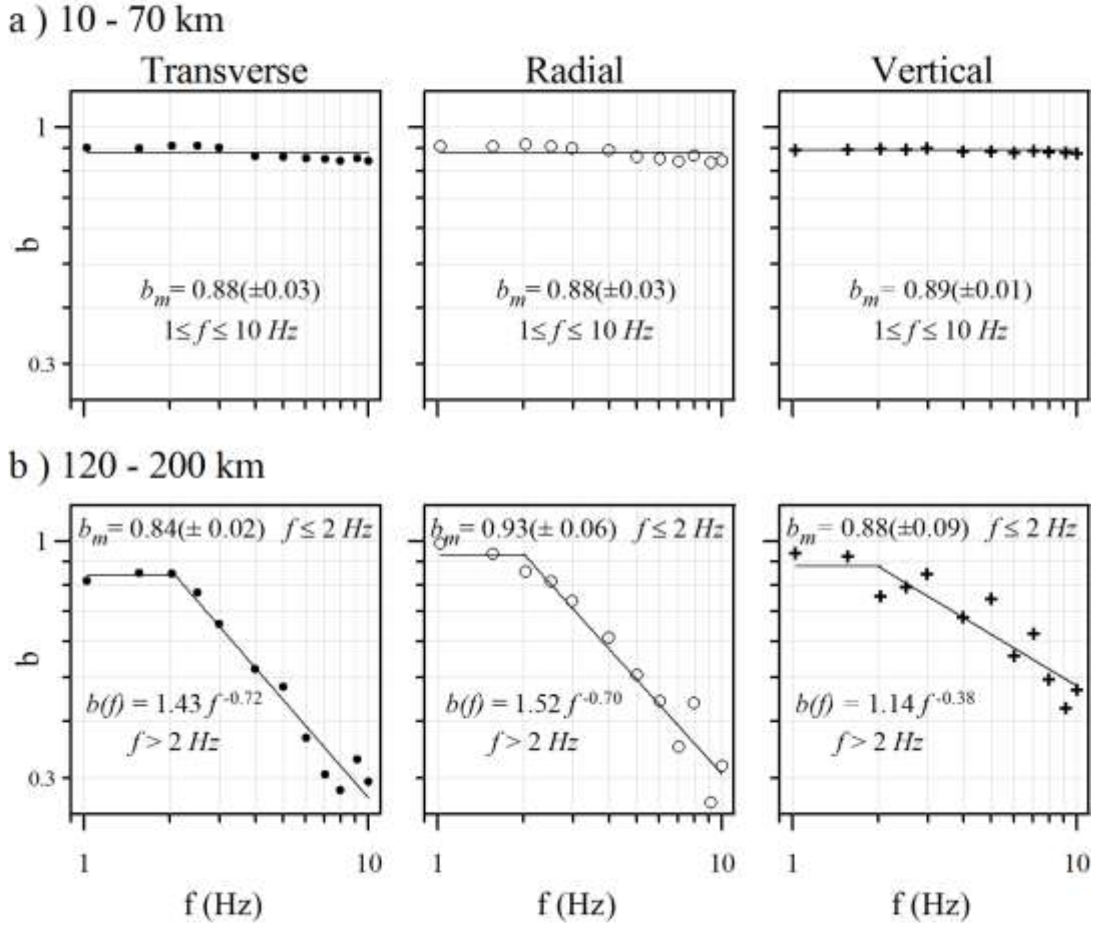

Figure 5.9 b values for (a) short (10-70 km) and (b) large (120-200 km) distance ranges. Dots, circles and crosses represent b values of T-, R- and V-components, respectively. b_m indicates the arithmetic mean of b values. Solid lines are the least-square fits of b values. Note that b values were modeled as piecewise linear fits for large distance range.

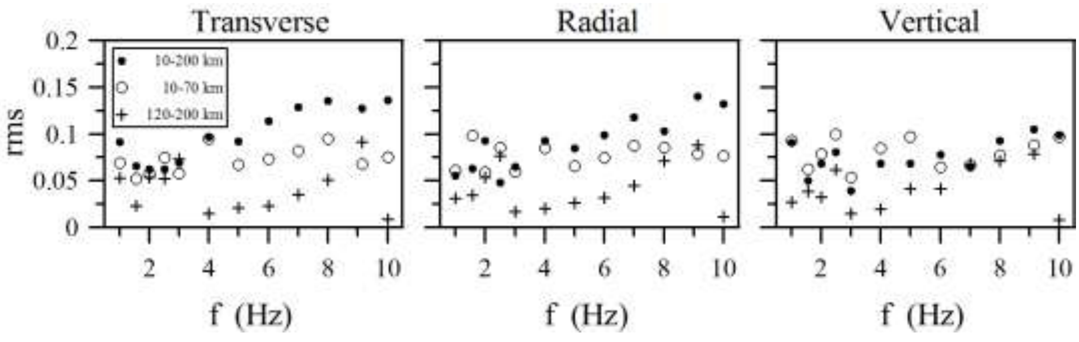

Figure 5.10 RMS values of residuals associated with eq. (5.26) and the results in Figs 5.7, 5.8 and 5.9. Dots, circles and crosses represent RMS values for the distance ranges of 10-200 km, 10-70 km and 120-200 km, respectively.

5.3.4 Separation of Source and Site Functions

After eliminating attenuation function effect, corrected spectral amplitudes can be inverted to decompose source and site spectral functions of micro- and moderate-size earthquakes in the central west Turkey:

$$U^{A}{}_{ij}(f) = \frac{U_{ij}(f,r)}{A(f,r)} = S_i(f) Z_j(f) \tag{5.27}$$

By taking the logarithm, the problem can be linearized and eq. (5.27) can be written for a fixed frequency *f* as following:

$$d_{ij} = s_i + z_j \tag{5.28}$$

Herein, $d_{ij} = \log U^{A}{}_{ij}(f)$ is the logarithm of the corrected spectral amplitude, $s_i = \log S_i(f)$ and $z_j = \log Z_j(f)$ are logarithmic source and site functions, respectively. This linear system can be written in matrix form just as in eq. (5.22) where *x* is the solution vector contains the model parameters S_i and Z_j, *b* is a vector in the data space containing attenuation corrected spectral amplitudes, and *A* is a matrix relating *x* to *b*. All calculations are carried out for 26 different frequencies for three components by using SVD algorithm. To overcome the linear dependence problem between the source and site terms (e.g., Andrews, 1986; Castro et al., 1990, 2003; Oth et al., 2009), either constrained-source or -site spectral function should be used. The following constraint has been used in this study:

$$\sum_{j=1}^{N} \log Z_j(f) = 0 \tag{5.29}$$

where *N* is equal to the number of reference site stations. Here, LA13, LA22 and MAN stations were chosen as reference sites according to the results of HVSR estimates in Chapter 4. GIT site functions from T-, R- and V-component are given in

Figs 5.11 and 5.12. Figure 5.13 shows examples from GIT spectral source function estimates for three components. RMS values of the residuals associated with the inversion results are given in Fig. 5.14.

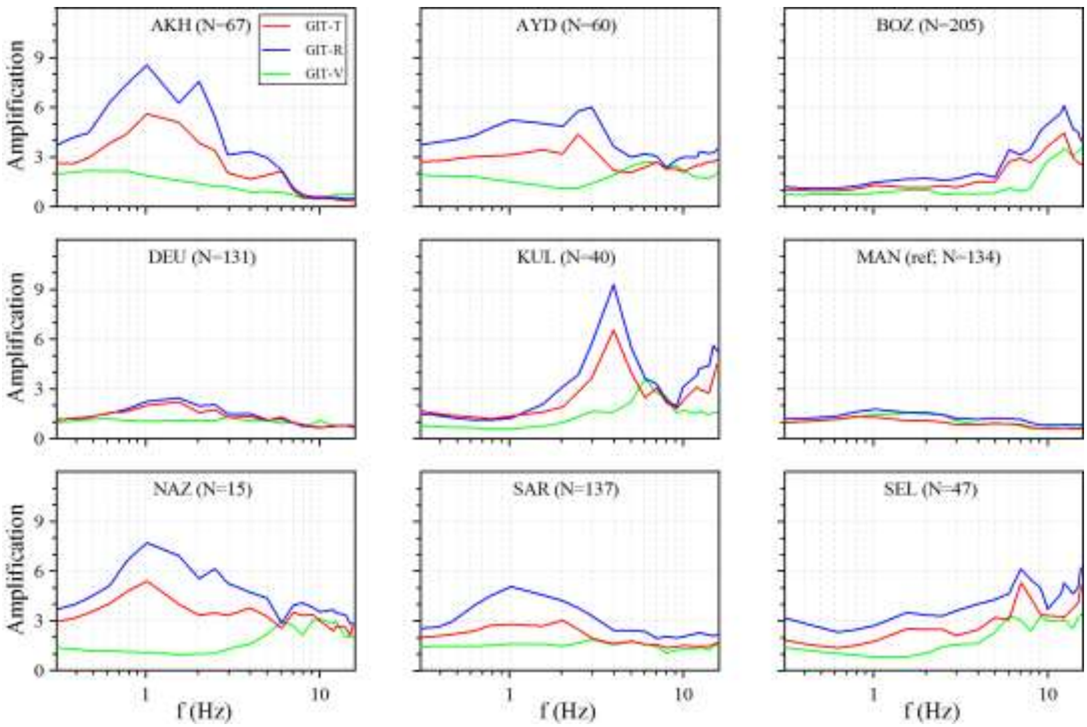

Figure 5.11 GIT site estimates from T-, R- and V- component for the regional array stations. *N* is the number of data used for each station.

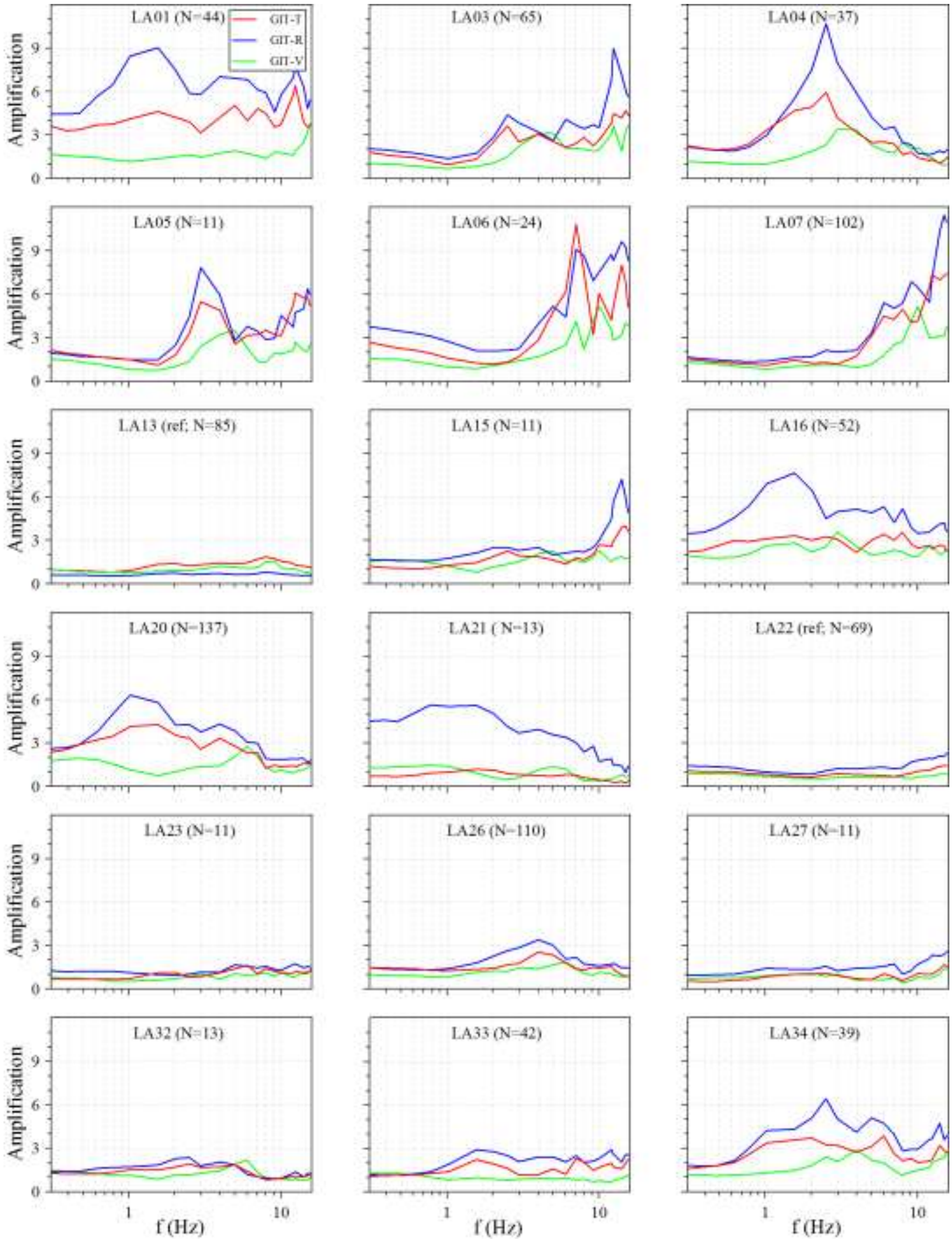

Figure 5.12 GIT site estimates from T-, R- and V- component for the linear array stations. *N* is the number of data used for each station.

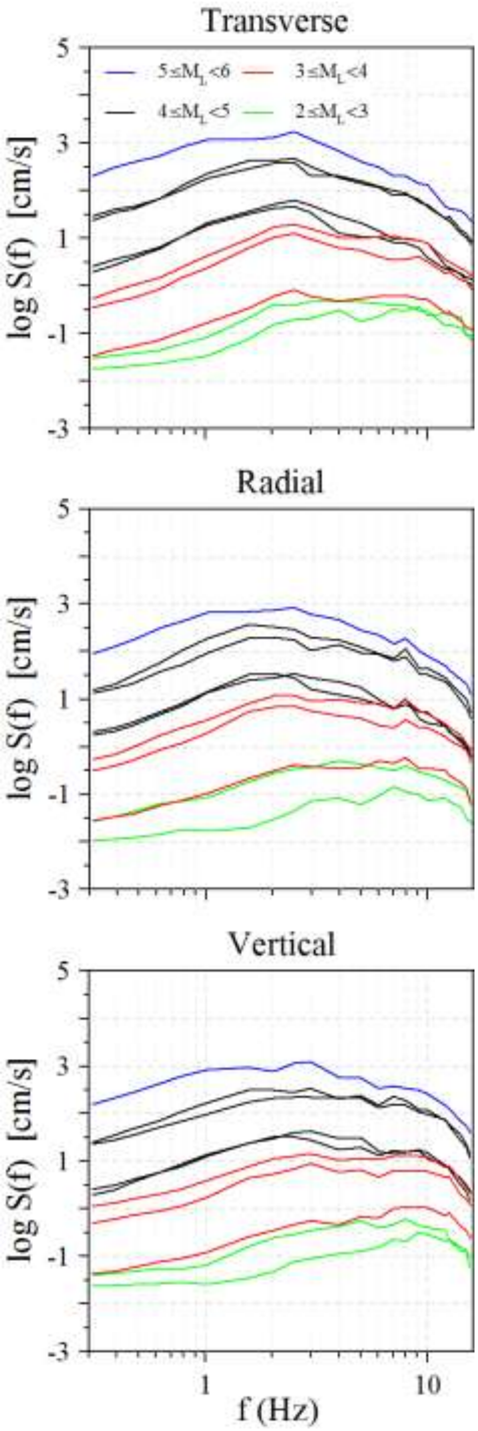

Figure 5.13 Examples from GIT source function estimates for three components of all-dataset.

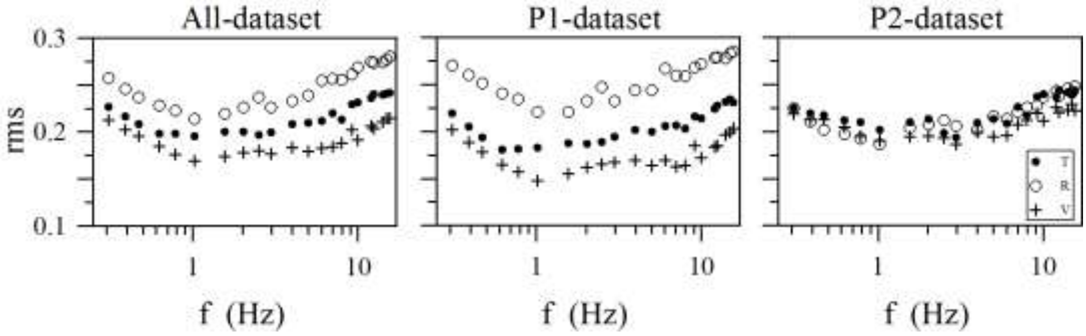

Figure 5.14 RMS values of the residuals associated with GIT for all-, P1- and P2-dataset. According to linear array positions of the data acquisition stage, the data were divided into two parts as mentioned below.

5.3.4.1 Data Distribution Effects on Source and Site Functions

According to linear array positions mentioned in Chapter 3, the data were divided into two parts in order to examine for data distribution effect on the results. The first stage consists of 1123 three-component-record of 190 earthquakes (P1-dataset). The second stage consists of 641 three-component-records of 132 events (P2-dataset). As shown in Fig. 5.15, P1- and P2-dataset dominantly come from different clusters (Zhu et al., 2006b) with different azimuthal distributions. GIT calculations separately performed to estimate spectral source and site functions of P1- and P2-dataset. LA13-MAN and LA22-MAN stations were chosen as reference sites for P1- and P2-dataset, respectively. Figure 5.16 shows comparison of GIT site functions from T-, R- and V-component of P1- and P2-dataset and for the stations deployed during whole data acquisition stage. Comparison of spectral source function estimates of all-, P1- and P2-dataset, from three components of the events with maximum (M_L = *2.0)* and minimum (M_L = *5.6*) magnitudes, is given in Fig. 5.17. Note that RMS values of the residuals associated with the inversion results of P1- and P2-dataset are also given in Fig. 5.14.

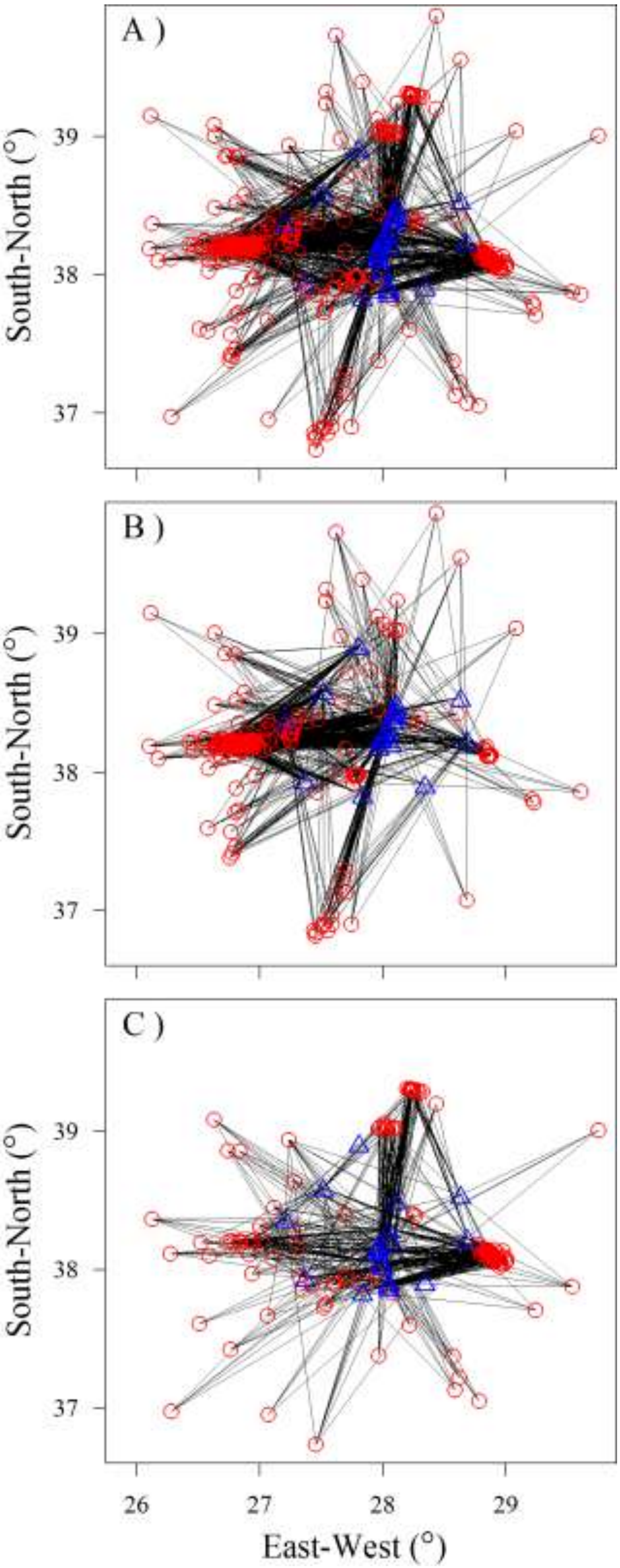

Figure 5.15 Ray coverages of all-, P1- and P2-dataset are given in A, B and C panels, respectively. Red circles and blue triangles represent the events and stations, respectively.

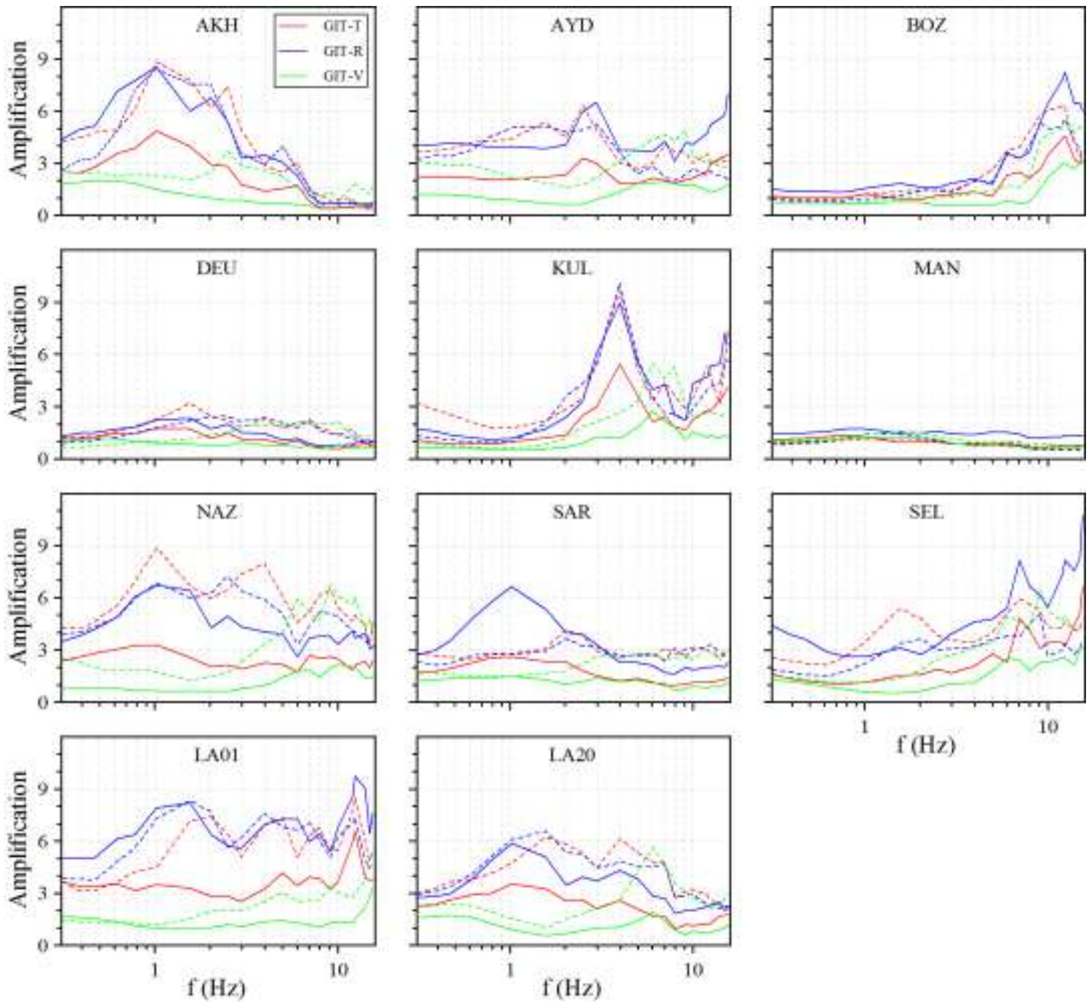

Figure 5.16 Comparison of GIT site functions from P1- and P2-dataset for the stations, deployed during whole data acquisition stage. Red, blue and green lines represent GIT site functions from T-, R- and V-component, respectively. Solid and dashed lines represent site functions from P1- and P2-dataset, respectively.

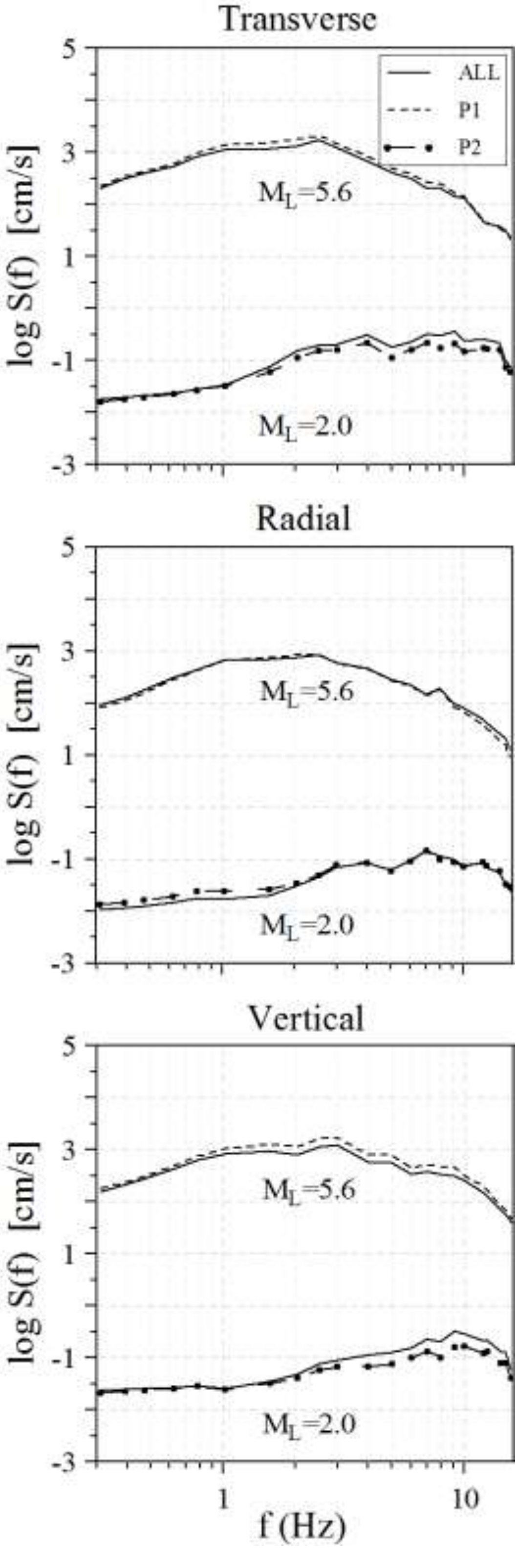

Figure 5.17 Spectral source function estimates for all-, P1- and P2-dataset from three components of the events with maximum (M_L = *2.0)* and minimum (M_L = *5.6*) magnitudes. Solid, dashed and dashed-dotted lines represent source functions from all-, P1- and P2-dataset, respectively.

5.4 Near-Surface Attenuation

It has been known that spectral amplitude of acceleration data decays rapidly at high frequencies (Ktenidou et al., 2013). Despite the attenuation along the path contains the average, the model in eq. (5.19) is inadequate to explain the attenuation of acceleration spectra at high frequencies. The amplitudes increase until a corner frequency, f_0, where the spectral shape is predicted by the omega-squared (ω^{-2}) model (Aki, 1967; Brune, 1970). Above f_0, some deviations from the ω^{-2} model occur and the spectral shape has differently been characterized. Originally, the parameter kappa (κ) to define the near-surface attenuation was introduced by Anderson & Hough (1984). This parameter describes the asymptotic high frequency slope of the spectra (Kilb et al., 2012). According to Anderson & Hough (1984), the spectrum exponentially decaying at high frequencies can be parameterized as following:

$$A(f) = A_0 e^{-\pi \kappa f} , \quad f > f_e \tag{5.30}$$

where A_0 is a source- and propagation path-dependent amplitude, κ is the spectral decay parameter which accounts for the attenuation along the path near the site; f_e is the frequency above which the spectral amplitude follows an exponential decay.

Because of its empirical nature, the debate on the origin and physical meaning of this parameter still continues (Ktenidou et al., 2013). Some researches correlate it to the seismic source, whereas the others are related to the site effects. Hanks (1982) and Petukhin & Irikura (2000) attributed this phenomenon mainly to local site effects. For instance, Anderson & Hough (1984) interpreted that κ was affected for amplitude reductions near the surface due to variations in the geologic conditions under the recording stations, and causes by high attenuation in the near-surface weathered layers. Some authors also have suggested an alternative model that it is a combination of near-surface attenuation and source effect (e.g., Purvance & Anderson, 2003; Tsai & Chen, 2000). Detailed discussion on taxonomy of kappa has been given by Ktenidou et al. (2013).

Anderson & Hough (1984) also observed linear dependence between κ and epicentral distance. They were expressed the behavior of κ as a function of epicentral distance in units of time as following:

$$\kappa(r) = \kappa_0 + \tilde{\kappa}(r) \tag{5.31}$$

in which r is epicentral distance. Therefore, the distance-dependence can be eliminated by extrapolating the $\tilde{\kappa}(r) = \frac{d\kappa}{dr} r$ trend to $r = 0$. A site-specific kappa, typically denoted as κ_0, is free of the regional Q attenuation effect. κ_0 corresponds to the site attenuation for a few kilometers depth beneath the station. $\tilde{\kappa}(r)$ states the distance dependence of κ and describes the incremental attenuation due to predominantly horizontal *S*-wave propagation through the crust (Ktenidou et al., 2013).

In this study, after eliminating attenuation function effects from spectral amplitudes, κ parameter has been calculated from T- component spectra of each recording utilizing eq. (5.30). The linear dependence between κ values and epicentral distances and also local magnitudes were examined. κ values as a function of epicentral distance and local magnitude for each station are given in Figs 5.18, 5.19, 5.20 and 5.21, respectively. Solid lines in these figures are linear least-square fits of κ values versus epicentral distances and local magnitudes. Standard error and significance level of these least-square fits together with average values of f_e and κ, and also obtained κ_0 values for each site can be seen in Table 5.1.

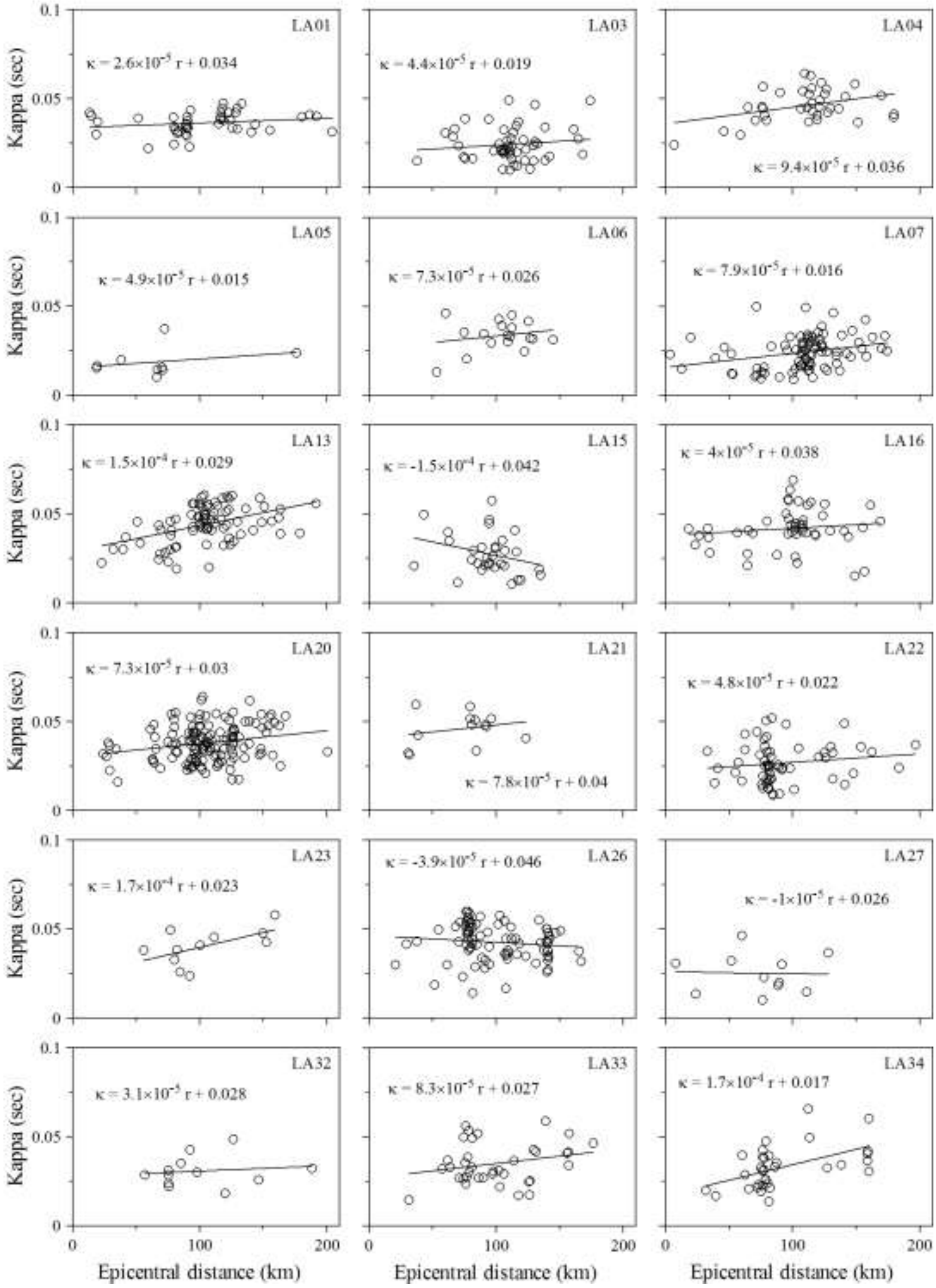

Figure 5.18 κ values versus epicentral distance for linear array station sites. Equations of linear least-square fits (solid lines) are given for each site.

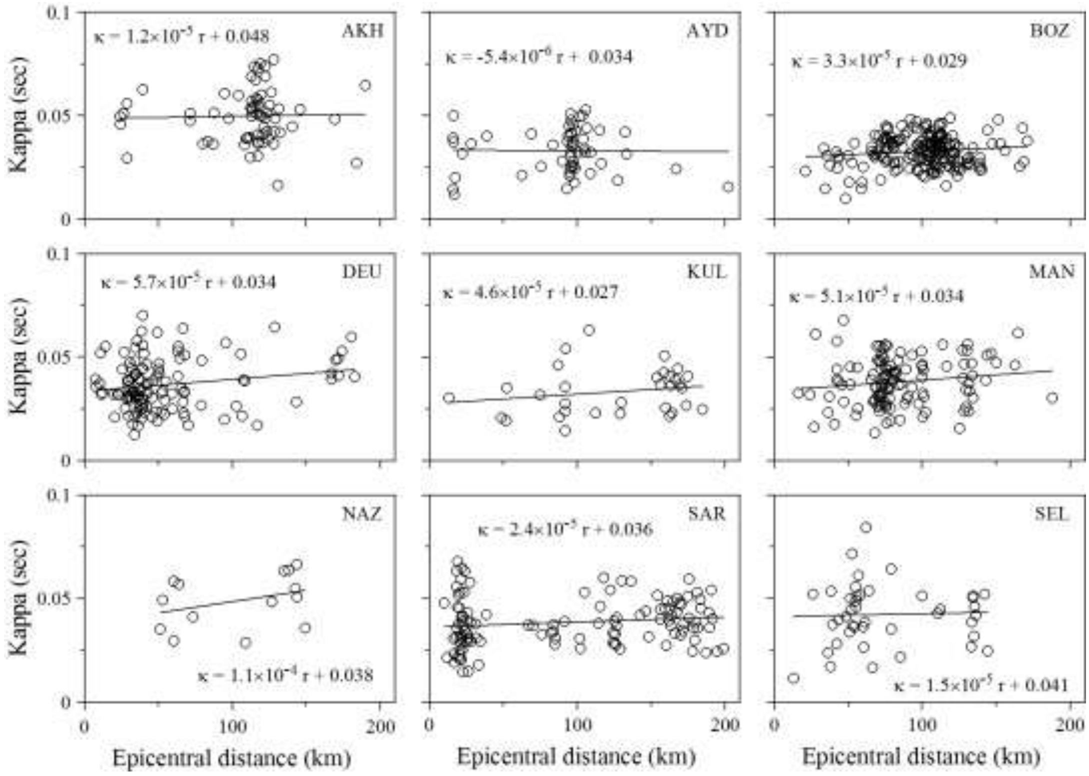

Figure 5.19 κ values versus epicentral distance for regional array station sites. Equations of linear least-square fits (solid lines) are given for each site.

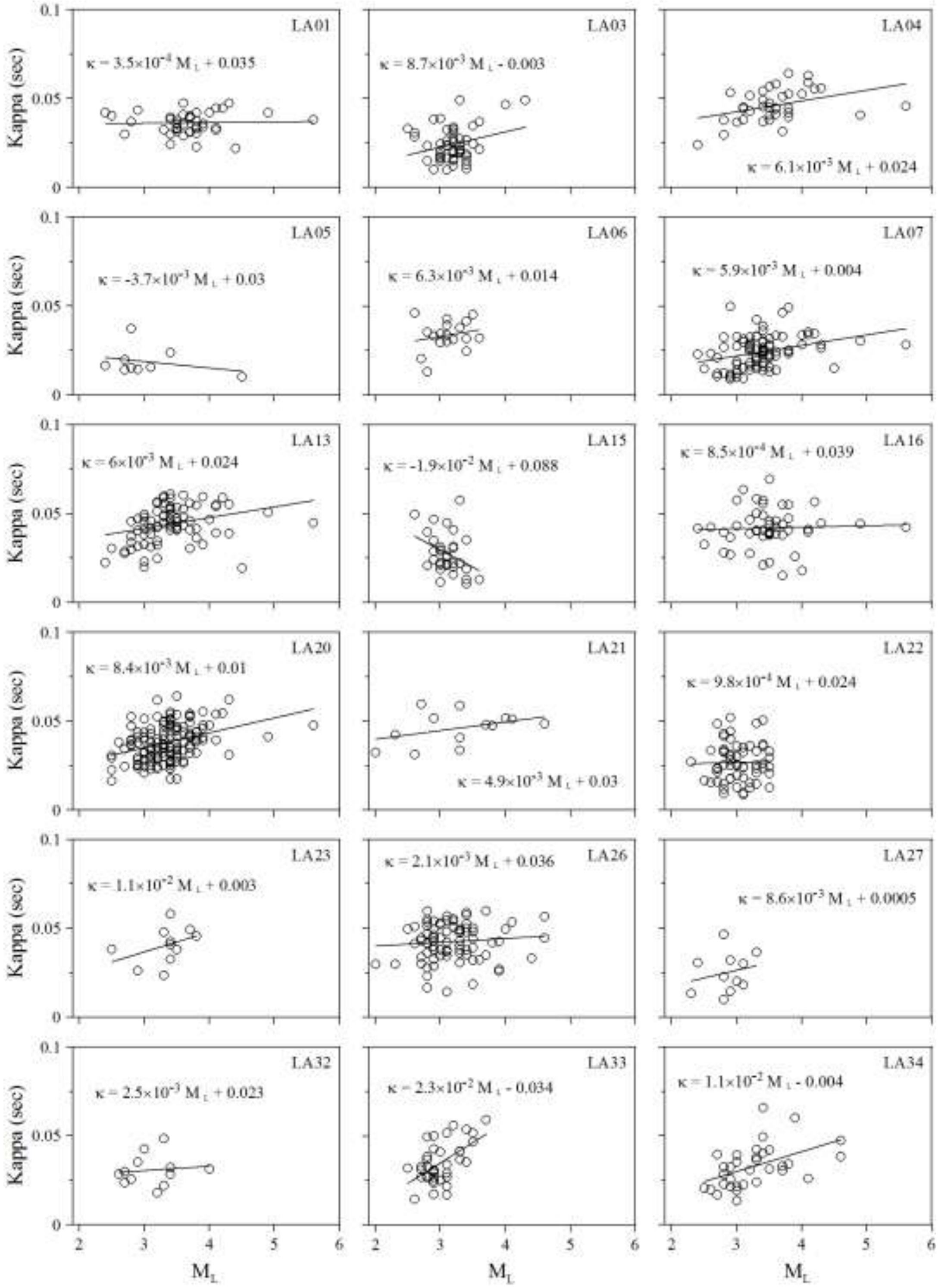

Figure 5.20 κ values versus local magnitudes-M_L for linear array station sites. Equations of linear least-square fits (solid lines) are given for each site.

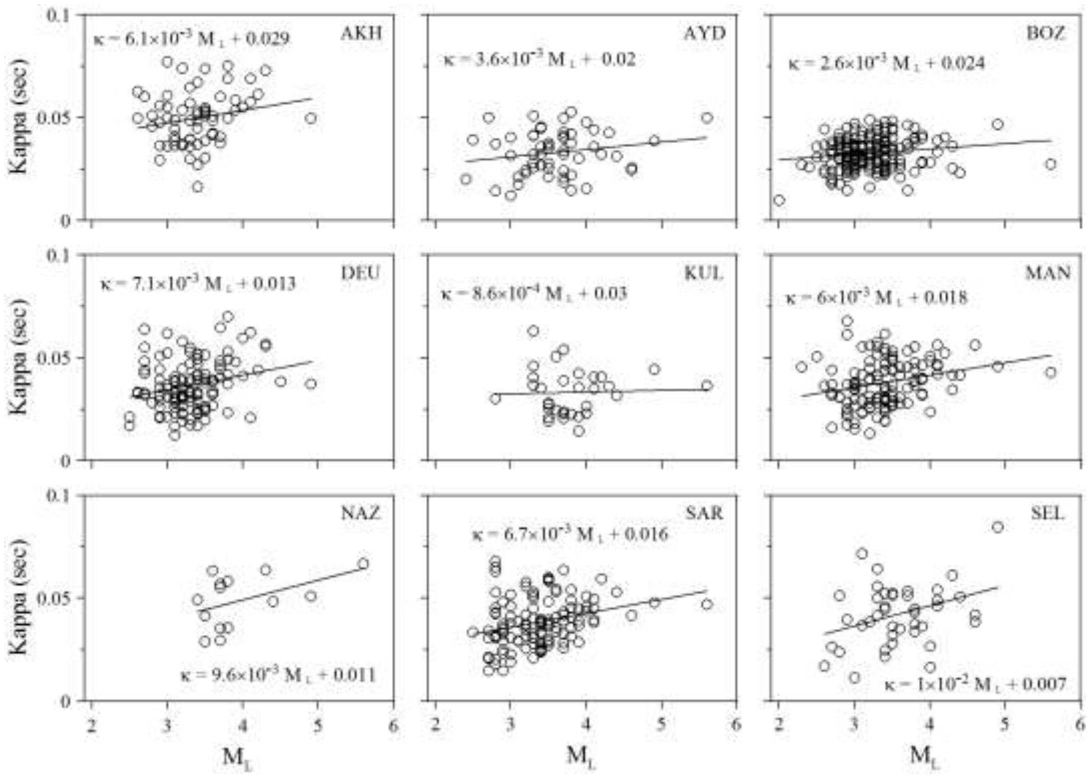

Figure 5.21 κ values versus local magnitudes-M_L for regional array station sites. Equations of linear least-square fits (solid lines) are given for each site.

Table 5.1 List of codes, site formation and obtained *fe*, κ and κ_0 values for each site. *SD*: Standart deviation, *SE:* Standart error, *SEF:* Standart error of fit and *SLF*: Significance level of fit from *F-Test*. * represents broadband stations.

Station Code	***Site Formation***	***Average fe (± SD)***	***Average κ (± SD)***	***κ_0 (± SE)***	***Distance***		***Magnitude***	
					SEF	***SLF***	***SEF***	***SLF***
LA01	Alluvium	5.98 *(±1.52)*	0.036 *(±0.006)*	0.034 *(±0.002)*	0.006	0.207	0.006	0.835
LA03	Neogene conglomerate	7.23 *(±1.86)*	0.024 *(±0.010)*	0.016 *(±0.006)*	0.010	0.388	0.009	0.047
LA04	Neogene conglomerate	6.23 *(±0.96)*	0.046 *(±0.009)*	0.036 *(±0.005)*	0.009	0.023	0.008	0.017
LA05	Micaschist	7.47 *(±1.34)*	0.019 *(±0.008)*	0.015 *(±0.005)*	0.008	0.455	0.008	0.457
LA06	Micaschist	7.51 *(±1.33)*	0.034 *(±0.008)*	0.026 *(±0.009)*	0.090	0.396	0.009	0.401
LA07	Micaschist	6.60 *(±1.42)*	0.024 *(±0.009)*	0.016 *(±0.003)*	0.009	0.007	0.009	0.002
LA13	Micaschist	7.80 *(±1.56)*	0.044 *(±0.010)*	0.029 *(±0.004)*	0.009	0.003	0.010	0.007
LA15	Micaschist	8.44 *(±1.45)*	0.028 *(±0.012)*	0.042 *(±0.009)*	0.011	0.105	0.011	0.044
LA16	Alluvium and micaschist	6.81 *(±1.77)*	0.042 *(±0.011)*	0.038 *(±0.005)*	0.011	0.379	0.011	0.774
LA20	Micaschist	4.88 *(±1.46)*	0.038 *(±0.010)*	0.030 *(±0.003)*	0.010	0.010	0.009	0.000
LA21	Micaschist	6.02 *(±1.50)*	0.046 *(±0.009)*	0.040 *(±0.007)*	0.009	0.424	0.009	0.177
LA22	Gneissic granite	8.07 *(±1.94)*	0.027 *(±0.011)*	0.022 *(±0.004)*	0.011	0.270	0.011	0.847
LA23	Gneissic granite	6.92 *(±2.18)*	0.040 *(±0.010)*	0.023 *(±0.009)*	0.009	0.064	0.010	0.228
LA26	Micaschist	7.44 *(±2.05)*	0.042 *(±0.010)*	0.046 *(±0.004)*	0.010	0.034	0.014	0.932
LA27	Micaschist	7.85 *(±2.06)*	0.025 *(±0.011)*	0.0259 *(±0.008)*	0.012	0.923	0.011	0.499
LA32	Sandstone	6.60 *(±2.22)*	0.031 *(±0.009)*	0.028 *(±0.008)*	0.009	0.676	0.009	0.718
LA33	Sandstone	8.20 *(±1.38)*	0.035 *(±0.011)*	0.027 *(±0.006)*	0.011	0.145	0.010	0.000
LA34	Sandstone and conglomerate	6.96 *(±1.56)*	0.033 *(±0.012)*	0.017 *(±0.005)*	0.010	0.002	0.011	0.004
AKH*	Alluvium	7.67 *(±1.46)*	0.050 *(±0.013)*	0.049 *(±0.006)*	0.013	0.805	0.013	0.103
AYD*	Alluvium	6.75 *(±1.90)*	0.033 *(±0.011)*	0.034 *(±0.004)*	0.011	0.892	0.010	0.151
BOZ*	Agricultural soil on top of the micaschist	8.70 *(±1.00)*	0.033 *(±0.007)*	0.029 *(±0.002)*	0.007	0.092	0.007	0.030
DEU*	Limestone	6.84 *(±1.86)*	0.037 *(±0.012)*	0.034 *(±0.002)*	0.012	0.039	0.012	0.007
KUL*	Agricultural soil on top of the micaschist	6.19 *(±1.89)*	0.032 *(±0.011)*	0.027 *(±0.006)*	0.011	0.290	0.011	0.830
MAN	Alluvium and colluvium	6.88 *(±1.75)*	0.038 *(±0.011)*	0.034 *(±0.003)*	0.011	0.123	0.011	0.005
NAZ	Alluvium	7.81 *(±2.04)*	0.049 *(±0.013)*	0.038 *(±0.010)*	0.013	0.229	0.012	0.092
SAR	Sandstone	7.43 *(±1.85)*	0.039 *(±0.012)*	0.036 *(±0.002)*	0.012	0.130	0.011	0.002
SEL	Alluvium	7.00 *(±1.60)*	0.042 *(±0.015)*	0.041 *(±0.005)*	0.015	0.813	0.014	0.023

CHAPTER SIX
GENERAL DISCUSSIONS

Site, source and regional/near-surface attenuation characteristics, which are necessary inputs for the seismic hazard assessment, were examined from recordings of micro- and moderate-size local earthquakes in the central west Turkey, by utilizing different approaches and the results were compared not only with each other but also with the literature. In the following sections, discussions on the obtained results are given in detail.

6.1 Site Functions from Spectral Ratio Estimates

The one of the main goal of this study is to highlight site-specific seismic hazard potential of basin/graben structures in the region. Firstly, site functions of 32 different locations were estimated by utilizing two different spectral ratio approaches (HVSR-Horizontal to Vertical Spectral Ratio and SSR-Standart Spectral Ratio). Comparison of average HVSR-T and HVSR-R estimates showed that the results are similar within a factor of 2 (Figs 4.2 and 4.3). Beyond the bounds of this factor, clear systematic differences were observed for LA03, LA06, LA13, LA21 and LA35 sites. The results show larger HVSR-R estimates for LA21 and LA35 sites (Figs 4.2 and 4.3). As shown in the geological cross-section in Fig. 3.2, these sites are located on the quaternary alluvium overlying steeply dipping bedrock region and the differences might be caused by basin-edge-generated waves (Narayan, 2005). On the other hand, there are limited number of data for these sites and large 90% confidence level interval for the averages. LA03, LA06 and LA13 located near the interface between different geologic units, too, which could be one of the possible reasons of these systematical differences.

One of the broadband stations, BOZ was deployed on Bozdağ Horst (Fig. 3.1). HVSR-T amplitude values for the BOZ site are 2.6, 3.4 and 4.3 at 2.7, 4.3 and 7.0 Hz, respectively (Fig. 4.2). During the N–S extension period major breakaway faults began to form around Bozdağ, located in the central part of the region (Yılmaz et al., 2000). Süzen et al. (2006) has investigated the origin and regional tectonic implications of high-altitude fluvial deposits developed over the Bozdağ horst which is an important structural element within the horst graben system of west Turkey. These deposits are of Quaternary age, which corresponds to the latest ~NS extensional tectonic phase in the region. The BOZ site is located on the steep slope of one of these fluvial cover regions on the metamorphics rocks. Obtained results imply that, even if the site is located on a horst, the presence of near-surface weathered zones must be evaluated carefully in site specific seismic hazard studies.

In order to investigate distance, magnitude and back-azimuth dependencies of the site functions from HVSR-T estimates for five linear and five regional array stations were examined (Figs 4.4, 4.5 and 4.6). Observed back-azimuth dependencies of the site functions are more significant than distance and magnitude dependencies. Back-azimuthal dependencies of LA13 site (Fig. 4.7) have implied that the origin of the systematical difference, between HVSR-T and HVSR-R site functions, is source radiation effect and it could be eliminated by averaging either all individual transverse and radial components HVSR estimates, in keeping with the literature, or by averaging each back-azimuthal group arithmetic mean HVSR values.

To evaluate site effect variations on the main horst-graben structures in the central west Turkey, transverse and radial components HVSR estimates were averaged and then distributions of HVSR-T, HVSR-R and averaged HVSR estimates were contoured as shown in Fig. 6.1. HVSR-T and HVSR-R estimates represent similar characteristics along the linear array stations. LA20 site is located on the quaternary alluvium in the middle of the Küçük Menderes Graben has large HVSR values for limited lower frequency band (~0.3–4 Hz). HVSR estimates of LA01, LA21 and LA35 sites show pronounced large values for almost whole frequency range interested. These sites are located on the quaternary alluvium close to basin-edges (Fig. 3.2). As pointed out by Cornou et al. (2003); sharp sediment-bedrock interface changes input motion frequency contents and causes large HVSR values.

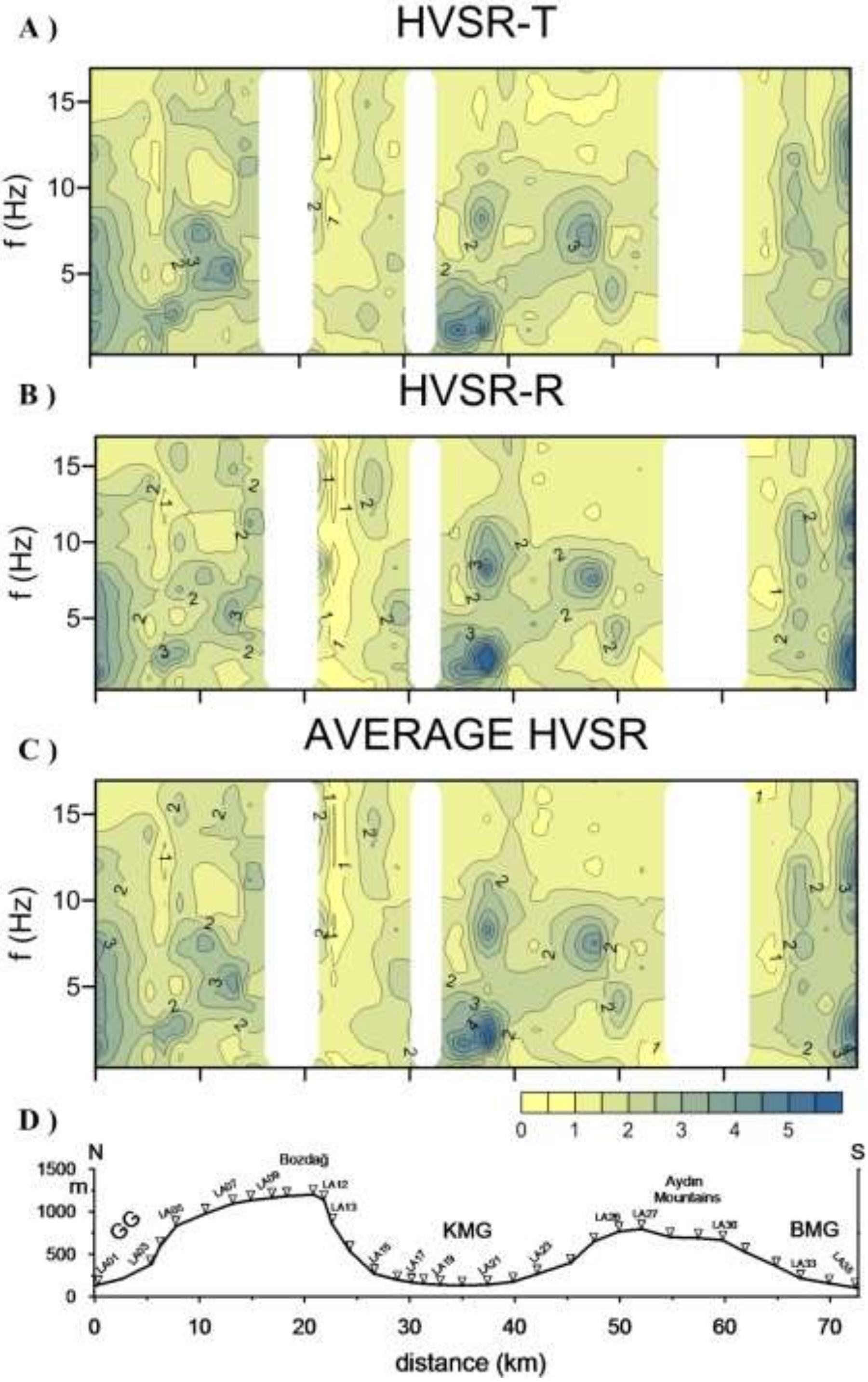

Figure 6.1 Distribution of HVSR estimates: A) HVSR-T, B) HVSR-R, C) average HVSR and D) the surface topography along the linear array amplified by a factor of 8. GG: Gediz graben; KMG: Küçük Menderes graben; BMG: Büyük Menderes graben. Blank areas on the maps represent stations without data.

Additionally, large HVSR values at the northern slope of the Bozdağ and Aydın Mountains Horsts (Figs 2.4 and 6.1) were observed in the medium frequency band (~2–8 Hz). These results might be attributed to tilted sedimentary or metamorphic rocks at the slopes of the horsts. The morphological, lithological, deformational characteristics of the deposits and the drainage system of the Bozdağ Horst suggest that the deposits are due to uplift and southward tilting of the Bozdağ horst (Süzen et al., 2006).

HVSR estimates (Figs 4.2 and 4.3) are also used in order to select reference station for SSR applications (Fig. 4.8). LA13 and LA22 sites were chosen as reference sites for SSR applications. Comparison of SSR and HVSR estimates from T-components were given in Fig. 6.2. Because of the reference site restrictions (epicentral distance range- and also epicentral distance at least four times larger than the distance- between reference site and the site of interest) SSR estimates could be obtained only for 8 stations. HVSR and SSR estimates for the stations LA01, LA16 and LA20 showed that SSR gives larger values at lower frequencies. LA01 is closely located on the quaternary alluvium overlying steeply dipping bedrock region of Gediz Graben. LA16 and LA20 are located on Küçük Menderes Graben which is small-size structure than the others (Fig. 3.1). The results imply that both the horizontal and vertical components of motion were affected by basin-generated waves in a similar way and their spectral ratio eliminates low-frequency band effects on HVSR estimates. The differences also indicate absence of low-frequency contents in the reference site spectra. The discrepancies between the results of two different spectral ratio estimates could be attributed to heterogeneity of the region such as lateral variations in regional velocity and attenuation values (Bindi et al., 2009) caused by basin geometry and edge effects. Parolai & Richwalski (2004) has indicated that the two techniques should provide similar results independent of the time window length, if the medium is predominantly one-dimensional. In the case of Parkway valley, Chavez-Garcia et al. (1999) concluded that it was not possible to separate 1D and 2D/3D effects because of their contribution to the same frequency band. By using teleseismic events data, Cornou et al. (2003) had suggested that HVSR is not sensitive or is much less sensitive to basin-induced waves than SSR technique by assuming that basin-induced waves are related to 2D/3D effects. They pointed out the importance of sediment-bedrock interface and structure geometry which control frequency input motion in shaping wave fields. Numerical simulations performed by Qin et al. (2012) demonstrated that 3D basin geometry causes a wavefront focusing effect that contributes significantly to a localized strong amplification.

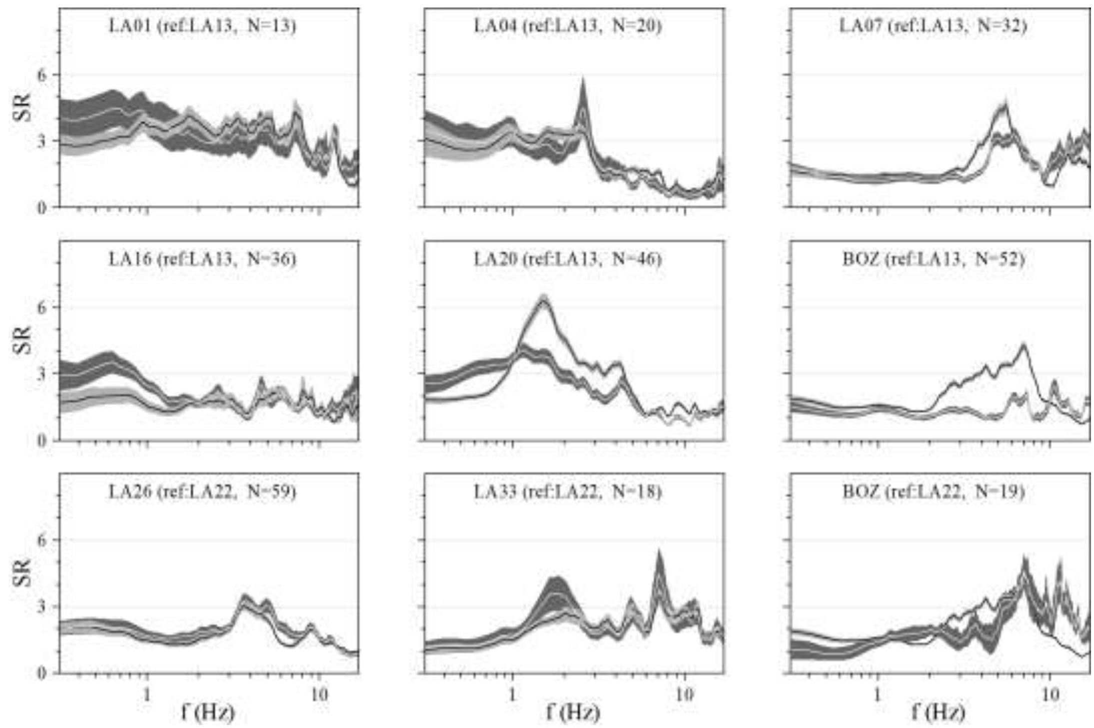

Figure 6.2 The average HVSR and SSR results from T-component for 8 sites with 90% confidence interval from *t*-test. Black and white lines represent HVSR and SSR estimates, respectively. *ref*: reference site and *N*: number of data used for each station for SSR. Note that, SSR results for the BOZ site were estimated by utilizing both of the chosen reference sites.

As shown in Fig. 6.2, the average site function of chosen reference sites could cause discrepancies between the results as shown the SSR results for BOZ site. The SSR results for the BOZ site were estimated by utilizing both of the chosen reference sites. The distance between the BOZ and LA13 sites is about 2.5 km, while it is about 19.5 km between the BOZ and LA22 sites. The obtained SSR results for the BOZ site imply that the LA13 and BOZ sites affect transverse horizontal ground motion in a similar way, except for higher frequencies. Site functions obtained by the SSR method can be misleading in inferring true site transfer functions especially for high frequencies, since most of the reference site transfer functions showed large variability at high frequencies due to shallow heterogeneities resulting from varying degrees of weathering (Malagnini et al., 2004). The effect of distance, and also heterogeneity of the medium, between the sites, as well a high degree of fracturing (Fig. 3.2), are observed in the SSR results of the BOZ site with regard to reference site LA22.

6.2 Regional Attenuation Parameters (*Q* and *b*) from GIT

The general characteristics of the empirical attenuation functions that obtained for the entire distance range are shown in Figs 5.4 and 5.5. The slope of the decay is significant for short (10–70 km) and large (120–200 km) distance ranges. An apparent lack of attenuation between 70 and 120 km might be originated from the lower crustal/Moho reflections such as the contribution of the *SmS* phases (e.g., Akıncı et al., 2006; Atkinson & Mereu, 1992). Boztepe-Güney & Horasan (2002) and Bindi et al. (2006) interpreted similar observations as a characteristic feature of crustal propagation in northwestern Turkey caused by critical Moho reflections, although the hinge points of obtained curves are unique to the crustal attenuation and velocity structure of the region of interest. According to Yang et al. (2007), the character of attenuation functions typically changes where the near-critical Moho reflections disrupt the uniform-space approximations. Figure 5.5 compares the non-parametric attenuation function estimates of T-, R- and V- component results for 12 frequencies. Larger V-component attenuation values for small frequencies ($f \leq 2.0$ Hz) were obtained. On the other hand, V-component attenuation functions are smaller than the other components at the frequencies larger than 3 Hz for the distances greater than 50 km, whereas there are the slight differences in the amount of attenuation between T-, and R- components, especially for high frequencies. These slight differences might be associated to near-surface fluid saturated sediments or cracks. On the other hand, these small differences are within the statistical uncertainties of the estimates (Fig. 5.6).

Firstly, Q and b values were parameterized for the distance range between 10 and 200 km. Obtained frequency dependencies of Q values are $Q_T(f)= 177.29(\pm 12.34)\ f^{\ 0.65(\pm 0.04)}$ $Q_R(f)=200.32(\pm 18.21)\ f^{\ 0.63(\pm 0.06)}$ and $Q_V(f)=166.99(\pm 6.88)\ f^{\ 0.58(\pm 0.03)}$ (Fig. 5.7). An average Q of T- and R- components is $Q(f)=189.63(\pm 13.50)\ f^{\ 0.64(\pm 0.05)}$. High frequency dependence of Q values has been reported for tectonically active regions in Turkey (e.g., Akıncı et al., 1994; Akıncı & Eyidoğan, 1996; Cong & Mitchell, 1998; Horasan et al., 1998; Horasan & Boztepe-Güney, 2004). Low Q_o values could be related to possible mid-crustal low-velocity layer previously mentioned for the region (Akyol et al., 2006; Gürer & Bayrak, 2007; Saunders et al., 1998). Zor et al. (2007) obtained low Lg Q_o values for the eastern Anatolian Plateau (~70–100) and for the Menderes Massif (~60–150) in western Turkey. For the eastern Anatolian Plateau, they related these results with localized mid-crustal low-velocity zones (Zor et al., 2003), which might be an indication of partial melt in the crust. Similarly, low Lg Q_o values along the Menderes massif were associated with the partially molten crust and young volcanism by Şahin et al. (2013).

The exponent b changes from 1.0 to 0.7 with increasing frequency for the entire distance range (Fig. 5.7). However, F-test statistics reveal that there are no statistically meaningful linear trends between the exponent b values in whole frequency range of interest. For that reason, $b(f)$ values for two different frequency ranges were parameterized as: an average value of b=0.97(±0.02) for $f \leq 2$ Hz; $b(f)=1.10(\pm 0.03)\ f^{\ -0.19(\pm 0.02)}$ for $f > 2$Hz for T-component; an average value of b=0.99 (±0.01) for $f \leq 2$ Hz; $b(f)$ =1.10(±0.03)$\text{f}^{-0.18(\pm 0.01})$ for $f > 2$ Hz for R-component; an average value of b=0.91(±0.01) for $f \leq 2$ Hz; $b(f)$ = 0.98(±0.02) $\text{f}^{-0.09(\pm 0.01})$ for $f > 2$ Hz for V-component. Slight decrease in b beyond 2 Hz could be attributed to constructive interference of high-frequency waves.

Due to an apparent lack of attenuation between 70 and 120 km, Q and b values parameterizations were performed for short (10-70 km) and large (120-200 km) distance ranges, separately. Figure 5.8 shows Q estimates for short and large distances. The frequency dependencies of T-, R- and V-component Q are $Q_T(f)$ = $60.97(\pm 7.92)\ f^{\ 1.42(\pm 0.08)}$, $Q_R(f)$ = $57.55(\pm 6.51)\ f^{\ 1.46(\pm 0.07)}$ and $Q_V(f)$= 107.23(±8.99) f

$^{0.94(\pm0.05)}$ for short distances; and $Q_T(f)$ = 113.45(±7.81) f $^{0.47(\pm0.04)}$, $Q_R(f)$ = 173.60(±11.29) f $^{0.28(\pm0.04)}$ and $Q_V(f)$= 161.16(±13.15) f $^{0.34(\pm0.05)}$ for large distances. The *Q*-frequency dependence for large distance range is lower than the one obtained for short distances. These results indicate that *S* phases recorded at long distance range propagate through more homogenous deeper media. Controversially, stronger frequency dependence of *Q* at short distance range underlines the heterogeneity which could be associated to high degree of fracturing (e.g., Akyol et al., 2006; Çiftçi et al., 2010), extensive volcanism (e.g., Aldanmaz, 2006; Tokçaer et al., 2005) and fluid filled cracks/geothermal systems (e.g., Mutlu, 2007; Tarcan et al., 2000) in the crust. Akıncı et al. (1995b) separated the effects of intrinsic and scattering attenuation in western Turkey using a Multiple-Lapse Time Window Method. They showed that scattering (Q_s^{-1}) predominates over intrinsic Q^{-1} at low frequencies (1–4 Hz) for short hypocentral ranges (0–80 km) and intrinsic attenuation is dominant over scattering attenuation in all frequency bands for long hypocentral distances (80–170 km). Individual grabens in the region are composite basins and comprise multiple depocentres or subbasins with sediment thickness exceeding 3000 m in some locations and crossed by complicated fault systems (Çiftçi et al., 2010). This kind of structure near the surface could be responsible for the scattering attenuation in the region (Akıncı et al., 1995b). Low Q_o for large distances could indicate increasing density and velocities with depth. Briefly, low Q_0 values and larger frequency dependence for short (10-70 km) distance ranges could be related to a high degree of fracturing, fluid filled cracks, young volcanism and geothermal activity in the crust. Decreasing *Q* frequency dependence and increasing Q_0 values for large (120-200 km) distance ranges manifest more homogenous medium by increasing pressure and enhanced healing of cracks with increasing temperature with depth. Different Q_o and *n* values, especially for large distance ranges, may indicate *Q* anisotropy for deeper phases which could be associated to plastic flow at greater depth (Mitchell & Xie, 1994).

Figure 5.9 compares the *b* estimates of all components at two different distance ranges. At short distances *b* is approximately 0.9 (Fig. 5.9a) for three components. Thus, for the 10–70 km range an average value of *b* seems adequate for the region within the frequency band of interest (1–10 Hz). The estimates of b decrease significantly with increasing frequency in the 120–200 km distance range (Fig. 5.9b). Castro et al. (2009) has observed a similar behavior of the geometrical spreading exponent in the Sonora Basin and Range for the 40–80 km range, for both P and S waves. F-test statistics reveal that there are no statistically meaningful linear trends between exponent b values in whole frequency range of interest. For that reason, b values were parameterized as piecewise linear fits for large distance range: an average value of b=0.84(±0.02) for $f \leq 2$ Hz; $b(f)=1.43(\pm 0.11)\, f^{-0.72(\pm 0.06)}$ for $f > 2$ Hz for T-component; an average value of b=0.93(±0.06) for $f \leq 2$ Hz; $b(f) = 1.52(\pm 0.12)\, f^{-0.70(\pm 0.07)}$ for $f > 2$ Hz for R-component; and an average value of b=0.88(±0.09) for $f \leq 2$ Hz; $b(f)=1.14(\pm 0.11)\, f^{-0.38(\pm 0.07)}$ for $f > 2$ Hz for V-component. Decrease in b beyond 2 Hz for large distances could be explained by constructive interference of high-frequency refracted and reflected waves generated by geological complexity. In addition, the geometrical spreading probably starts having smaller effect on the amplitude decay because of surface wave arrivals at this long distance range.

Morozov (2010) showed that geometrical spreading is far from any of the theoretical ‘spreading-wave front’ models and contains pervasive ‘multipathing’ represented by multiple reflections and mode conversions because of the wavefields generated by complex crustal and mantle structure. Recent studies of body-wave attenuation for seismically active areas in the different parts of the world show that the value of the geometrical spreading coefficient associated with the distance may be more complicated than a simple assumption of b=1, because of the complex velocity structure of the media. For instance, Castro et al. (2008b) modeled upper and lower crust total Q in the southern region of Italy. They investigated frequency dependence of geometrical spreading coefficient for lower crust and obtained that the geometrical spreading varies between $r^{-0.3}$ and $r^{-0.5}$.

6.2.1 Comparison with Other Attenuation Functions

Obtained $Q(f)$ function for entire distance range was compared with the results for western Turkey and for different regions from all over the world in Fig. 6.3. Obtained average T- and R- component $Q(f)$ estimates, $Q_S(f)$=190±13.5 $f^{\,0.64\pm0.05}$, is given in this figure. Detail about compared $Q(f)$ values are given below:

1) Utilizing the single isotropic scattering model in western Turkey, Akıncı et al. (1994) obtained $Q_c(f)$ =50.7$f^{\,1.01}$ and $Q_c(f)$=183.2$f^{\,0.76}$ for a lapse time of 30 and 190 s, respectively. Their data set consists of 116 local earthquakes with magnitudes ranging from 3.0 to 4.0 and recorded by a three-component short-period station. Hypocentral distances of their data range between 10 and 400 km. More than the central west Turkey, their data came from northwestern Turkey. Figure 6.3a includes their Q_c estimates for a lapse time of 30 s.

2) Based on the *S*-wave to coda wave amplitude ratio with distance, Horasan & Boztepe-Güney (2004) computed Q_S values of the crust in the Sea of Marmara for a lapse time 50 s. They used the data from 91 earthquakes with duration magnitudes between 2.4 and 3.9 and focal depths less than 20 km, recorded by three stations. The epicenter distances of the selected earthquakes range from 15 to 70 km. They estimated Q_S values for five sub-regions. An average of their estimates, 40±5 $f^{\,1.03\pm0.06}$ was given in Fig. 6.3a.

3) Akıncı et al. (2006) computed $Q_S(f)$=180 $f^{\,0.45}$ (Fig. 6.3a) in the frequency range of 0.4-15.0 Hz and in the distance range of 10-200 km for the Marmara region, Turkey. Their data set consists of 24000 three-component recordings by 53 stations and from 462 earthquakes with moment magnitude range between 2.5 and 7.2. They parameterized geometrical spreading coefficients for four different distance ranges at two different frequency ranges (f < 1 Hz and $f \geq$ 1 Hz).

4) Şahin et al. (2007) estimated intrinsic and scattering seismic attenuation in southwestern Anatolia by using coda-*Q* and the Multiple Lapse Time Window methods. Their data set consists of 116 events, with magnitude range of 3.0-5.6 and epicentral distance range of 20-180 km, recorded by a three-component broadband station. They obtained intrinsic, scattering, total, observed and expected coda Q values. Intrinsic; $Q_i(f)$=111 $f^{\ 1.17}$ and observed coda; $Q_C(f)$=125 $f^{\ 0.84}$ estimates from their results are given in Fig. 6.3a.

5) Akıncı et al. (2013) scaled ground motions in the frequency range of 0.25-10 Hz for western Turkey. Their data set contains our study area and data set as a subset. This dataset consists of 902 regional earthquakes of magnitude 2.5 to 5.8 and the distance range of 15-250 km. They obtained anelastic attenuation function $Q_S(f)$=180 $f^{\ 0.55}$ (Fig. 6.3a) with a piecewise geometrical spreading coefficient (1.0 for 1< r < 20 km; 0.8 for 20 < r < 40 km; 0.7 for 40 < r < 100 km; and 0.5 for r > 100 km) for the region.

6) Castro et al. (1999) obtained the frequency dependence of Q as $Q_{SV}(f)$=105.6 $f^{\ 0.65}$ and $Q_{SH}(f)$=86.1 $f^{\ 0.70}$ for the region of Marche, Italy. In Fig. 6.3b, the average $Q_S(f)$ function of their $Q_{SV}(f)$ and $Q_{SH}(f)$ estimates was given. They used 161 three-component digital records from 26 events having magnitudes in the range of 1.8 < M < 3.6 at hypocentral distances between 9 and 125 km. They investigated the frequency dependence of geometrical spreading values and gave the averages of them for *P*, *SV* and *SH* waves.

7) Malagnini et al. (2002) computed $Q_S(f)$=260 $f^{\ 0.55}$ (Fig. 6.3b) in the frequency range of 0.5-14.0 Hz together with a slightly frequency-dependent geometrical spreading for northeastern Italy. Their dataset is from 1753 earthquakes with magnitudes ranging from 1 to 5.6 and well distributed out to 200 km hypocentral distance. They parameterized geometrical spreading coefficients for five different distance ranges at two different frequency ranges ($f \leq 1$ Hz and $f > 1$ Hz).

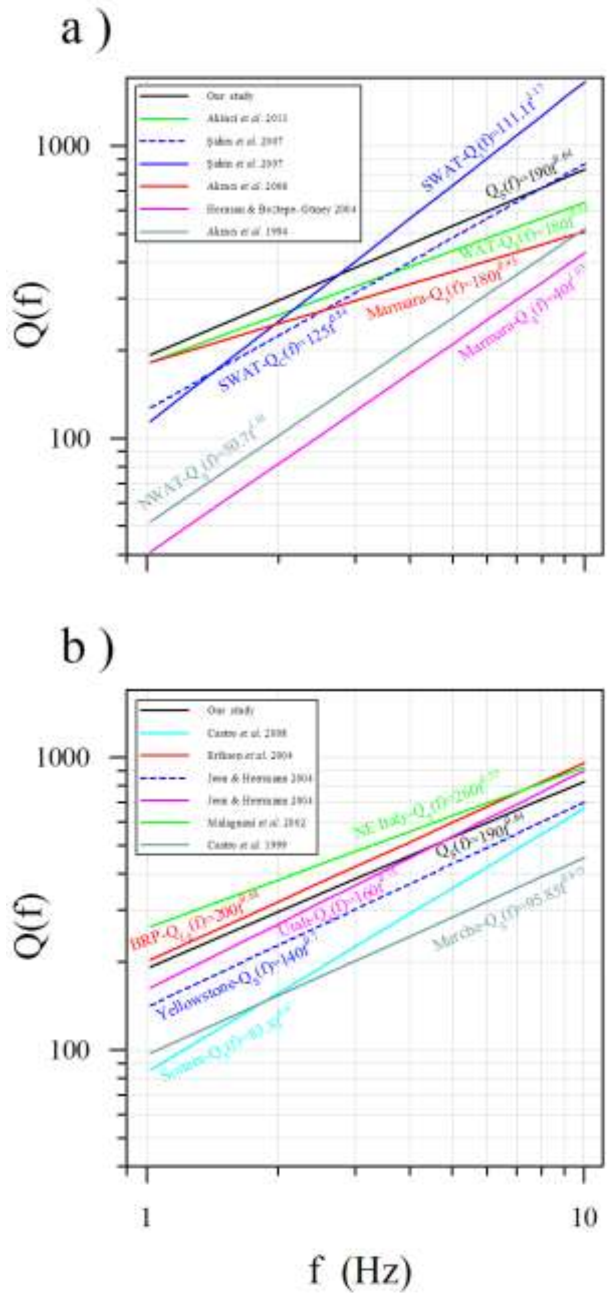

Figure 6.3 An average *Q(f)* results (black line) for entire distance range (10-200 km) from this study compared to results from numerous regions (a) for vicinity of western Turkey: NWAT- $Q_S(f)$ (North Western Anatolia-Turkey; Akıncı et al., 1994), Marmara- $Q_S(f)$ (The Marmara Region-Turkey; Horasan & Boztepe-Güney, 2004 and Akıncı et al., 2006), SWAT- $Q_i(f)$ and SWAT- $Q_C(f)$ (South Western Anatolia-Turkey; Şahin et al., 2007), WAT- $Q_S(f)$ (Western Anatolia-Turkey; Akıncı et al., 2013). (b) for different regions from all over the world: Marche-$Q_S(f)$ (Marche-Italy; Castro et al., 1999), NE Italy-$Q_S(f)$ (North East-Italy; Malagnini et al., 2002), BRP-$Q_{Lg}(f)$ (Basin and Range Province-USA; Erickson et al., 2004), Utah and Yellowstone-$Q_S(f)$ (USA; Jeon & Herrmann, 2004), Sonora-$Q_S(f)$ (Northeastern Sonora-Mexico; Castro et al., 2008c).

8) Jeon & Herrmann (2004) estimated the anelastic attenuation functions $Q_S(f)=160\, f^{0.75}$ with a piecewise geometrical spreading coefficient (1.2 for $0< r \leq 50$ km; 0.55 for $50 \leq r \leq 60$ km; 0.2 for $60 \leq r \leq 90$ km; 0.1 for $90 \leq r \leq 140$ km and 0.5 for $140 < r \leq 500$ km) for Utah (Basin and Range Province). They also obtained $Q_S(f)=140f^{0.70}$ with a piecewise geometrical spreading coefficient (0.8 for $0 \leq r \leq 40$ km; 1.1 for $40 \leq r \leq 80$ km and 1.4 for $80 \leq r \leq 105$ km) for the Yellowstone region. Their dataset consists of 2662 three-component waveforms from 283 earthquakes and mining-associated events for the Utah region and 726 three-component waveforms from 223 earthquakes for Yellowstone region. The hypocentral distance ranges of their datasets are out to 500 km and 105 km for Utah and Yellowstone, respectively. Their $Q_S(f)$ estimates are given in Fig. 6.3b.

9) Erickson et al. (2004) compared L_g attenuation between seven different tectonic regions in the continental United States. They obtained $Q_{Lg}(f)=200(\pm 40)\, f^{0.68(\pm 0.12)}$ (Fig. 6.3b) for the Basin and Range Province in the frequency band 0.5 to 16 Hz. Their dataset was consisting of 242 waveforms from 31 earthquakes recorded by 17 stations.

10) Castro et al. (2008c) computed $Qs(f)=83.8\, f^{0.9}$ (Fig. 6.3b) in the frequency range 0.4 and 63.1 Hz in Northeastern Sonora, Mexico. Their data set consists of 44 earthquakes with magnitude range of 1.8 to 3.2 and hypocentral distances range of 25 to 150 km. In the region of Sonora Basin and Range, they obtained that *P*-waves attenuate more than *S*-waves.

As shown in Fig. 6.3a, Akıncı et al. (2013) obtained quite similar Q values ($Q_S(f)=180f^{0.55}$) with the result of this study ($Q_S(f)=190\pm 13.5f^{0.64\pm 0.05}$). The slight differences between the results could be caused different parameterizations, employed data sets and the methodologies used (Ford et al., 2008). For instance, their data set includes this study area as a subregion and consists of recordings from 902 regional earthquakes of magnitude 2.5–5.8 and the distance range of 15-250 km. They used narrow bandpass-filtered time histories around the fixed frequencies and computed a duration window for each filtered time history. They obtained a piecewise geometrical spreading coefficient (1.0 for $1 < r < 20$ km; 0.8 for $20 < r < 40$ km; 0.7 for $40 < r < 100$ km and 0.5 for $r > 100$ km) for the region.

Both of the anelastic attenuation functions for the Basin and Range Province from Erickson et al. (2004) and Jeon & Herrmann (2004) are quite similar with the result of this study (Fig. 6.3b). In recent years, the Aegean extensional region has been compared to Basin & Range province (e.g., Zhu et al., 2006a) since both of them were evaluated as the metamorphic core complexes. Large scale extension, high heat flow and thin continental crust in a tectonically active subduction system environment have characterized both of the regions.

6.3 Source and Site Functions from GIT

6.3.1 Source Functions

After eliminating attenuation function effects from the spectra, another inversion step was utilized to separate source and site functions. To overcome the linear dependence problem between the source and site terms (e.g., Andrews, 1986; Castro et al., 1990, 2003; Oth et al., 2009), the unconstrained-source spectral shape and the constrained-site response methodology were used. According to HVSR site estimates, LA13, LA22 and MAN sites were chosen as reference sites during this inversion step. Figures 5.13 and 5.17 represent GIT spectral source function estimates from each component. Although, most of the source functions have slight fall-off at high frequencies as predicted by simple dislocation model, GIT source function estimates were interpreted as Brune's ω^2 source model (Brune, 1970) which is reasonable for micro- and moderate-size earthquakes.

6.3.2 Site Functions and Comparison with Spectral Ratio Estimates

GIT site functions were obtained for T-, R- and V- component (Figs 5.11 and 5.12). Comparison of GIT site functions with HVSR site estimates were given in Figs 6.4 and 6.5. In order to be able to compare the results, GIT site functions from R- and T-component were divided by V-component GIT site functions. As shown in these figures; large amplitude values of V-component GIT site estimates were observed at varying frequency ranges for different site conditions. This means that the vertical component of motion is influenced by the local structure and causes contamination of spectral ratio site estimates. Malagnini et al. (2004) has suggested that vertical motion transfer function is not amplification free and HVSR does not represent the characteristics of the true horizontal site transfer function. As shown in Figs 6.4 and 6.5, GIT site amplitude values of radial components are larger than transverse ones, especially for the stations located on young and deep sedimentary fill, such as LA01, LA20, LA21, AKH, AYD and NAZ sites. This could be explained by P-to-SV conversion at the bedrock/soil layer contact (Parolai et al., 2004). The differences in the amplitude values from different techniques may arise from complexities in the wave field due to constructive/destructive interference, diffraction, and scattering (Parolai et al., 2004).

Although shallow heterogeneities resulting from varying degrees of weathering or cracking of the rock cause the velocity decrease near surface, the reference rock site definition is needed for probabilistic seismic-hazard assessment. According to V-component GIT site functions, LA13, LA22, LA23, LA26, LA27, LA33, DEU and MAN stations could be considered as reference sites for future studies.

It is known fact that the sites amplify or deamplify the amplitudes of incident motion depending upon the azimuth and incidence angle of the incoming signal (Tucker et al., 1984). These effects can be canceled out using the events at different azimuths and distances (Castro et al., 1990). For that reason, GIT calculations separately performed for two subsets of data (Fig. 5.15, P1- and P2- dataset) to decompose source and site functions and to examine data distribution effect, especially on the site function estimates. Figure 5.16 shows GIT site functions from three components of P1- and P2-dataset: R-component-site functions of P1-dataset are significantly larger than the ones for P2-dataset; T-component site functions of P1- and P2-dataset are much more similar than the ones for R-components; V-component site functions of P1-dataset are significantly lower than the ones for P2-dataset. One of the possible reasons of these results could be eliminating of average attenuation function estimates (Kurtulmuş & Akyol, 2013) from all dataset. On the other hand, the results could also be attributed to the degree of structural complexities such as differences in the basin geometries, velocity and heat flow values, fracturing and fluid saturation along the propagation paths. Bindi et al. (2009) suggested that the discrepancies between the results could be related to lateral variations in velocity and attenuation values caused by basin geometry and edge effects on both of the horizontal and vertical components. Cornou et al. (2003) pointed out the importance of sediment-bedrock interface and structure geometry which control frequency input motion in shaping wave fields. Qin et al. (2012) demonstrated that 3D basin geometry causes a wave-front focusing effect and contributes significantly to a localized strong amplification.

GIT source functions from three components of P1- and P2-dataset are quite similar (Fig. 5.17). Large RMS residuals associated with the inversion results (Fig. 5.14) implies more contamination on R-component of all- and P1-dataset. Closer values of RMS residuals for three components of P2-dataset indicates more homogenous medium, the ray goes through. V-component RMS residuals are smaller than the other components at the frequencies larger than 1 Hz for three datasets. That might imply that the vertical component of motion is less influenced by the local structure (Parolai et al., 2004).

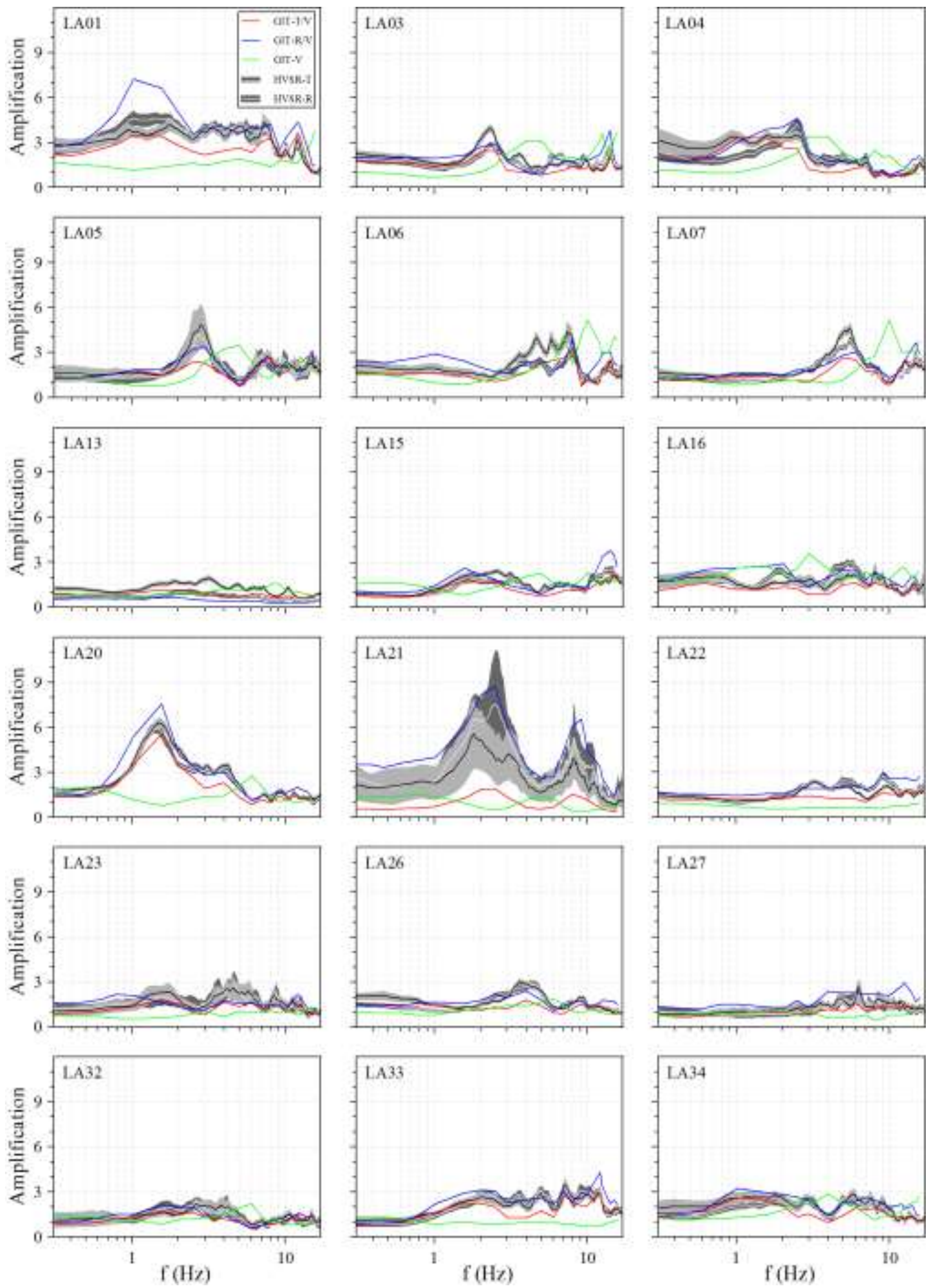

Figure 6.4 GIT site functions from three components of all-dataset for linear array stations together with HVSR estimates. Red, blue and green lines represent GIT site functions from T-, R- and V-component, respectively. RMS values of the residuals associated with the inversion step are given in Fig. 5.14. Black and white lines represent the average HVSR estimates from T- and R- component, respectively, together with 90% confidence interval from *t*-test. Note that, to make the comparison with HVSR estimates, T- and R-component GIT site functions were divided by V-component GIT site functions.

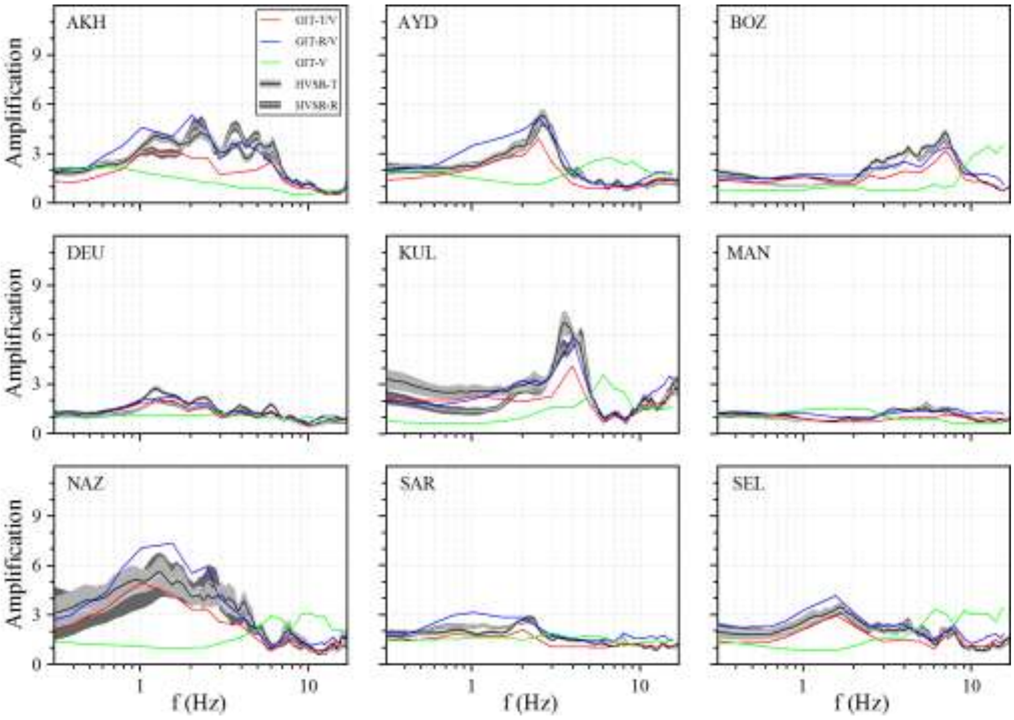

Figure 6.5 GIT site functions from three components of all dataset for regional array stations together with HVSR estimates. Red, blue and green lines represent GIT site functions from T-, R- and V-component, respectively. RMS values of the residuals associated with the inversion step are given in Fig. 5.14. Black and white lines represent the average HVSR estimates from T- and R- component, respectively, together with 90% confidence interval from *t*-test. Note that, to make the comparison with HVSR estimates, T- and R-component GIT site functions were divided by V-component GIT site functions.

Site functions from three different approaches (HVSR, SSR and GIT) are compared in Fig. 6.6. The differences were observed in the amount of the amplitude levels of HVSR, SSR and GIT site estimates. But note that GIT and spectral ratio site functions could be compared, only if, T-component GIT site functions were divided by V-component GIT site functions. Even in this case, GIT and HVSR amplitude levels are close to each other than SSR ones. For that reason discussion on comparison of two spectral ratio estimates (Fig. 6.2) is valid for Fig. 6.6. The differences of site effect functional shapes suggested that HVSR is much less sensitive to basin-induced waves than SSR technique by assuming that basin-induced waves are related to 2D/3D effects (Cornou et al., 2003). Most of the site studies concluded that the HVSR method fails in determination of site transfer function due to both the vertical and horizontal components is amplified at the same resonance frequencies (Ameri et al., 2011). This amplification arises from 2D or 3D effects at the edge of sedimentary basins or due to topography (Bindi et al., 2009). As in Figs 6.4 and 6.5, the results in Fig. 6.6, once again, imply that vertical components of motion are affected by basin-generated waves and contaminate HVSR site estimates with regarding to not only amplitude levels but also functional shapes of site transfer functions due to 2D/3D variations of physical parameters.

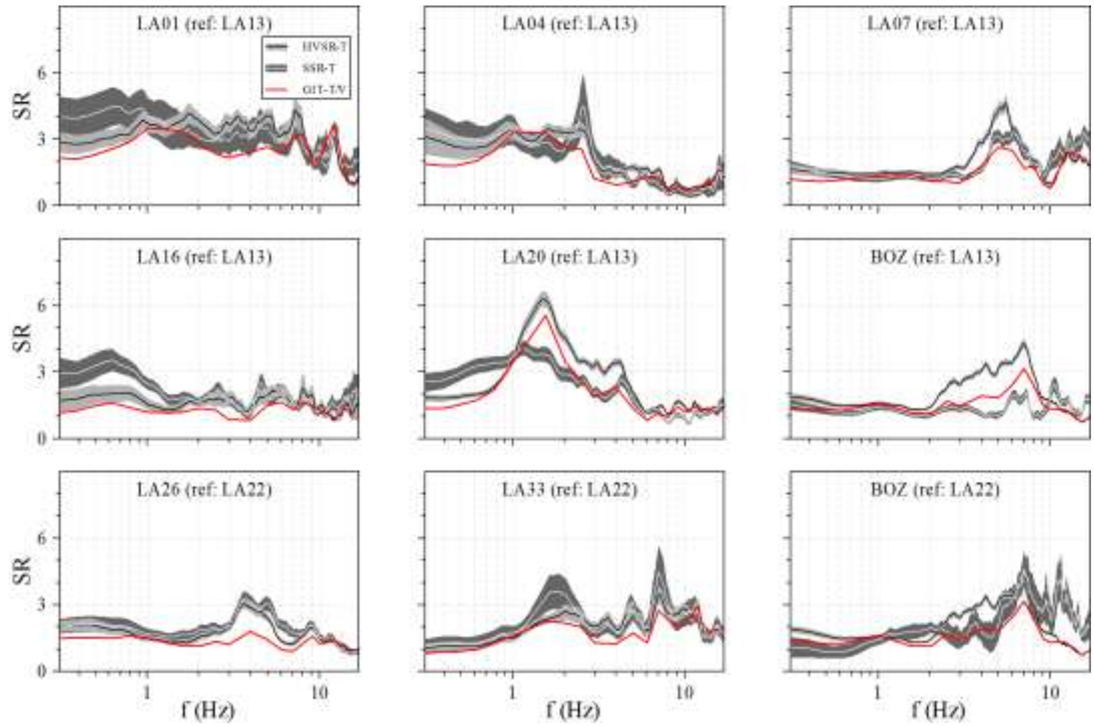

Figure 6.6 The average HVSR-T, SSR-T and GIT-T/V site functions. HVSR and SSR results with 90% confidence interval from *t*-test. Black, white and red lines represent HVSR, SSR and GIT estimates, respectively. *ref*: reference site used for SSR. Note that, SSR results for the BOZ site were estimated by utilizing both of the chosen reference sites.

6.4 Near-Surface Attenuation Parameter (κ)

The near-surface attenuation parameter κ was estimated from T-component spectra for each site (Table 5.1). The distance, magnitude and site dependence of κ were examined in this study. On the other hand, grouping of kappa values according to the site conditions could not be derived, since we were not able to classify the sites. Weak epicentral and magnitude dependencies of κ values with large scattering (Figs 5.18, 5.19, 5.20 and 5.21) for most of the sites was obtained. Similarly, Purvance & Anderson (2003) obtained the absence of a statistically significant dependence of κ on epicentral distance for the Guerrero, Mexico region. Castro et al. (2000) and Fernández et al. (2010) also reported large scattering in the estimates of κ values. Castro et al. (2000) interpreted this result as possibly due to the degree of fracturing for similar source and station paths for the region of Umbria-Marche, Italy.

Generally, κ_0 is considered to be the near-surface attenuation effect of seismic waves beneath the site and that it depends on the site conditions. Although a reliable correlation between κ_0 and geological/geophysical characteristics of a site of interest has still been debated, many field studies present that κ_0 is generally smaller for rock sites than for the sites on alluvium and it can be used as an indicator of site effect (e.g., Akyol et al., 2002a; Atkinson, 1996; Castro et al., 1995). On the other hand, chosen frequency band effects on the results were discussed by some researchers (e.g., Liu et al., 1994; Parolai & Bindi 2004). Parolai & Bindi (2004) showed that weak correlation between site conditions and obtained κ parameters could be caused of narrow spectral windows which are not wide enough to average out the site effects. Kilb et al. (2012) have stated that low values of κ (~5 ms) correspond to seismograms with a lot of high frequency energy, whereas high values of κ (~40 ms) correspond to seismograms with a minimal amount of high-frequency energy.

In this study, obtained minimum and maximum values of κ_0 are 0.015 and 0.049 s for LA05 and AKH sites, respectively. LA05 is located on micaschist unit at the northern slope of the Bozdağ Horst, while AKH is located on alluvium unit of

Akhisar Basin (thickness unknown). Additionally, some of the sites such as LA15, LA26 and BOZ have large κ_0 values with large *fe* values. The results could emphasize that near-surface alteration affects these recording sites.

Obtained *fe* values ranges between 4.88 and 8.7 Hz with an average value of 7.12 (± 0.85) Hz. The minimum and maximum values are obtained for LA20 and BOZ sites, respectively. LA20 site is located on Küçük Menderes Graben, while BOZ site is located on Bozdağ horst. On the other hand, large *fe* values with large κ_0 values were obtained for some of the sites, which have significant amplification values on deep sedimentary units, such as AKH and NAZ. Site transfer functions of these sites might be obscured real *fe* values. Here, an algorithm based on to search minimum error by trying every frequency larger than corner frequency (f_o) was used as an initial point of the linear least-square fits of high frequency slope and all of the processes were checked by visually.

The site and source term dependencies of near-surface attenuation parameter may not have been resolved completely since both site and source terms are frequency dependent. Some researchers have been modeled frequency dependence of near-surface attenuation parameter (e.g., Castro et al., 2008a; 2009) as being in total attenuation effect. On the other hand, some others have been modeled an array average of near-surface attenuation values (e.g., Akıncı et al. 2013; Malagnini et al., 2002) as in the excitation terms which depends on source characteristic such as the energy released and is valid for the average site class. Akıncı et al. (2013) scaled ground motions for western Turkey. Their dataset contains this study area and data set as a subset. They modeled the excitation term by using a Brune source model with a stress drop of 10 MPa for the largest event (M_w=5.8) of the data set and a near-surface attenuation parameter of κ_0 = 0.045 s. An array average κ_0 is 0.031 (± 0.009) s from κ_0 values of 27 different sites for our dataset.

CHAPTER SEVEN
CONCLUSIONS AND RECOMMENDATIONS

In this study, necessary input parameters of the seismic hazard assessment were examined from the recordings of micro- and moderate-size local earthquakes in the central west Turkey. Briefly:

- Site functions of micro and moderate-size earthquakes were obtained utilizing three different approaches (HVSR, SSR and GIT).
- Distance, back-azimuth and magnitude dependencies of HVSR site functions were analyzed for T-component.
- The attenuation characteristics, both *Q(f)* and *b(f)* values, were analyzed for three different hypocentral distance ranges and also for three components.
- GIT source and site functions were decomposed for three components.
- The data distribution effects on GIT source and site functions were examined.
- Near-surface attenuation effect of the station sites was evaluated for T-component.

7.1 Conclusions

The site effects of graben/basin fill thicknesses and its complexity for the deep basin structures in the central west Turkey were emphasized in this study. According to HVSR estimates from T-component, the KUL site (Kula basin) has a peak value of 6.3 at 1.5 Hz, LA01 (Salihli Basin–Gediz Graben) has the largest values of about 4.0 between 1.0 and 7.5 Hz, LA20 (Ödemiş–Küçük Menderes Graben) has a peak value of 6.3 at 1.5 Hz, and NAZ and AYD sites (Nazilli and Aydın–Büyük Menderes Graben) have the largest values of about 5.7 and 5.4 at 1.3 and 2.6 Hz, respectively. In general, HVSR values from T- and R-component are similar within a factor of 2. Back azimuth dependencies of the HVSR estimates are more significant than distance and magnitude dependencies. On the other hand, averaging of all individual T- and R-component HVSR estimates eliminates the systematical differences caused by source radiation effects.

Distribution of average HVSR site functions along the linear array shows that large amplitude values (~5–6) occur over a broad frequency band for the sites close the basin edges due to complexity of wave propagation. These sites pose a high potential seismic risk since 2D/3D variations in the sediment–bedrock structure expand the hazard for whole frequency range interested. The results also show that, even if the site located on horst, the presence of near-surface weathered zones must be evaluated carefully for high frequencies in the site specific seismic hazard studies.

A comparison of two different spectral ratio techniques has showed that SSR estimates give larger values at lower frequencies for the stations on the graben sites. The weak dependence of the HVSR on the window length and the low frequency pattern of SSR results for these sites suggest that basin-generated waves have influence on 1D site effect and locally generated waves affect the vertical components as well as the horizontal ones. For that reason the discrepancies between the results could be attributed to heterogeneity of the region such as 2D/3D variations in regional velocity and attenuation values caused by sediment–bedrock interface and basin geometry.

Crustal attenuation characteristics in the central part of west Turkey were estimated by using a two-step inversion. Non-parametric attenuation functions of T-, R- and V-components were obtained in the first step. In the second step, the behavior of anelastic attenuation, Q and the geometrical spreading exponent, b at different frequencies were analyzed for three different distance range. The b values of all components are ~0.9±0.03 for short paths (10–70 km) within the frequency band of interest. b frequency dependence was modeled as a piecewise in two frequency ranges for entire (10–200 km) and long (120–200 km) distance ranges. These results one more time emphasizes that geometrical spreading can only be associated with the time or distance dependence of the wavefield rather than any particular seismic phase.

Spatial variations of Q were explored to infer anisotropy and analyzed possible causes. Low Q_0 values and strong frequency dependence of Q at short hypocentral distances (10–70 km) could be associated to strong heterogeneity because of high degree of fracturing, fluid filled cracks, young volcanism and/or geothermal activity in the crust. Lower Q frequency dependence and higher Q_0 values manifest more homogenous medium because of increasing density and pressure along with depth for large hypocentral ranges (120–200 km). Frequency dependence is lower and Q_0 is higher for V-component, whereas frequency dependence and Q values obtained for *SH* and *SV* waves do not show significant differences for the distance range between 10 and 70 km. However, in the distance range between 120 and 200 km, $Q_R(f)$ has higher Q_0 value and lower frequency dependence than $Q_T(f)$ and $Q_V(f)$. This Q anisotropy could be associated to plastic flow at greater depth contributing to the dissipation of cracks in the extensional intracontinental plate setting of the region.

Site functions were also obtained for 27 different locations in the central west Turkey, utilizing GIT. Significant V-component GIT site transfer functions for some of the stations indicate contamination of spectral ratio estimates at different frequency bands, which could be related to complexities in the wave field caused by deep or shallow heterogeneities. GIT site functions from two different sub-datasets emphasize the data distribution effect on the results, which could be attributed to the degree of structural complexities in the region such as differences in the basin geometries, velocity and heat flow values, fracturing and fluid saturation along different propagation paths.

GIT source function estimates were interpreted as Brune's ω^2 source model. After eliminating source and attenuation effects, an array average near-surface attenuation parameter κ_0 value obtained as 0.031 (± 0.009) s for the region. The minimum κ_0 value is 0.015 s for LA05 site located on micaschist unit at the northern slope of the Bozdağ Horst, while the maximum κ_0 value is 0.049 s for AKH site located on alluvium unit of deep sedimentary basin. Weak epicentral and magnitude dependence of κ values with large scattering could also be attributed to the complexities along the propagation paths. For some of the stations located on shallow sedimentary deposits or horst, large *fe* values with large κ_0 values were obtained. These results emphasize, once again, near surface weathered zones attenuation effect at high frequencies. In keeping with the literature (e.g., Fernández et al., 2010), they also suggest that κ_0 depends not only on the rock type but also on the degree of fracturing and erosion of the rocks near the recording sites.

7.2 Future Developments and Final Considerations

In engineering point of view, the sites which could be evaluated as reference sites were determined and also possible threats of the other sites with regard to seismic hazard assessments were emphasized. It would be highly desirable to measure shear-wave velocity gradient of the sites, even those located on hard rock and also to know geometry of structural complexities. This would allow much more detailed interpretation of the origin of the observed spectral shapes. Moreover, this study highlights the ongoing need to denser seismic array data for the region to validate and improve 2D/3D evaluations of site functions by utilizing numerical modeling. Comparison of three different approaches for site effect evaluation have shown that interpretations should be based on the results from different approaches, which could be applied to the dataset, since all of the methods have restrictions and also drawbacks between each other.

The attenuation functions could be used in a variety of applications, such as local magnitude estimates, earthquake hazard assessment and structural engineering applications. Note that, obtained attenuation functions represent average values for the region without any azimuthal information contained in each recording. Further work together with increasing level of well-distributed data will provide tomographic inversion of Q_S values. Scattering process of attenuation mechanisms could also be examined in detail.

To improve seismic hazard analysis, spectral source parameters, source radiation and directivity effects are planned to be examined for the central west Turkey. That will provide us more realistic inputs for simulating hypothetic strong ground motion models for the region.

Understanding of source, site and propagation characteristics of ground motion must be the primary research in seismically active regions in our country and all of them should be taken into account for seismic hazard related studies, especially for unconsolidated sediment sites. After that, deterministic and probabilistic seismic hazard maps could be generated for site specific conditions. Description and choice of site are absolutely necessary to avoid from earthquake damages. The geoscientific studies will help to better understand and define how the damages will be minimized.

REFERENCES

Abercrombie, R. E. (1998). A summary of attenuation measurements from borehole recordings of earthquakes: the 10 Hz transition problem. *Pure and Applied Geophysics*, *153*, 475-487.

Akıncı, A., Taktak, G., & Ergintav, S. (1994). Attenuation of coda waves in the western Anatolia. *Physics of the Earth and Planetary Interiors*, *87*, 155-165.

Akıncı, A., Ibanez, J. M., Del Pezzo, E., & Morales, J. (1995a). Geometrical spreading and attenuation of Lg waves: A comparison between western Anatolia (Turkey) and southern Spain. *Tectonophysics*, *250*, 47-60.

Akıncı, A., Del Pezzo, E., & Ibanez, J. M. (1995b). Separation of scattering and intrinsic attenuation in southern Spain and western Anatolia (Turkey). *Geophysical Journal International*, *121*, 337-353.

Akıncı, A., & Eyidoğan, H. (1996). Frequency-dependent attenuation of S and coda waves in Erzincan region (Turkey). *Physics of the Earth and Planetary Interiors*, *97*, 109-119.

Akıncı, A., Mejia, J., & Jemberie, A. (2004). Attenuative disperision of P waves and crustal Q in Turkey and Germany. *Pure and Applied Geophysics*, *161*, 73-91.

Akıncı, A., Malagnini, L., Herrmann, R. B., Gok, R., & Sørensen, M. B. (2006). Ground motion scaling in the Marmara region, Turkey. *Geophysical Journal International*, *166*, 635-651.

Akıncı, A., D'Amico, S., Malagnini, L., & Mercuri, A. (2013). Scaling earthquake ground motions in the western Anatolia, Turkey. *Physics and Chemistry of the Earth*, *63*, 124-135.

Aki, K. (1967). Scaling law of seismic spectrum. *Journal of Geophysical Research*, *72*, 1217–1231.

Akyol, N., Akıncı, A., & Eyidoğan, H. (2002a). Separation of source, propagation and site effects from S waves of local earthquakes in Bursa region, northwestern Turkey. *Pure and Applied Geophysics*, *159*, 1253-1269.

Akyol, N., Akıncı, A., & Eyidoğan, H. (2002b). Site amplification of S-waves in Bursa city and its vicinity, Northwestern Turkey: Comparison of different approaches. *Soil Dynamics and Earthquake Engineering*, *22*, 579-587.

Akyol, N., Zhu, L., Mitchell, B. J., Sözbilir, H., & Kekovalı, K. (2006). Crustal structure and local seismicity in western Anatolia. *Geophysical Journal International*, *166*, 1259-1269.

Akyol, N., & Karagöz, Ö. (2009). Empirical Attenuation Relationships for western Anatolia, Turkey. *Turkish Journal of Earth Sciences*, *18*, 351-382.

Akyol, N., Palas, F., & Sındırgı, P. (2012). Batı Anadolu depremleri için büyüklük-frekans ilişkisinin istatistiksel analizi. *DEÜ Fen ve Mühendislik Dergisi*, *13*, 39-54.

Akyol, N., Kurtulmuş, T. Ö., Çamyıldız, M., & Güngör, T. (2013). Spectral ratio estimates for site effects on the horst–graben system in west Turkey. *Pure and Applied Geophysics*, *170*, 2107-2125.

Aldanmaz, E. (2002). Mantle source characteristics of alkali basalts and basanites in an extensional intracontinental plate setting, western Anatolia, Turkey: Implications for multi-stage melting. *International Geology Review*, *44*, 440-457.

Aldanmaz, E. (2006). Mineral-chemical constraints on the Miocene calc-alkaline and shoshonitic volcanic rocks of western Turkey: Disequilibrium phenocryst assemblages as indicators of magma storage and mixing conditions. *Turkish Journal of Earth Sciences*, *15*, 47-73.

Al-Lazki, A., Sandvol, E., Seber, D., Barazangi, M., Türkelli, N., & Mohamad, R. (2004). Pn tomographic imaging of mantle lid velocity and anisotropy at the junction of the Arabian, Eurasian and African plates. *Geophysical Journal International*, *158*, 1024-1040.

Ameri, G., Oth, A., Pilz, M., Bindi, D., Parolai, S., Luzi, L., et al., (2011). Separation of source and site effects by generalized inversion technique using the aftershock recordings of the 2009 L'Aquila earthquake. *Bulletin of Earthquake Engineering, 9*, 717-739.

Anderson, J. G., & Hough, S. E. (1984). A model for the shape of the Fourier amplitude spectrum of acceleration at high frequencies. *Bulletin of the Seismological Society of America*, *74*, 1969-1993.

Andrews, D. J. (1986). Objective determination of source parameters and similarity of earthquakes of different size. In S. Das, J. Boatwright, & C. H. Scholz, (Eds.). *Earthquake source mechanics* (259-267). Washington, D.C.: American Geophysical Union Monograph.

Atkinson, M. G. (1996). The high frequency shape of the source spectrum for earthquakes in eastern and western Canada. *Bulletin of the Seismological Society of America, 86*, 106-112.

Atkinson, M. G., & Mereu, R. (1992). The shape of ground motion attenuation curves in southeastern Canada. *Bulletin of the Seismological Society of America*, *82*, 2014-2031.

Barazangi, M., Pennington, W., & Isacks, B. (1975). Global study of seismic attenuation in the upper mantle behind Island arcs using pP waves. *Journal of Geophysical Research, 80,* 1079-1092.

Bayrak, Y., Yılmaztürk, A., & Öztürk, S. (2005). Relationships between fundamental seismic hazard parameters for the different source regions in Turkey. *Natural Hazards*, *36*, 445-462.

Bayrak, Y., Öztürk, S., Çınar, H., Kalafat, D., Tsapanos, T. M., Koravos, G. Ch., et al., (2009). Estimating earthquake hazard parameters from instrumental data for different regions in and around Turkey. *Engineering Geology*, *105*, 200–210.

Bayrak, Y., & Bayrak, E. (2012). Regional variations and correlations of Gutenberg–Richter parameters and fractal dimension for the different seismogenic zones in western Anatolia. *Journal of Asian Earth Sciences*, *58*, 98–107.

Bindi, D., Parolai, S., Grosser, S., Milkereit, C., & Karakısa, S. (2006). Crustal attenuation characteristics in northwestern Turkey in the range from 1 to 10 Hz. *Bulletin of the Seismological Society of America*, *96*, 200-214.

Bindi, D., Parolai, S., Cara, F., Di Giulio, G., Ferretti, G., Luzi, L., et al., (2009). Site amplifications observed in the Gubbio basin, Central Italy: Hints for lateral propagation effects. *Bulletin of the Seismological Society of America*, *99*, 741-760.

Bindi, D., Luzi, L., Parolai, S., Di Giacomo, D., & Monachesi, G. (2011). Site effects observed in alluvial basins: The case of Norcia (Central Italy). *Bulletin of Earthquake Engineering*, *9*, 1941-1959.

Biryol, C. B., Beck, S. L., Zandt, G., & Özacar, A. A. (2011). Segmented African Lithosphere Beneath the Anatolian Region Inferred from Teleseismic P-Wave Tomography. *Geophysical Journal International*, *184*, 1037–1057.

Boatwright, J., Seekins, L. C., Fumal, T. E., Liu, H. S., & Mueller, C. S. (1991). Ground motion amplification in the Marina district. *Bulletin of the Seismological Society of America*, *81*, 1980-1997.

Bonilla, L. F., Steidl, J. H., Grant, T. L., Alexei, G. T., & Ralph, J. A. (1997). Site amplification in the San Fernando valley, California: Variability of site-effects estimation using the S-wave, coda, and H/V methods. *Bulletin of the Seismological Society of America*, *87*, 710-730.

Bonilla L. F., Archuleta R. J., & Lavallée, D. (2005). Hysteretic and dilatant behavior of cohesionless soils and their effects on nonlinear site response: Field data observations and modelling. *Bulletin of the Seismological Society of America*, *95*, 2373-2395.

Bonnefoy-Claudet, S., Cornou, C., Bard, P. Y., Cotton, F., Moczo, P., Kristek, J., et al., (2006). H/V ratio: A tool for site effects evaluation. Results from 1-D noise simulations. *Geophysical Journal International*, *167*, 827-837.

Borcherdt, R. D. (1970). Effects of local geology on ground motion near San Francisco Bay. *Bulletin of the Seismological Society of America, 60,* 29-61.

Borcherdt, R. D., & Gibbs, J. F. (1976). Effects of local geological conditions in the San Francisco Bay region on ground motions and intensities of the 1906 earthquakes. *Bulletin of the Seismological Society of America, 66,* 467-500.

Borcherdt R. D., & Wentworth, C. W. (1995). *Strong-ground motion generated by the Northridge earthquake of January 17, 1994. Implications for seismic design coefficients and seismic zonation*. In: 5th international conference on Seismic Zonation Proceedings, vol II. Nice, France, 964–971.

Bozkurt, E. (2001). Neotectonics of Turkey - a synthesis. *Geodinamica Acta*, *14*, 3-30.

Bozkurt, E. (2003). Origin of NNE-trending basins in Western Turkey. *Geodinamica Acta*, *16*, 61-81.

Bozkurt, E., & Mittwede, S. K. (2005). Introduction: Evolution of Neogene extensional tectonics of western Turkey. *Geodinamica Acta*, *18*, 153-165.

Boztepe-Güney, A., & Horasan, G. (2002). Enhanced ground motions due to large-amplitude critical Moho reflections (SmS) in the Sea of Marmara, Turkey. *Geophysical Research Letters*, *29,* 9-1 - 9-4.

Brune, J. (1970). Tectonic strain and the spectra of seismic shear waves from earthquakes. *Journal of Geophysical Research, 75,* 4997-5009.

Cadet, H., Bard, P. Y., & Duval, A. M. (2012). Site effect assessment using KiK-net data: Part 2-site amplification prediction equation based on f(0) and V_{sz}, *Bulletin of Earthquake Engineering, 10,* 451-489.

Cantore, L., Oth, A., Parolai, S., & Bindi, D. (2011). Attenuation, source parameters and site effects in the Irpinia-Basilicata region (southern Apennines, Italy). *Journal of Seismology*, *15*, 375-389.

Castro, R. R., Anderson, J. G., & Singh, S. K. (1990). Site response, attenuation and source spectra of S waves along the Guerrero, Mexico, subduction zone. *Bulletin of the Seismological Society of America*, *80*, 1481-1503.

Castro, R. R., Mungunia, L., & Brune, J. N. (1995). Source spectra and site response from P and S waves of local earthquakes in the Oaxaca, Mexico, subduction zone. *Bulletin of the Seismological Society of America*, *85*, 923-936.

Castro, R. R., Monachesi, G., Mucciarelli, M., Trojani, L., & Pacor, F. (1999). P- and S-wave attenuation in the region of Marche, Italy. *Tectonophysics*, *302*, 123-132.

Castro, R. R., Trojani, L., Monachesi, G., Mucciarelli, M., & Cattaneo, M. (2000). The spectral decay parameter κ in the region of Umbria-Marche, Italy. *Journal of Geophysical Research*; *105*, 23.811-23.823.

Castro, R. R., Fabriol, H., Bour, M., & Le Brun, B. (2003). Attenuation and site effects in the region of Guadeloupe, Lesser Antilles. *Bulletin of the Seismological Society of America*, *93*, 612-626.

Castro, R. R., Pacor, F., Bindi, D., Franceschina, G., & Luzi, L. (2004). Site response of strong motion stations in the Umbria, Central Italy region. *Bulletin of the Seismological Society of America*, *94*, 576-590.

Castro, R. R., Massa, M., Augliera, P., & Pacor, F. (2008a). Body-wave attenuation in the region of Garda, Italy. *Pure and Applied Geophysics*, *165*, 1351-1366.

Castro, R. R., Gallipoli, M. R., & Mucciarelli, M. (2008b). Crustal Q in southern Italy determined from regional earthquakes. *Tectonopyhsics*, *457*, 96-101.

Castro, R. R., Condori, C., Romero, O., Jacques, C., & Suter, M. (2008c). Seismic attenuation in northeastern Sonora, Mexico. *Bulletin of the Seismological Society of America*, *98*, 722-732.

Castro, R. R., Huerta, C. I., Romero, O., Jacques, C., Hurtado, A., & Fernández, A. I. (2009). Body-wave attenuation near the rupture of the 1887 Sonora, México, earthquake (Mw 7.5). *Geofisica Internacional*, *48*, 297-304.

Chavez-Garcia, F. J., Stephenson, W. R., & Rodríguez, M. (1999). Lateral propagation effects observed at Parkway, New Zealand. A case history to compare 1D versus 2D site effects. *Bulletin of the Seismological Society of America*, *89*, 718-732.

Cong, L., & Mitchell, B. J. (1998). Lg Coda Q and its relation to the geology and tectonics of the Middle East. *Pure and Applied Geophysics*, *153*, 563-585.

Cornou, C., Bard, B. Y., & Dietrich, M. (2003). Contribution of dense array analysis to identification and quantification of basin-edge induced waves. Part II: Application to Grenoble basin (French Alps). *Bulletin of the Seismological Society of America*, *93*, 2624-2648.

Çamyıldız, M. (2008). *Comparison of the parameters belonging to different sites in west Anatolia*. BSc Thesis, Dokuz Eylül University Engineering Faculty, Department of Geophysical Engineering, İzmir.

Çemen, İ., Catlos, E. J., Göğüs, O., & Özerdem, C. (2006). Post-collisional extensional tectonics and exhumation of the Menderes massif in the Western Anatolia extended terrane, Turkey. In Y. Dilek, & S. Pavlides, (Eds.). *Post-collisional tectonics and magmatism in the Mediterranean region and Asia* (353–379). Colorado: Geological Society of America Special Paper.

Çiftçi, N. B., & Bozkurt, E. (2009). Evolution of the Miocene sedimentary fill of the Gediz graben, SW Turkey. *Sedimentary Geology*, *216(3-4)*, 49-79.

Çiftçi, N. B., & Bozkurt, E. (2010). Structural evolution of the Gediz graben, SW Turkey: Temporal and spatial variation of the graben basin. *Basin Research*, *22*, 846-873.

Çiftçi, N. B., Temel, R. O., & İztan, Y. H. (2010). Hydrocarbon occurrences in the western Anatolian (Aegean) grabens, Turkey: is there a working petroleum system?. *AAPG Bulletin*, *94*, 1827-1857.

Der, Z. A. (1998). High-frequency P- and S-wave attenuation in the Earth. *Pure and Applied Geophysics*, *153*, 273-310.

Dewey, J. F., & Şengör, A. M. C. (1979). Aegean and surrounding regions: Complex multiple and continuum tectonics in a convergent zone. *Geological Society of America Bulletin*, *90*, 84-92.

Dilek, Y. (2005). Tectonics of Post-Collisional volcanism in Cenozoic western Anatolia (Turkey). *GSA Annual Meeting Abstracts with Programs*, *37*, 389.

Di Luccio, F., & Pasyanos, M. E. (2007). Crustal and Upper Mantle Structure in the Eastern Mediterranean from the Analysis of Surface Wave Dispersion Curves. *Geophysical Journal International*, *169*, 1139-1152.

Dravinski, M., Ding, G., & Wen, K.-L. (1996). Analysis of spectral ratios for estimating ground motion in deep basins. *Bulletin of the Seismological Society of America*, *86*, 646-654.

Drouet, S., Chevrot, S., Cotton, F., & Souriau, A. (2008). Simultaneous inversion of source spectra, attenuation parameters, and site responses: Application to the data of the French accelerometric network. *Bulletin of the Seismological Society of America*, *98*, 198-219.

Emre, T., Tavlan, M., Akkiraz, M. S., & İşintek, İ. (2010). Stratigraphy, sedimentology and palynology of the Neogene-Pleistocene (?) rocks around Akçaşehir-Tire-İzmir (Küçük Menderes graben, Western Anatolia). *Turkish Journal of Earth Sciences*, *20*, 27-56.

England, P. C. (2003). The alignment of earthquake T-axes with the principal axes of geodetic strain in the Aegean region. *Turkish Journal of Earth Sciences*, *12*, 47-53.

Erdik, M., & Durukal, E. (2003). Simulation modeling of strong ground motion. In W. F. Chen, & C. Scawthorn, (Eds.). *Earthquake Engineering Handbook* (16-67). Boca Raton, Florida: CRC Press.

Erickson, D., McNamara, D. E., & Benz, H. M. (2004). Frequency dependent Lg Q within the continental United States. *Bulletin of the Seismological Society of America*, *94*, 1630-1643.

Eskişar, T., Özyalın, Ş., Kuruoğlu, M., & Yılmaz, H. R. (2013). Microtremor measurements in the northern coast of Izmir Bay, Turkey to evaluate site specific characteristics and fundamental periods by H/V spectral ratio method. *Journal of Earth System Science*, *122*, 123-136.

Eyidoğan, H., & Jackson, J. (1985). A seismological study of normal faulting in the Demirci, Alaşehir and Gediz earthquake of 1960–1970 in western Turkey: Implications for the nature and geometry of deformation in the continental crust. *Geophysical Journal of the Royal Astronomical Society*, *81*, 569–607.

Fernández, A.I., Castro, R.R., & Huerta, C.I. (2010). The spectral decay parameter kappa in Northeastern Sonora, Mexico. *Bulletin of the Seismological Society of America*, *100*, 196-206.

Field, E. H. (1996). Spectral amplification in a sediment-filled valley exhibiting clear basin-edge-induced waves. *Bulletin of the Seismological Society of America*, *86*, 991-1005.

Field, E. H., & Jacob, K. H. (1995). A comparison and test of various site-response estimation techniques, including three that are not reference-site dependent. *Bulletin of the Seismological Society of America*, *85*, 1127-1143.

Flerit, F., Armijo, R., King, G., & Meyer, B. (2004). The mechanical interaction between the propagating North Anatolian Fault and the back-arc extension in the Aegean. *Earth and Planetary Science Letters*, *224*, 347–362.

Floyd, M. A., Billiris, H., Paradissis, D., Veis, G., Avallone, A., Briole, P., et al., (2010). A new velocity field for Greece: implications for the kinematics and dynamics of the Aegean. *Journal of Geophysical Research*, *115,* B10403.

Ford, S. R., Dreger, D. S., Mayeda, K., Walter, W. R., Malagnini, L., & Phillips, W. R. (2008). Regional attenuation in northern California: A comparison of five 1D Q methods. *Bulletin of the Seismological Society of America, 98*, 2033-2046.

Gao, S., Liu, H., Davis, P. M., & Knopoff, L. (1996). Localized amplification of seismic waves and correlation with damage due to the Northridge earthquake: Evidence for focusing in Santa Monica. *Bulletin of the Seismological Society of America*, *86(1B),* S209-S230.

Gessner, K., Ring, U., Johnson, C., Hetzel, R., Passchier, C. W., & Güngör, T. (2001). An active bivergent rollinhinge detachment system. Central Menderes metamorphic core complex in western Turkey. *Geology, 29*, 611-614.

Goetz, R. P. (2009). *Study of the horizontal-to-vertical spectral ratio (hvsr) method for characterization of deep soils in the Mississippi embayment*. MSc thesis, The Faculty of the Graduate School University of Missouri, Columbia.

Göktürkler, G., Şalk, M., & Sarı, C. (2003). Numerical modeling of the conductive heat transfer in western Anatolia. *Journal of Balkan Geophysical Society, 6,* 1-15.

Gürer, A., & Bayrak, M. (2007). Relation between electrical resistivity and earthquake generation in the crust of west Anatolia, Turkey. *Tectonophysics*, *445,* 49-65.

Gürer, O. F., Sarıca-Filoreau, N., Ozburan, M., Sangu, E., & Doğan, B. (2009). Progressive development of the Buyuk Menderes graben based on new data, western Turkey. *Geological Magazine*, *146*, 652–673.

Hammer, P. T. C., Clowes, R. M., & Ellis, R.M. (2000). Crustal structure of NW British Columbia and SE Alaska from seismic wide-angle studies: coast plutonic complex to Stikinia. *Journal of Geophysical Research, 105*, 7961-7981.

Hanks, T. C. (1982). fmax. *Bulletin of the Seismological Society of America*, *72,* 1867-1880.

Hartzell, S. H. (1992). Site response estimation from earthquake data. *Bulletin of the Seismological Society of America*, *82*, 2308-2327.

Hearn, T. M. (1999). Uppermost mantle velocities and anisotropy beneath Europe. *Journal of Geophysical Research*, *104(B7)*, 15.123-15.139.

Hearn, T. M., & Ni, J. (1994). Pn velocities beneath continental collision zones: The Turkish-Iranian plateau. *Geophysical Journal International*, *117*, 273-283.

Hetzel R., Passchier, C. W., Ring, U., & Dora, O. Ö. (1995). Bivergent extension in orogenic belts: the Menderes Massif (southwestern Turkey). *Geology*, *23*, 455-458.

Horasan, G., Kaşlılar-Özcan, A., Boztepe-Güney, A., & Niyazi, T. (1998). S-wave attenuation in the Marmara Sea, northwestern Turkey. *Geophysical Research Letters*, *25*, 2733-2736.

Horasan, G., & Boztepe-Güney, A. (2004). S-wave attenuation in the Sea of Marmara, Turkey. *Physics of the Earth and Planetary Interiors*, *142*, 215-224.

Huang, H.-C., & Teng, T.-L. (1999). An evaluation on h/v ratio vs. spectral ratio for site-response estimation using the 1994 Northridge earthquake sequences. *Pure and Applied Geophysics*, *156*, 631-649.

Ibáňez, J. M., Del Pezzo, E., Alguacil, G., De Miguel, F., Morales, J., De Martino, S., et al., (1993). Geometrical spreading function for short-period S and coda waves recorded in southern Spain. *Physics of the Earth and Planetary Interiors*, *80*, 25-36.

İlkışık, O. M. (1995). Regional heat flow in western Anatolia using silica temperatures estimates from thermal springs. *Tectonophysics*, *244*, 175-184.

Jackson, J., & McKenzie, D. (1988). The relationship between plate motions and seismic tremors, and the rates of active deformation in the Mediterranean and Middle East. *Geophysical Journal of Royal Astronomical Society, 93,* 45–73.

Jeon, Y. S. & Herrmann, R. B. (2004). High-frequency earthquake ground-motion scaling in Utah and Yellowstone. *Bulletin of the Seismological Society of America*, *94*, 1644-1657.

Jolivet, L., Faccenna, C., Huet, B., Labrousse, L., Le Pourhiet, L., Lacombe, O., et al. (2013). Aegean tectonics: Strain localisation, slab tearing and trench retreat. *Tectonophysics*, (*597-598*), 1-33.

Kalafat, D., Gürbüz, C., & Üçer, B. (1987). Investigation of the crust and upper mantle in the west of Turkey. *Deprem Arastirma Bulteni*, 14(59), 43-64.

Kandilli Obsevatory & Earthquake Research Institute (2014). *Earthquake catalogue of Turkey and surrounding region*. Retrived February 10, 2014, from http://www.koeri.boun.edu.tr/sismo/.

Kaşlılar-Özcan, A., Boztepe-Güney, A., & Ecevitoğlu, B. (2002). Estimation of attenuation structure in the Çınarcık Basin of the Marmara Sea, northwest Turkey. *Physics of the Earth and Planetary Interiors, 130,* 1-16.

Kilb, D., Biasi, G., Anderson, J. G., Brune, J., Peng, Z., & Vernon, F. L. (2012). A comparison of spectral parameter kappa from small and moderate earthquakes using Southern California ANZA seismic network data. *Bulletin of the Seismological Society of America, 102*, 284-300.

Kiratzi, A. A. (2002). Stress tensor inversions along the westernmost North Anatolian fault zone and its continuation into the North Aegean Sea. *Geophysical Journal International*, *151*, 360–376.

Kiratzi, A., & Louvari, E. (2003). Focal mechanisms of shallow earthquakes in the Aegean Sea and the surrounding lands determined by waveform modelling: A new database. *Journal of Geodynamics, 36*, 251–274.

Kitagawa, Y., Okawa, I., & Kashima, T. (1992). Observation and analyses of dense strong motions at sites with different geological conditions in Sendai. In *Proceedings of International Symposium on the Effects of Surface Geology on Seismic Motions*, Association of Earthquake Disaster Prevention, Odawara, Japan, 311-6.

Koçyiğit, A., Yusufoğlu, H., & Bozkurt, E. (1999). Evidence from the Gediz Graben for episodic two-stage extension in western Turkey. *Journal of the Geological Society London*, *156*, 605-616.

Kramer, S. L. (1996). *Geotechnical earthquake engineering*. New Jersey: Prentice Hall.

Kurtulmuş, T. Ö., & Akyol, N. (2013). Crustal attenuation characteristics in western Turkey. *Geophysical Journal International*, *195*, 1384-1394.

Ktenidou, O. J., Gelis, C., & Bonilla, F. (2013). A study on the variability of kappa in a borehole, implications on the computation method used. *Bulletin of the Seismological Society of America*, *103*, 1048-1068.

Lachet, C., Hatzfeld, D., Bard, P-Y., Theodulidis, N., Papaioannou, C., & Savvaidis, A. (1996). Site effects and microzonation in the city of Thessaloniki (Greece) comparison of different approaches. *Bulletin of the Seismological Society of America*, *86*, 1692-1703.

Lay, T., & Wallace, T. C. (Eds). (1995). *Modern global seismology*, California: Academic Press.

Le Pichon, X., & Angelier, J. (1979). The Hellenic arc and trench system: A key to the neotectonic evolution of the Eastern Mediterranean area. *Tectonophysics*, *60*, 1-42.

Le Pichon, X., Chamot-Rooke, C., Lallemant, S., Noomen, R., & Veis, G. (1995). Geodetic determination of the kinematics of central Greece with respect to Europe: Implications for Eastern Mediterranean tectonics. *Journal of Geophysical Research*, *100*, 12675-12690.

Le Pichon, X., & Kreemer, C. (2010). The Miocene-to-Present kinematic evolution of the Eastern Mediterranean and Middle East and its implications for dynamics. *Annual Review of Earth and Planetary Sciences*, *38*, 323-351.

Lermo, J., & Chávez-García, F. J. (1993). Site effect evaluation using spectral ratios with only one station. *Bulletin of the Seismological Society of America*, *83*, 1574-1594.

Lermo, J., & Chávez-García, F. J. (1994). Are microtremors useful in site response evaluation? *Bulletin of the Seismological Society of America, 84*, 1350-1364.

Liu, Z., Wuenscher, M. E., & Herrmann, R. B. (1994). Attenuation of body waves in the central New Madrid Seismic Zone. *Bulletin of the Seismological Society of America*, *84*, 1112-1122.

Lowrie, W. (1997). *Fundamentals of geophysics.* Cambdirge: Cambridge University Press.

Lunedei, E., & Albarello, D. (2009). On the seismic noise wave field in a weakly dissipative layered Earth. *Geophysical Journal International*, *177*, 1001-1014.

Malagnini, L., Akıncı, A., Herrmann, R. B., Pino, N. A., & Scognamiglio, L. (2002). Characteristics of the ground motion in northeastern Italy. *Bulletin of the Seismological Society of America, 92*, 2186-2204.

Malagnini, L., Mayeda, K., Akıncı, A., & Bragato, P. L. (2004). Estimating absolute site effects. *Bulletin of the Seismological Society of America, 94*, 1343-1352.

McClusky, S., Balassanian, S., Barka, A., Demir, C., Ergintav, S., Georgiev, I., et al., (2000). Global positioning system constraints on plate kinematics and dynamics in the eastern Mediterranean and Caucasus. *Journal of Geophysical Research*, *105*, 5695-5720.

McKenzie, D. (1972). Active tectonics in the Mediterranean region. *Geophysical Journal of the Royal Astronomical Society, 30*, 109-185.

McKenzie, D. (1978). Active tectonics of the Alpine-Himalayan belt: the Aegean sea and surrounding regions. *Geophysical Journal of the Royal Astronomical Society, 55*, 217-254.

Menke, W. (1989). *Geophysical data analysis: Discrete inverse theory* (2nd ed.). New York: Academic Press.

Mitchell, B. J. (1995). Anelastic structure and evolution of the continental crust and upper mantle from seismic surface wave attenuation. *Reviews of Geophysics*, *33*, 441-462.

Mitchell, B. J., & Xie, J. (1994). Attenuation of multiphase surface waves in the basin and range province-III. Inversion for crustal anelasticity. *Geophysical Journal International*, *116*, 468-484.

Mitchell, B. J. & Romanowicz, B. (1998). Introduction. *Pure and Applied Geophysics*, *153*, 235–236.

Mooney, W. D., & Braile, L. W. (1989). The seismic structure of the continental crust and upper mantle of North America. In A. Bally, & P. Palmer, (Eds.). *The Geology of North America: An overview* (39-52). Colarado: Geological Society of America Special Papers.

Morozov, I. B. (2010). *Seismological attenuation without Q*. Bloomington: Trafford Publishing.

Mutlu, H. (2007). Constraints on the origin of the Balıkesir thermal waters (Turkey) from stable isotope ($\delta^{18}O$, δD, $\delta^{13}C$, $\delta^{34}S$) and major-trace element compositions. *Turkish Journal of Earth Sciences*, *16*, 13-32.

Mutlu, A. K. (2012). *Imaging the upper mantle beneath Turkey and surrounding regions*. PhD Thesis, Geophysics Department of Boğaziçi University, İstanbul.

Mutlu, A. K., & Karabulut, H. (2011). Anisotropic Pn tomography of Turkey and adjacent regions. *Geophysical Journal International*, *187*, 1743-1758.

Nakamura, Y. (1989). A method for dynamic characteristics estimations of subsurface using microtremors on the ground surface. *Quarterly Report of Railway Technical Research Institute*, Japan, *30*, 25-33.

Nakamura, Y. (2000). Clear identification of fundamental idea of Nakamura's technique and its applications. In *Proceedings of the 12th World Conference on Earthquake Engineering*, Paper no. 2656, Auckland, New Zealand.

Narayan, J. P. (2005). Study of basin-edge effects on the ground motion characteristics using 2.5-D modeling. *Pure and Applied Geophysics*, *162*, 273-289.

Nogoshi, M., & Igarashi, T. (1970). On the propagation characteristics of microtremors. *Journal of the Seismological Society of Japan*, *23*, 264-280.

Nyst, M., & Thatcher, W. (2004). New constraints on the active deformation of the Aegean. *Journal of Geophysical Research*, *109*, B11406.

Olafsson, S., Sigbjörnsson, R., & Einarsson, P. (1998). Estimation of source parameters and Q from acceleration recorded in the Vatnafjöll earthquake in south Iceland. *Bulletin of the Seismological Society of America*, *88*, 556-563.

Oliver, J., & Isacks, B. (1967).Deep earthquake zones, anomalous structures in the upper mantle, and the lithosphere. *Journal of Geophysical Research*, *72*, 4259-75.

Oral, M. B., Reilinger, R. E., Tokgöz, M. N., Kong, R. W., Barka, A. A., Kınık, İ., et al., (1995). Global positioning system offers evidence of plate motions in eastern Mediterranean. *EOS Transaction*, *76*, 9.

Oth, A. P. H. (2007). *Source processes and spectral ground motion models of intermediate-depth Vrancea (Romania) earthquakes.* PhD Thesis, the Faculty of Physics of the University of Karlsruhe (TH), Karlsruhe.

Oth, A., Parolai, S., Bindi, D., & Wenzel, F. (2009). Source spectra and site response from S waves of intermediate-depth Vrancea, Romania earthquakes. *Bulletin of the Seismological Society of America*, *99*, 235-254.

Oth, A., Bindi, D., Parolai, S., & Di Giacomo, D. (2011). Spectral analysis of K-NET and KiK-net data in Japan, Part II: On attenuation characteristics, source spectra, and site response of borehole and surface stations. *Bulletin of the Seismological Society of America, 101*, 667-687.

Özalaybey, S., Zor, E., Ergintav, S., & Tapırdamaz, C. (2011). Investigation of 3-D basin structures in the Izmit Bay area (Turkey) by single-station microtremor and gravimetric methods. *Geophysical Journal International*, *186*, 883-894.

Padhy, S. (2009). Characteristics of body-wave attenuations in the Bhuj Crust. *Bulletin of the Seismological Society of America*, *99*, 3303-3313.

Papazachos, C. B. (1999). An alternative method for a reliable estimation of seismicity with an application in Greece and surrounding area. *Bulletin of the Seismology Society of America*, *89*, 111-119.

Papazachos, C. B., Hatzidimitriou, P. M., Panagiotopoulos, D. G., & Tsokas, G. N. (1995). Tomography of the Crust and Upper Mantle in Southeast Europe. *Journal of Geophysical Research, 100*, 148-227.

Parolai, S. (2012). Investigation of site response in urban areas by using earthquake data and seismic noise. In P. Bormann, (Ed.). *New manual of seismological observatory practice 2 (NMSOP-2)*, IASPEI, GFZ German Research Centre for Geosciences, Potsdam.

Parolai, S., Bindi, D., & Augliera, P. (2000). Application of the generalized inversion technique (GIT) to a microzonation study: numerical simulations and comparison with different site-estimation techniques. *Bulletin of the Seismological Society of America*, *90*, 286-297.

Parolai, S., & Bindi, D. (2004). Influence of soil-layer properties on *k* evaluation. *Bulletin of the Seismological Society of America*, *94*, 349-356.

Parolai, S., & Richwalski, S. M. (2004). The importance of converted waves in comparing H/V and RSM site responses. *Bulletin of the Seismological Society of America*, *94*, 304-313.

Parolai, S., Bindi, D., Baumbach, M., Grosser, H., Milkereit, C., Karakisa, S., et al., (2004). Comparison of different site response estimation techniques using aftershocks of the 1999 Izmit earthquake. *Bulletin of the Seismological Society of America*, *94*, 1096-1108.

Pe-Piper, G., & Piper, D. J. W. (2001). Late Cenozoic post-collisional Aegean igneous rocks: Nd and Sr isotopic constraints on petrogenetic and tectonic models. *Geological Magazine*, *138*, 653-668.

Petukhin, A. G., & Irikura, K. (2000). A method for the separation of source and site effects and the apparent Q structure from strong motion data. *Geophysical Research Letters*, *27*, 3429-3432.

Polat, O., Gök, E., & Yılmaz, D. (2008). Earthquake hazard of Aegean Extension Region, Turkey. *Turkish Journal of Earth Science*, *17*, 593-614.

Purvance, M. D., & Anderson, J. G. (2003). A comprehensive study of the observed spectral decay in strong-motion accelerations recorded in Guerrero, Mexico. *Bulletin of the Seismological Society of America*, *93*, 600-611.

Qin, Y., Wang, Y., Taneka, H., & Zhang, X. (2012). Seismic ground motion amplification in a 3D sedimentary basin: the Effect of the vertical velocity gradient. *Journal of Geophysics and Engineering*, *9*, 761-772.

Reilinger, R., McClusky, S., Paradissis, D., Ergintav, S., & Vernant, P. (2010). Geodetic constraints on the tectonic evolution of the Aegean region and strain accumulation along the Hellenic subduction zone. *Tectonophysics*, *488*, 22–30.

Riepl, J., Bard, P.-Y., Hatzfeld, D., Papaioannou, C., & Nechtschein, S. (1998). Detailed evaluation of site response estimation methods across and along the sedimentary valley of Volvi (EURO-SEISTEST). *Bulletin of the Seismological Society of America*, *88*, 488-502.

Rogers, A. M., Borcherdt, R. D., Covington, P. A., & Perkins, D. M. (1984). A comparative ground response study near Los Angeles using recordings of Nevada nuclear tests and the 1971 San Fernando Earthquake. *Bulletin of the Seismological Society of America*, *74*, 1925-1949.

Rojay, B., Toprak, V., Demirci, C., & Süzen, L. (2005). Plio-Quaternary evolution of the Küçük Menderes graben southwestern Anatolia, Turkey. *Geodinamica Acta*, *18*, 317-331.

Romanowicz, B. (1995). A global tomographic model of shear attenuation in the upper mantle. *Journal of Geophysical Research*, *100*, 12375-12394.

Salazar, W., Sardina, V., & de Cortina, J. (2007). A hybrid inversion technique for the evaluation of source, path and site effects employing S-wave spectra for subduction and upper-crustal earthquakes in El Salvador. *Bulletin of the Seismological Society of America*, *97*, 208-221.

Sarı, C., & Şalk, M. (2006). Sediment thicknesses of the western Anatolia graben structures determined by 2D and 3D analysis using gravity data. *Journal of Asian Earth Sciences*, *26*, 39-48.

Saunders, P., Priestly, K., & Taymaz, T. (1998). Variations in the crustal structures beneath western Turkey. *Geophysical Journal International*, *134*, 373-389.

Sayıl, N., & Osmanşahin, İ. (2008). An investigation of seismicity for western Anatolia. *Natural Hazard*, *44*, 51-64.

Sayın, A. (2007). Origin of kaolin deposits: Evidence from the Hisarcık (Emet-Kütahya) deposits, Western Turkey. *Turkish Journal of Earth Sciences*, *16*, 77-96.

Sereno, T. J., & Given, J.W. (1990). P_n attenuation for a spherically symmetric Earth model. *Geophysical Research Letters*, *17*, 1141-1144.

Seyitoğlu, G., & Scott, B. C. (1991). Late Cenozoic crustal extension and basin formation in west Turkey. *Geological Magazine*, *128*, 155-166.

Seyitoğlu, G., & Scott, B. C. (1992). The age of Büyük Menderes Graben (west Turkey) and its tectonic implications. *Geological Magazine*, *129*, 239-242.

Seyitoğlu, G., & Işık, V. (2009). Meaning of the Küçük Menderes graben in the tectonic framework of the central Menderes metamorphic core complex (western Turkey). *Geologica Acta*, *7,* 323-331.

Sodoudi, F., Kind, R., Hatzfeld, D., Priestley, K., Hanka, W., Wylegalla, K., et al. (2006). Lithospheric Structure of the Aegean Obtained from P and S Receiver Functions. *Journal of Geophysical Research*, *111*, B12.

Sokolov, V., Bonjer, K. -P., Oncescu, M., & Rizescu, M. (2005). Hard rock spectral models for intermediate-depth Vrancea, Romania, earthquakes. *Bulletin of the Seismological Society of America, 9*5, 1749-1765.

Sonley, E., & Atkinson, G. M. (2006). Path-specific attenuation in eastern Canada. *Bulletin of the Seismological Society of America*, *96*, 1375-1382.

Steidl, J. H. (1993). Variation of site response at the UCSB dense array of portable accelerometers. *Earthquake Spectra*, *9,* 289-302.

Steidl, A. G., Tumarkin, A. G., & Archuleta, R. J. (1996). What is a reference site? *Bulletin of the Seismological Society of America, 86*, 1733-1748.

Stein, S., & Wysession, M. (2003). *An introduction to seismology, earthquakes and earth structure*. Oxford: Blackwell Publishing.

Süzen, M. L., Toprak, V., & Rojay, B. (2006). High-altitude Plio Quaternary fluvial deposits and their implication on the tilt of a horst, Western Anatolia, Turkey. *Geomorphology, 74(1-4)*, 80-99.

Syuhada (2010). *Seismic attenuation anisotropy in the southernmost part of the Taupo Volcanic Zone, North Island, New Zealand*. MSc Thesis, Victoria University of Wellington, Wellington.

Şafak, E. (1997). Models and methods to characterize site amplification from a pair of records. *Earthquake Spectra*, *13,* 97-129.

Şafak, E. (2001). Local site effects and dynamic soil behaviour. *Soil Dynamics and Earthquake Engineering*, *21*, 453-458.

Şahin, Ş. (2008). Lateral variations of coda Q and attenuation of seismic waves in southwest Anatolia. *Journal of Seismology*, *12,* 367-376.

Şahin, Ş., Erduran, M., Alptekin, Ö., & Çakır, Ö. (2007). Intrinsic and scattering seismic attenuation in southwestern Anatolia. *Pure and Applied Geophysics*, *164,* 2255-2270.

Şahin, Ş., Bao, X., Türkelli, N., Sandvol, E., Teoman, U., & Kahraman, M. (2013). Lg wave attenuation in the Isparta angle and Anatolian plateau (Turkey). *Pure and Applied Geophysics*, *170,* 337-351.

Şengör, A. M. C. (1979). The North Anatolian transform fault: its age, offset and tectonic significance. *Journal of Geological Society London*, *136,* 269-282.

Şengör, A. M. C. (1987). Cross-faults and differential stretching of hanging walls in regions of low-angle normal faulting: examples from Western Turkey. In M. P. Coward, J. F. Dewey, & P. Hancock, (Eds.). *Continental extensional tectonics* (575-589). London: Geological Society London Special Publications.

Şengör, A. M. C., Satır, M., & Akkök, R. (1984). Timing of the tectonic events in the Menderes massif, western Turkey: Implications for tectonic evolution and evidence for Pan-African basement in Turkey. *Tectonics*, *3,* 693-707.

Şengör, A. M. C., Görür, N., & Şaroğlu, F. (1985). Strike-slip faulting and related basin formation in zones of tectonic escape: Turkey as a case study. In K. T. Biddle, & N. Christie-Blick, (Eds.) *Strike-slip faulting and basin formation* (227-264). Society of Economic Paleontologists and Mineralogists Special Publication.

Tarcan, G., Filiz, S., & Gemici, U. (2000). Geology and geochemistry of the Salihli geothermal fields, Turkey. *World Geothermal Congress,* Kyushu-Tohoku, Japan, p.1829-1834.

Taymaz, T., Jackson, J., & McKenzie, D. (1991). Active tectonics of the North and Central Aegean Sea. *Geophysical Journal International*, *106,* 433-490.

Theodulidis, N., & Bard, P.-Y. (1995). Horizontal to vertical spectral ratio and geological conditions: An analysis of strong motion data from Greece and Taiwan. *Soil Dynamics and Earthquake Engineering*, *14*, 177-197.

Tokçaer, M., Agostini, S., & Savasçın, M. Y. (2005). Geotectonic setting and origin of the youngest Kula volcanics (western Anatolia), with a new emplacement model. *Turkish Journal of Earth Sciences*, *14*, 145-166.

Tonarini, S., Agostini, S., Innocenti, F., & Manetti, P. (2005). d_{11}B as tracer of slab dehydration and mantle evolution in western Anatolia Cenozoic magmatizm. *TerraNova*, *17*, 259-264.

Triantafyllidis, P., Hatzidimitriou, P. M., Theodulidis, N., Suhadolc, P., Papazachos, C., Raptakis, D., et al., (1999). Site effects in the city of Thessaloniki (Greece) estimated from acceleration data and 1D local soil profiles. *Bulletin of the Seismological Society of America*, *89*, 521-537.

Tsai, C.-C. P., & Chen, K.-C. (2000). A model for the high-cut process of strong motion accelerations in terms of distance, magnitude, and site condition: An example from the SMART 1 array, Lotung, Taiwan. *Bulletin of the Seismological Society of America*, *90*, 1535-1542.

Tucker, B. E., King, J. L., Hatzfeld, D., & Nersesov, I. L. (1984). Observations of hard-rock site effects. *Bulletin of the Seismological Society of America*, *74*, 121-136.

Üçer S. B., Crampin, S., Evans R., Miller, A., & Kafadar, N. (1985). The MARNET radio linked seismometer network spanning the Marmara Sea and the seismicity of western Turkey. *Geophysical Journal International*, *83*, 17-30.

Wessel, P., & Smith, W. H. F. (1995). New version of the generic mapping tools released. *EOS Transactions of the American Geophysical Union*, *76*, 329.

Westaway, R., Pringle, M., Yurtmen, S., Demir, T., Bringland, D., Rowbotham, G., et al., (2004). Pliocene and Quaternary regional uplift in western Turkey: the

Gediz River terrace staircase and the volcanism at Kula. *Tectonophysics*, *391*, 121−169.

Yalçınkaya, E., Tekebaş, S., & Pınar, A. (2013). Analysis of ambient noise in Yalova, Turkey: Discrimination between artificial and natural excitations. *Journal of Seismology*, *17*, 1021-1039.

Yang, X., Lay, T., Xie, X. B., & Thorne, M. S. (2007). Geometric spreading of Pn and Sn in a spherical Earth model. *Bulletin of the Seismological Society of America*, *97*, 2053-2065.

Yılmaz, Y., Genç, S. C., Gürer, O. F., Bozcu, M., Yılmaz, K., Karacık, Z., et al. (2000). When did the western Anatolian grabens begin to develop?. In E. Bozkurt, J. A. Winchester, & J. D. A. Piper, (Eds.) *Tectonics and magmatism in Turkey and the surrounding area* (173) (353-384). London: Geological Society of London Special Publications.

Yılmaz, H. (2007). Stream sediment geochemical exploration for gold in the Kazdağ dome in the Biga peninsula, Western Turkey. *Turkish Journal of Earth Sciences*, *16*, 33-55.

Zhu, L., Akyol, N., Mitchell, B. J., & Sözbilir, H. (2006a). Seismotectonics of western Turkey from high resolution earthquake relocations and moment tensor determinations. *Geophysical Research Letters*, *33*, L07316.

Zhu, L., Mitchell, B. J., Akyol, N., Çemen, I., & Kekovalı, K. (2006b). Crustal thickness variation in the Aegean region and its implications for the extension of continental crust. *Journal of Geophysical Research*, *111*, B01301.

Zor, E., Sandvol, E., Gürbüz, C., Türkelli, N., Seber, D., & Barazangi, M. (2003). The crustal structure of the east Anatolian plateau from receiver functions. *Geophysical Research Letters*, *30*, 8044.

Zor, E., Sandvol, E., Xie, J. K., Türkelli, N., Mitchell, B. J., Gasanov, A. H., et al., (2007). Crustal attenuation within the Turkish plateau and surrounding regions. *Bulletin of the Seismological Society of America*, *97(1B)*, 151-161.